



HAL
open science

Strong anharmonicity in the phonon spectra of PbTe and SnTe evaluated via the stochastic self-consistent harmonic approximation.

Guilherme Almeida Silva Ribeiro

► **To cite this version:**

Guilherme Almeida Silva Ribeiro. Strong anharmonicity in the phonon spectra of PbTe and SnTe evaluated via the stochastic self-consistent harmonic approximation.. Condensed Matter [cond-mat]. Université Pierre et Marie Curie - Paris VI, 2017. English. NNT : 2017PA066737 . tel-02999127

HAL Id: tel-02999127

<https://theses.hal.science/tel-02999127>

Submitted on 10 Nov 2020

HAL is a multi-disciplinary open access archive for the deposit and dissemination of scientific research documents, whether they are published or not. The documents may come from teaching and research institutions in France or abroad, or from public or private research centers.

L'archive ouverte pluridisciplinaire **HAL**, est destinée au dépôt et à la diffusion de documents scientifiques de niveau recherche, publiés ou non, émanant des établissements d'enseignement et de recherche français ou étrangers, des laboratoires publics ou privés.

**THÈSE DE DOCTORAT
DE L'UNIVERSITÉ PIERRE ET MARIE CURIE**

Spécialité : Physique

École doctorale : Physique en Île-de-France

réalisée

à l'**Institut de Minéralogie, de Physique des Matériaux et de Cosmochimie
(IMPMC)**

présentée par

Guilherme ALMEIDA SILVA RIBEIRO

pour obtenir le grade de:

DOCTEUR DE L'UNIVERSITÉ PIERRE ET MARIE CURIE

Sujet de la thèse

**Strong anharmonicity in the phonon spectra of PbTe and SnTe
evaluated via the stochastic self-consistent harmonic approximation.**

Soutenue le 05/12/2017

devant le jury composé de:

Mme. Sylvie Hébert	Rapporteur
M. Natalio Mingo	Rapporteur
M. Matthieu Verstraete	Examineur
M. Massimiliano Marangolo	Examineur
M. Matteo Calandra	Directeur de thèse
M. Lorenzo Paulatto	Co-Directeur de thèse

Institut de minéralogie, de physique des
matériaux et cosmochimie
Université Pierre et Marie Curie
4, Place Jussieu
75252 Paris CEDEX 05

École doctorale: Physique en Île-de-
France

Contents

List of Figures	5
Acknowledgements	13
Introduction	15
1 Main experimental findings: structural, electronic, and vibrational properties of SnTe and PbTe.	19
1.1 Crystal structure	20
1.2 Electronic structure	21
1.2.1 Experimental findings	21
1.2.2 Comments on ab-initio simulations of the electronic structure	23
1.3 Vibrational properties	25
1.4 Summary	28
2 Dynamical properties of solids	31
2.1 Lattice dynamics	31
2.1.1 The general picture	31
2.1.2 The ionic Hamiltonian	33
2.2 Density functional perturbation theory (DFPT)	35
2.2.1 Dynamical matrix from the density response function	35
2.2.2 Density functional perturbation theory (DFPT)	37
2.2.3 Born effective charges	39
3 Anharmonicity	41
3.1 Anharmonic effects	41
3.2 Thermal expansion and the Quasi-Harmonic Approximation	43
3.3 Perturbation theory and anharmonic effects	45
3.3.1 Phonon self-energies, linewidth, and lineshifts	45
3.3.2 Perturbation theory validity	47

3.4	Stochastic self-consistent harmonic approximation	48
3.4.1	Self-consistent harmonic approximation	48
3.4.2	Structural second order phase transition, and the free energy curvature	50
3.4.3	Phonon quasiparticles	52
3.4.4	SSCHA self-energies	53
3.5	Summary	54
4	Magnitude of the anharmonic contribution	57
4.1	Calculation details	58
4.2	Harmonic phonon dispersion	59
4.2.1	Dependence on the volume	59
4.2.2	k-points sampling in SnTe	61
4.2.3	Born effective charges and doping	61
4.3	Anharmonic contribution to the phonon dispersion: static limit ($z = 0$)	63
4.3.1	Magnitude of $\langle D3V \rangle$ and $\langle D4V \rangle$ terms	63
4.3.2	Evaluation of PbTe thermal expansion at 600K	66
4.3.3	Empirical potential calculations	67
4.4	Anharmonic contribution to the phonon dispersion: Dynamical self-energy calculations, ($z = \omega = \omega_{\mathbf{q}\mu}^{sscha}$)	73
4.4.1	Diagonal vs off-diagonal self-energies	73
4.4.2	Third order force constants	75
4.5	Summary	78
5	Lattice-dynamics of PbTe and SnTe	85
5.1	Lead telluride (PbTe)	85
5.1.1	Anharmonic phonon dispersion	85
5.1.2	Satellite peak due to phonon-phonon scattering.	88
5.2	Tin telluride (SnTe)	90
5.2.1	Structural phase transition in SnTe	93
5.3	Summary	94
6	Conclusion and Perspectives	95
A	Density functional theory overview	99
A.1	Hohenberg-Kohn theorems	99
A.2	The Kohn-Sham equations	100
A.3	Local density approximation (LDA)	101
A.4	Generalized gradient approximation (GGA)	102

Résumé en français 103

Bibliography 117

List of Figures

1	p- and n-type thermoelectric materials	17
1.1	A section of the rock salt structure. The primitive unit cell is given in green.	20
1.2	SnTe structural transition from a rock-salt to a rhombohedral structure.	21
1.3	Model for the valence and conduction bands at low temperature for PbTe, for the composition in which the energy gap is zero, and for SnTe.	22
1.4	Comparison between PbTe and SnTe surface band structure. In (a) the near Fermi energy, E_f , electronic states around the $\bar{\Lambda}$ point of the BZ is shown. (b) shows the ARPES intensity plots showing the broader feature coming from the top of the valence band of PbTe and the presence of the metallic Dirac-like band in SnTe. (c) illustrates the band inversion model with the addition of the surface states. Here SS, CB, VB denote the surface state, the bulk conduction band, and the bulk valence band, respectively.	24
1.5	Electronic band structure of SnTe (a) and PbTe (b). The red dots represent the fraction of electronic charge residing on the Te atoms. The grey highlights the intrinsic band of SnTe.	25
1.6	Band dispersion of SnTe. The (001) surface states are denoted by the red lines. As found in experiment, the Dirac point is slightly away from the \bar{X} point of the surface BZ.	26
1.7	Phonon dispersion curves of PbTe at 296 K for different directions along the BZ. The dots denote the INS measurements as the solid lines represent a theoretical model for PbTe developed by the authors [15].	27

1.8	PbTe $S(\mathbf{q}, E)$ data for dispersion along $[0,0,L]$ in (113) BZ at (a) 300 K and (b) 600 K. The white lines denote harmonic calculations performed by the authors, and pink diamonds indicates the peak for the TO scans at Γ . The red arrows indicate where the avoid crossing between LA and TO modes occurs. From ref.[19]	28
1.9	INS measurements of $S(\mathbf{q}, E)$ of SnTe. (a,b) $S(\mathbf{q}, E)$ measured at $T = 50$ and 300 K, respectively, along the $[H,H,3]$ direction. White lines are renormalized phonon dispersion calculated at $T = 300$ K. Taken from [20]	29
1.10	Resistivity measurements vs temperature of SnTe for various carrier concentrations from ref.[28]. The position of the kink in the curve indicates where the structural transition occurs.	30
1.11	The transition temperature T , versus carrier concentration. resistivity (open dots);neutron Bragg reflection result (dot in circle); INS result (solid circle), x-ray results (crosses); Raman scattering results (r); anomaly position of Hall mobility at 77 K (triangle), theoretical curve obtained by a fit (solid lines). Taken from ref.[28]	30
3.1	Slice of the spectral function of PdH at 80 K. Linewidth example	42
3.2	Processes produced in lowest-order perturbation theory by cubic and quartic anharmonic terms	42
3.3	Energy of the transverse optical (TO) mode at zone center of PbTe at different temperatures.	44
3.4	Comparison between QHA, TDEP, and experimental cross sections for PbTe.	44
3.5	The self-energy Feynman diagrams which contribute to the total self energy $\Pi_{\mu}(\mathbf{q}, \omega)$ at the perturbative level.	45

3.6	The shape (a) illustrates the vibrational problem of a molecule. When vibrations are small only the bottom of the well comes in, so in this case the harmonic approximation (dotted curve) is reasonable. If the well has a different shape, shape (b) for example, the harmonic approximation breaks down (dotted curve). However, a pseudo-harmonic approximation is still possible with a harmonic oscillator wave-function and the frequency parameter fitted by a variational principle equivalent to the fixing of average position and mean-square deviation (dashed curve). Taken from [78]	48
3.7	Second-order phase transition, as described by Landau's theory.	51
4.1	Harmonic phonons dispersion of PbTe and SnTe for different lattice constants.	60
4.2	Low-temperature rhombohedral structure of SnTe can be obtained as a small distortion of the rock-salt structure	61
4.3	Double-well anharmonic phonon potential. Frozen phonon potentials of Γ -point TO phonon mode of SnTe and PbTe. Red solid boxes and lines correspond to relaxed lattice parameters at 0 K. The depth of the well in this case is close to 1 meV. Taken from the supplemental material of ref.[20]	62
4.4	Frozen phonon potential for SnTe in function of the k-point grid.	63
4.5	SnTe harmonic phonon dispersion using a $4 \times 4 \times 4$ supercell: undoped (red) and doped (blue) case. Besides points very close to the zone center, doping does not change considerably the dispersion curves.	64
4.6	Anharmonic phonon dispersion curves for PbTe at 300 K and 600 K.	65
4.7	SSCHA runs for SnTe at 50 K and 100 K.	66
4.8	vibrational free energy plus the BO total energy vs lattice parameter.	67
4.9	Anharmonic phonon spectra for the PBE at 600 K lattice parameter versus the PBE at 0 K case.	68
4.10	Anharmonic PbTe phonon dispersion at 300 K on a $4 \times 4 \times 4$ supercell: Ab-initio vs (blue lines) empirical potential (red lines).	70

4.11	Anharmonic SnTe phonon dispersion at 100 K on a $4 \times 4 \times 4$ supercell: Ab-initio vs (blue lines) empirical potential (red lines). The phonon frequencies ($\Omega_{\mu\mathbf{q}}$) are obtained using Eq.(3.31) in the static limit, namely by using $\Pi_{\mu}(\mathbf{q}, 0)$	70
4.12	Comparison between PbTe anharmonic phonon spectra using a $2 \times 2 \times 2$ (blue) and $4 \times 4 \times 4$ (red) supercell.	71
4.13	Comparison between SnTe anharmonic phonon spectra using a $4 \times 4 \times 4$ (red) and $5 \times 5 \times 5$ (purple) supercell.	71
4.14	On the TO modes in function of T for PbTe (top) and SnTe (bottom) for different supercell sizes.	72
4.15	Anharmonic phonon spectra of PbTe at 300 K (left) and 600 K (right) calculated via perturbation theory, diagonal case (solid lines), on top of the spectral function calculated considering off-diagonal self-energies (heat map).	75
4.16	Anharmonic phonon spectra of SnTe at 50 K (top) and 100 K (bottom) calculated via perturbation theory, diagonal case (solid lines) on top of the spectral function (heat map) calculated considering off-diagonal self-energies.	76
4.17	Spectral weight of PbTe at 300K (right) and 600 K (left), for $\mathbf{q} = \Gamma$	77
4.18	Spectral weight of SnTe at 50K (right) and 100 K (left), for $\mathbf{q} = \Gamma$	78
4.19	Spectral function of PbTe at 300K. The third-order forces constants were calculated via the SSCHA (left) and by the finite difference method (right).	79
4.20	Spectral weight of PbTe at 300K (right) and 600 K (left), for $\mathbf{q} = \Gamma$. The position of the peaks is very similar, the different	80
4.21	Spectral function of PbTe at 600K. The third-order forces constants were calculated via the SSCHA (left) and by the finite difference method (right).	80
4.22	Spectral function of PbTe at 600K for $\mathbf{q} = \Gamma$. The third-order forces constants were calculated via the SSCHA (left) and by the finite difference method (right).	81
4.23	Spectral function of SnTe at 50K. The third-order forces constants were calculated via the SSCHA (top) and by the finite difference method (bottom).	81
4.24	Slice of the spectral function of SnTe at 50 K, $\mathbf{q} = \Gamma$. the third-order force constants were calculated via the SSCHA and by the finite difference method.	82

4.25	Spectral function of SnTe at 100 K along special point on the BZ. The third-order forces constants were calculated via the SSCHA (top) and by the finite difference method (bottom).	82
4.26	Slice of the spectral function of SnTe at 100 K, $\mathbf{q}=\Gamma$. the third-order force constants were calculated via the SSCHA and by the finite difference method.	83
5.1	Schematic of nesting between acoustic and optical branches in phonon dispersions of PbTe from ref.[20].	86
5.2	Joint density of states of PbTe and SnTe calculated by Li et al [20].	87
5.3	PbTe harmonic (dashed lines) and anharmonic (solid lines) phonon dispersion curves at 300 K compared with INS experiments at 300 K (black dots).	88
5.4	PbTe harmonic (dashed lines) and anharmonic (solid lines) phonon dispersion curves at 300 K compared with INS experiments at 300 K (black dots).	89
5.5	PbTe Spectral function at 300 K calculated along the X- Γ -X path (color map). Solid lines denote the anharmonic phonon dispersion curves, black dots denote INS experimental data, and pink squares denote the experimental values for the peaks at the zone center.	89
5.6	PbTe Spectral function at 600 K calculated along the X- Γ -X path (color map). Solid lines denote the anharmonic phonon dispersion curves. The intensity of the satellite peak decreases with increasing temperature, and the TO modes shift towards higher energies.	90
5.7	Comparison between the harmonic (black lines) and anharmonic phonon dispersion curves of SnTe at 50 K (red lines) and 100 K along special points in the BZ.	91
5.8	Harmonic (dashed lines) and anharmonic (solid lines) phonon dispersion relations of SnTe at 100 K (red lines) compared with IXS experiments at 75 K (black dots).	91
5.9	SnTe Spectral function at 100 K calculated along the X- Γ -X path (color map). Solid lines denote the anharmonic phonon dispersion curves.	92
5.10	Energy square of the TO phonons on the zone-center plotted against temperature.	93

-
- 6.1 Preliminary results on the NiTi system. The plot compares experimental data at 400 K (points) with the harmonic phonon dispersion using the $2 \times 2 \times 2$ (black) and $3 \times 3 \times 3$ (black) supercells, and unconverged SSCHA calculations; $2 \times 2 \times 2$ (blue) and $3 \times 3 \times 3$ (red) supercells. 97
- A.1 Courbe de dispersion des phonons harmoniques pour PbTe et SnTe pour différents paramètres de mailles. Pour les paramètres de mailles expérimentaux (lignes rouges) chaque système ne présente aucune fréquence négative. Pour les paramètres de mailles optimisés par la méthode PBE (lignes bleues), le spectre phononique du SnTe montre des fréquences négatives au point Γ , indiquant ainsi une instabilité structurelle. Les modes TO au point gamma a une forte dépendance sur le volume.. . . . 109
- A.2 Courbes de dispersion des phonons harmoniques (lignes pointillées) et anharmoniques (lignes pleines) pour PbTe à 300 K, comparées avec les expériences INS [42] à 300K. La courbe de dispersion des phonons anharmoniques ($\Omega_{\mathbf{q}\mu}$) est obtenue d'après l'équation (A.20) et comprend la contribution de l'énergie propre sous la forme *bulle*. 112
- A.3 Fonction spectrale de PbTe à 300K calculée le long de la trajectoire X- Γ -X (carte en couleur). Les lignes pleines représentent les courbes de dispersions des phonons anharmoniques, les points noirs les données expérimentales de réf.[42] et les carrés roses les valeurs expérimentales du pics pour le centre de zone d'après les expériences plus récentes de la réf.[19]. Le code de couleur est déterminé par la valeur de $\sigma(\mathbf{q}, \omega)$, équation (A.21). 113
- A.4 Courbes de dispersion des phonons harmoniques (lignes pointillées) et anharmoniques (lignes pleines) pour SnTe à 100 K (lignes rouges), comparées avec les expériences IXS [84] à 75K (points noirs). La courbe de dispersion anharmonique ($\Omega_{\mathbf{q}\mu}$) est obtenue d'après l'équation (A.20) et comprend la contribution de l'énergie propre sous la forme *bulle*. 114

A.5	Énergie au carré pour les phonons TO au centre de la zone en fonction de la température. Les carrés rouges présentent les résultats obtenus à l'aide de l'équation (A.20), et les carrés noirs présentent les résultats d'ONeil et al.[84]. L'extrapolation linéaire montrent que les modes s'annulent à une énergie nulle aux alentours de la $T_c \approx 23 K$ d'après nos calculs.	115
-----	--	-----

Acknowledgements

It is always hard to look back and see how fast things change. I arrived in France as a young dreamer from South America. Now, I see myself as a way more complex, realistic (unfortunately), and mature human being. The adventure of making a Ph.D far away from home, from family, from friends, molded me into who I am now. It was not easy, it was not perfect, but even with all the difficulties, and all the sorrow, I can say without any doubt that it was worth it. I can look to these past years and smile, and be grateful for this opportunity. In the lines to follow I would like to acknowledge some persons that played some role in my journey.

I would like to start by acknowledging my supervisors. First, Francesco for giving me the opportunity to do my Ph.D here at the IMPMC, and for his advice during the time we worked together. I have a big gratitude towards you, and I wish you all the best. Lorenzo, thank you for being such a nice person, for your patience, and for your support when things seemed not to work properly. Definitely, I've learned a lot from you. Finally, thank you Matteo for always being kind to me. You believed in me when I was completely lost and with my spirit broken. I'll never forget your advice and knowledge you shared with me. It was a great pleasure to work under your supervision.

Second, I would like to acknowledge the CAPES foundation for the opportunity and for the scholarship that allowed me to carry my studies here in France.

A huge thanks to my brothers and sisters: David, Abdel, Mario, Nico, Andreax, Tuzin, Susu, Marie, Gaby, Mio, Yo, Camille, Jatin, Mat, Henrique, Edo, Eric, Peppe, Chicca, Alisha, Guillaume, Alexandre, Carlos, Thomaso, Raffaello, Betül, Sam, Fred, Irina, Laporta, Andrea Gauzzi, Lili, Fernanda, Andreíta. You are really family for me. Thank you for all the good moments we shared together. I truly love you all with all my heart (and you know that normally I do not speak about my feelings).

Another huge thanks to my officemates: Clémence, Mathilde, Félix,

Fra, Abdel(again), Giulia. I'll always remember the times we laughed (and cried) together. You have a special place in my hearth.

To all of my friends from the IMPMC, from Brazil (-Emilson), and from all over the world; thank you very much.

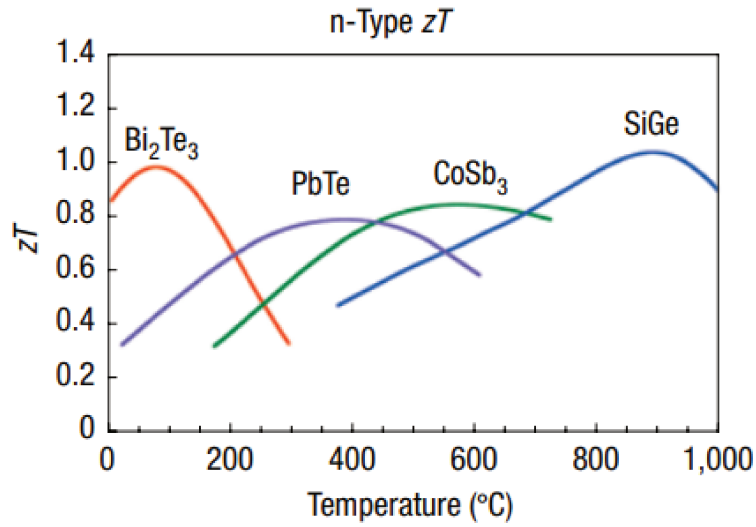
Thank you, Sabrina, for being this amazing partner, and for making me try to be the best that I can. I am very lucky to be part of your life. Last, a special acknowledgement to my parents, Rogério and Graça. Thank you for being always there for me, and sorry for not saying often how much I love and admire you two.

Introduction

The increase of energy consumption and global issues, such as global warming and climate change, have increased the interest for alternative ways to generate energy [1]. These issues are usually linked to the use of fossil fuels for transport, industrial processes, and for energy generation in thermal power stations. According to some predictions, the global oil reserves will last approximately for fifty years more. Due to this fact and environmental concerns, the international community have been tried over the past few year to create agreements and initiatives in order to reduce the primary energy consumption, which is approximately 30% oil based [2]. Recently, during the 2015 United Nations Climate Change Conference (COP21), through a series of resolutions, some countries agreed to search for strategies to increase the efficiency in energy generation, limit carbon dioxide emissions, and boost the utilization of renewable energy sources. The private sector, conscientious of these matters, is also promoting this way of thinking, and is investing in new technologies. For example, the success of companies such as Tesla motors, indicates that clean energy powered vehicles tend to become a new trend; environmental friendly and profitable [3, 4].

Among other solutions, the use of thermoelectric technology is considered a very promising alternative and clean technology for energy harvesting and recovery. By using thermoelectric devices one can convert the wasted heat from different sources, like solar radiation, and automotive exhausts, into electric power via thermoelectric generators, or Seebeck generators. In addition, thermoelectric materials are also capable of operate on the other way around, converting an electric voltage into temperature differences. This effect is known as thermoelectric cooling, or Peltier cooling, with applications varying from refrigerators, temperature controllers, or other cooling devices.[5, 6, 7]

The critical aspect concerning thermoelectrics is to develop efficient devices. The thermoelectric efficiency is related to an dimensionless quantity



n-type thermoelectric materials.

called thermoelectric figure of merit, ZT , given by :

$$ZT = \frac{S^2 \sigma T}{k_e + k_l}, \quad (1)$$

S is the Seebeck coefficient, T the temperature, σ is the electronic conductivity, k_e and k_l are the electronic and lattice contributions to the thermal conductivity, respectively. The higher is the figure of merit, higher is the efficiency of a thermoelectric device. Hence, in order to achieve a high ZT one can search for compounds with high σ , and low thermal conductivity.

The challenge here is to find materials which are appropriate, affordable, and efficient in order to develop power generation applications. Nowadays, the most popular thermoelectric materials are alloys of bismuth telluride and antimony telluride; Bi_2Te_3 and Sb_2Te_3 [9, 10]. These compounds exhibit a large figure of merit for near room-temperatures, and are appropriate for refrigeration and wasted heat recovery applications up to 200°C . Bi_2Te_3 alloyed with other materials such as Bi_2Se_3 and Sb_2Te_3 was studied as a promising thermoelectric material since the fifties. This alloying process allows a fine tuning of the carrier concentration in conjunction with a reduction in lattice thermal conductive, then enhancing ZT . The highest values of ZT for these materials range from 0.8 to 1.1 as it is illustrated in Fig.(1). However, by adjusting the carrier concentration the value of ZT as well the temperature at which occurs change, enabling applications in different ranges [11].

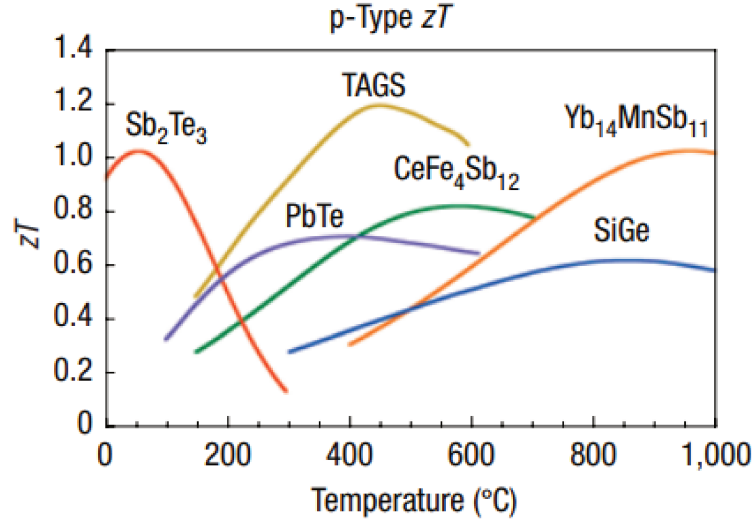


Figure 1: p-type thermoelectric materials. Most of these materials are complex alloys with dopants; approximate compositions are shown. By changing the dopant concentration the peak of ZT and the temperature where it occurs are modified. Figure taken from [8].

For power generation in the range between 200°C and 600°C, materials based on IV-VI salts are typically used, such as PbTe, GeTe, or SnTe [10, 12]. Also, for those materials, ZT can be modified via a tuning of the carrier concentrations. The highest values for the figure of merit have been achieved by alloying with AgSbTe₂. However, for real long term applications only the alloy (GeTe)_{0.85}(AgSbTe₂)_{0.15} (TAGS), with a maximum ZT greater than 1.2, have been applied extensively [8].

In addition to its thermoelectric properties, the presence of strong anharmonic effects in the family of IV-VI compounds gives rise to interesting properties, such as the presence of soft phonon modes heavily affected by temperature, phonon satellites, and ferroelectric instabilities. Indeed, materials such GeTe, PbS, and SnTe undergo second order structural phase transitions from the rock-salt structure to a distorted ferroelectric phase. On the other hand, PbTe remains cubic, being considered a incipient ferroelectric [13, 14, 15].

To have a full theoretical understanding of the mechanisms behind the ferroelectric transition and also to study the anharmonic contributions to the lattice dynamical properties of these solids, one must chose wisely the methodology. Since they are conceptually simple, having few atoms in their unit cells and, by consequence, few phonon modes, they are a class of

materials perfectly suitable to be used as playground for various theoretical developments. On the past, many approaches based on the harmonic theory, and on perturbation theory failed to obtain reliable results. Hence, showing the need of methodologies beyond the perturbative limit. One of the most promising methods is the so called stochastic self-consistent harmonic approximation [16, 17, 18]. This methods aims to minimize the free energy of a given system via a stochastic procedure. Then, it allows the evaluation of anharmonic phonon spectra, self-energies, and lattice instabilities, as needed for the IV-VI salts.

This thesis devoted to the study the anharmonic contribution to the lattice dynamical properties of the thermoelectric compounds PbTe and SnTe using some new developments of the stochastic self-consistent harmonic approximation . First, on chapter 1 we discuss some relevant findings and the phenomenology of IV-VI chalcogenides. Chapters 2 and 3 we present the theoretical framework used in this thesis, starting from the harmonic theory and the density-functional perturbation theory to the inclusion of anharmonicity via different approaches. In the latter, we discuss the limits of perturbative methods, and we give a brief, although deep, introduction to the method used in this work. Chapter 4 aims to test and validate the methodology by applying it to our systems of interest for a variety of different cases. The comparison between experimental findings and our calculations for PbTe and SnTe are presented on chapter 5. Finally, the main conclusions drawn will be acquainted in chapter 6.

Chapter 1

Main experimental findings: structural, electronic, and vibrational properties of SnTe and PbTe.

The family of IV-VI compounds have been extensively studied experimentally since the fifties. In particular, PbTe, GeTe, and SnTe gained attention due to their thermoelectric properties [10, 12], the relevance of the anharmonic effects in their phonon spectra [19, 20], the occurrence of ferroelectric phase transitions in SnTe and GeTe [13, 21, 22, 23], and more recently, the presence of surface states on SnTe. Hence, including the latter on the hot field of topological insulators [24, 25].

In this chapter we give a brief overview on some experimental findings focusing on PbTe and SnTe. We start our discussion with their crystal structure and its dependence on temperature and pressure. Then, we discuss about their electronic properties. We focus this discussion on features such as the presence of a small-gap, a band inversion mechanism present on the $\text{Pb}_{1-x}\text{Sn}_x\text{Te}$ alloy dependent on Sn concentration, and the existence of surface states on SnTe. In addition, we discuss some theoretical results present in literature. Then, we highlight some experimental studies aiming to describe the lattice dynamical properties and the role of anharmonicity in both compounds. First we discuss some inelastic ion scattering measurements for PbTe. Then, we compare the latter with findings for SnTe. Finally, the study of the ferroelectric transition in SnTe is addressed.

1.1 Crystal structure

One of the main reasons why some materials of the IV-VI family are interesting is due to their, in principle, simple structure. At room temperature and ambient pressure, PbTe and SnTe have a rock-salt structure as illustrated in Fig.(1.1). Where PbTe has a lattice parameter of $a = 6.462 \text{ \AA}$ at 300 K whereas SnTe lattice constant is $a = 6.387 \text{ \AA}$ for the same temperature [26, 27].

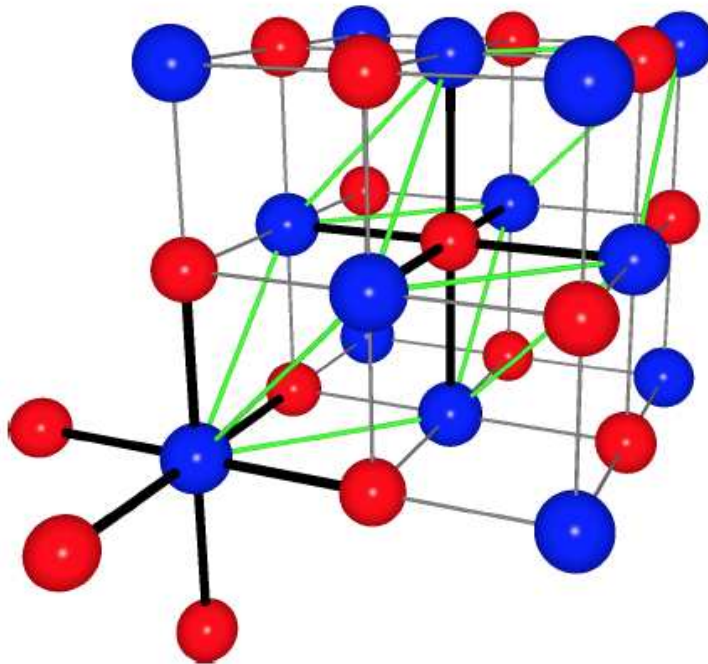


Figure 1.1: A section of the rock salt structure of PbTe and SnTe. The primitive unit cell is given in green.

For temperatures in the range between 0 K to 120 K, SnTe undergoes a structural transition towards a rhomboedral structure, becoming then a ferroelectric material. In this phase, due to a small dimerization along the (111) direction, the lattice parameter assumes the values of $a = 6.325 \text{ \AA}$ and the rhombohedral angle is $\alpha = 89.895^\circ$ [28]. The structural transition is illustrated in Fig.(1.2) depends strongly on the sample doping, being absent if the carrier concentrations (due to off-stoichiometry) is smaller than $n_p = 1.5 \times 10^{20} \text{ cm}^{-3}$. We will talk more about this transition when discussing the measurements of optical properties of SnTe, since it can be studied using different techniques.

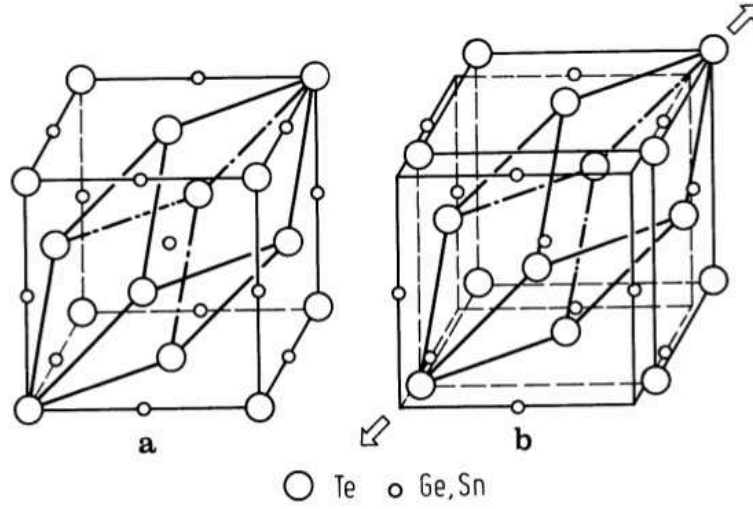


Figure 1.2: SnTe structural transition from a rock-salt to a rhombohedral structure. From ref [29]

Finally, according to X-ray experiments, an orthorhombic phase can be induced as pressure is applied. The critical pressure is 20 kbar and 42 kbar, for SnTe and PbTe, respectively [30].

1.2 Electronic structure

1.2.1 Experimental findings

PbTe and SnTe are narrow direct-gap semiconductors. The optical gap is of the order of 0.31 eV and 0.18 at the L point on the BZ, for PbTe and SnTe at 300 K, respectively. In addition, the band edges are nonparabolic, and the ordering of the levels at L is composition sensitive and determines the temperature and pressure coefficients of the band gap [31]. In order to calculate transport properties the mechanism behind the levels ordering at L must be well understood and determined [31]. Hence, this fact motivated both experimental and theoretical studies using a large range of techniques [32].

On the experimental side, Dimmock et al.[33] carried out photoluminescence experiments in order to evaluate the evolution of the electronic properties of the $\text{Pb}_x\text{Sn}_{1-x}\text{Te}$ alloy in function of temperature and Sn concentration. For PbTe, via luminescence data, the values for the band gap

at the L point in the Brillouin zone (BZ) varies from 0.186 eV to around 0.31 eV at 12 K and 300 K respectively. Hence, the authors concluded that the band gap increases with temperature. On the other hand, SnTe band gap dependence was found, via tunneling experiments [34], to have the opposite behavior, ranging from 0.18 eV at 300 K and 0.3 eV at ≈ 4.2 K. In addition, by varying the mole fraction of SnTe, $1 - x$, in the $\text{Pb}_x\text{Sn}_{1-x}\text{Te}$ alloy, it was found that the band gap reduces as the alloy becomes Sn rich, being zero for $1 - x = 0.35$ at low temperature, and $1 - x = 0.62$ at 300 K. For this reason, they proposed a model, illustrated in Fig.(1.3), in which the valence and conduction bands of SnTe are inverted in relation from these of PbTe.

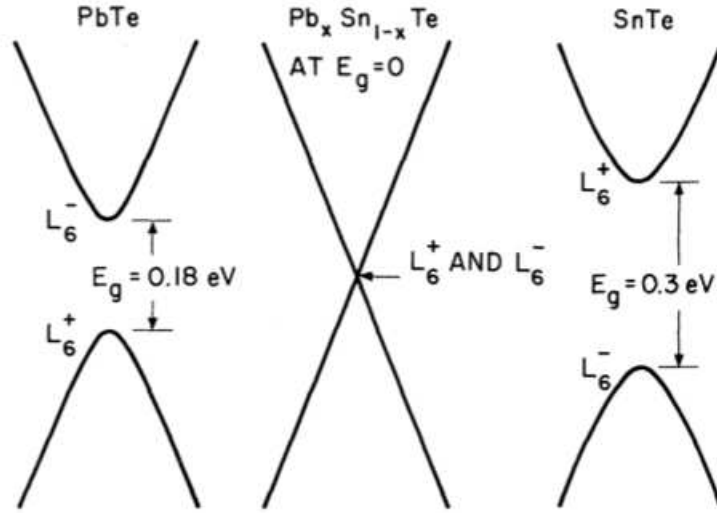


Figure 1.3: Model for the valence and conduction bands at low temperature for PbTe, for the composition in which the energy gap E_g is zero, and for SnTe. By increasing the concentration of Sn the gap energy becomes zero at a certain point, after a band inversion occurs. Taken from ref.[33]

It is believed that the conduction band and the valence band edges are a L_6^- and a L_6^+ states, respectively. On the Pb rich system, the L_6^- and L_6^+ are associated with p-orbital of Pb, and Te, respectively. By increasing Sn concentration the energy gap E_g decreases as these states approach each other, it becomes zero for a intermediate stage in which the states are degenerate, and then increases with now the L_6^- and L_6^+ states representing the valence and conduction band edges, respectively.

More recent experiments using the angle-resolved photoemission spectroscopy technique (ARPES) investigated this band inversion in detail [35],

supporting the model of Dimmock. In addition, other ARPES measurements [24] verified the existence of a topological crystalline insulator (TCI) phase of SnTe.

The work of Tanaka et al.[24] shows that SnTe is a TCI with metallic Dirac-cone surface band. In addition, they performed similar measurements showing that PbTe is a trivial insulator, which is in agreement with theoretical predictions. The ARPES measurements shown in Fig.(1.4a) displays the electronic states close to E_f and around the $\bar{\Lambda}$ point of the BZ. This point is the one in which the top of the Dirac-like band is found, and it is located slightly away from the \bar{X} point of the surface BZ corresponding to a projection of the L point of the bulk BZ. It found that PbTe does not exhibit evidence of a metallic Dirac-like band, and shows only a broad feature coming from the top of the valence band, as shown in Fig.(1.4b). Hence, one can conclude that a topological phase transition from the trivial insulator, PbTe, to a TCI phase takes place in the $\text{Pb}_{1-x}\text{Sn}_x\text{Te}$ alloy. The model proposed by Dimmock et al.[33] is recovered, as can be illustrated in Fig.(1.4c).

1.2.2 Comments on ab-initio simulations of the electronic structure

The electronic and structural properties of PbTe have been largely investigated via ab-initio methods since the interest on these materials grew during the sixties. However, their description can be quite tricky due to some of their particular features. Since PbTe and SnTe are small-gap semiconductors, the evaluation of their band structure via ab-initio calculations, specially within the density functional theory (DFT)[36, 37] is a delicate matter. The use of standard approximations, such as local density approximations (LDA) and generalized gradient approximation (GGA) [38], normally underestimates the direct gap at the L point in the Brillouin-zone (BZ), specially for PbTe. This property depends on the lattice parameter chosen in the simulations. Furthermore, it influences directly the calculations of optical properties, so a consistent approach is desirable.

The first measure taken in order to correct the band gaps, is to include the spin-orbit coupling. Using LDA, Wei et al.[39] were able to reduce the error in the band gaps. Their calculations were partially empirical, making use of constant potential applied to the conduction-band states aiming to match the calculated gaps with the experimental data.

Within a fully DFT framework, the effects of the spin-orbit coupling

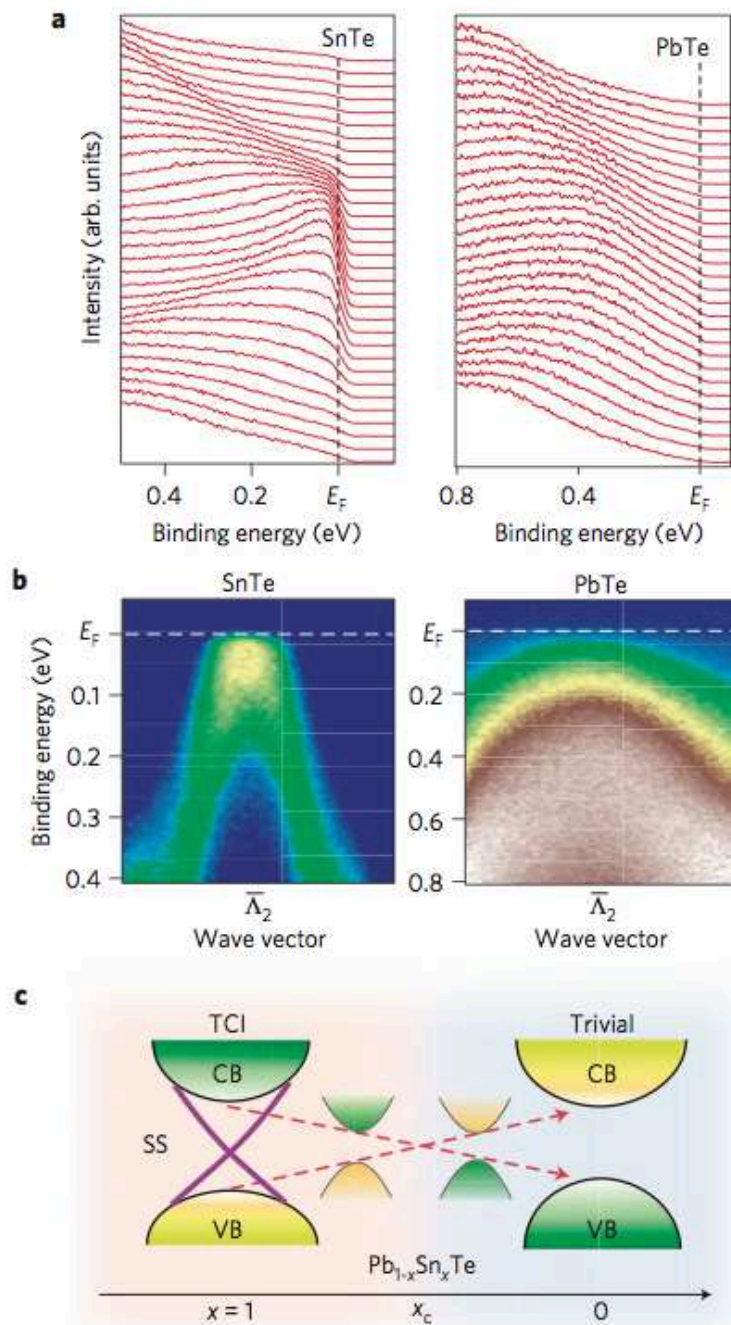


Figure 1.4: Comparison between PbTe and SnTe band structure [24]. In (a) the electronic states close to E_F and around the $\bar{\Lambda}$ point of the BZ are shown. (b) shows the ARPES intensity plots showing the broader feature coming from the top of the valence band of PbTe and the presence of the metallic Dirac-like band in SnTe. (c) illustrates the band inversion model with the addition of the surface states. Here SS, CB, VB denote the surface state, the bulk conduction band, and the bulk valence band, respectively.

were investigated deeply by Hummer et al.[40] It has been shown that the inclusion of the spin-orbit coupling by using GGA functionals leads to negative gap on the L point. The authors believe that the use of hybrid exchange-correlation functionals, such as the HSE06 [41], are particularly adequate since the increase the precision of the calculations. On the other hand, they also state that calculations using GGA functionals neglecting spin-orbit coupling are an suitable and less costly option [40].

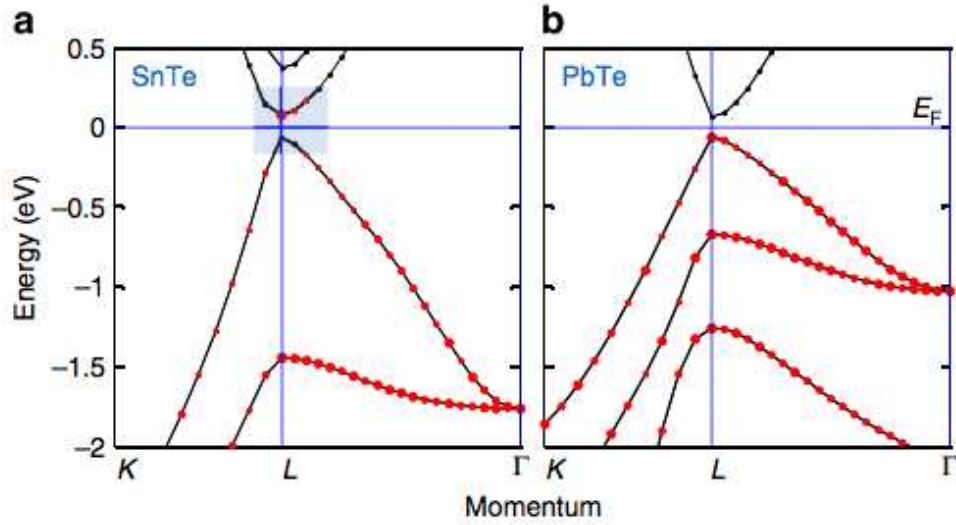


Figure 1.5: Electronic band structure of SnTe (a) and PbTe (b) from ref.[42]. The red dots represents the fraction of electronic charge residing on the Te atoms. The grey are highlights the intrinsic band of SnTe.

Using the GGA several studies manage to describe the inversion of the valence band character between PbTe and SnTe verified experimentally. Fig.(1.6) show the calculations performed by Hsieh et al.[42]. This study successfully calculated the surface states of SnTe close to \bar{X} as reported by Tanaka et al.[24]. In addition, they've also shown the inversion of the band character between PbTe and SnTe, Fig.(1.5).

1.3 Vibrational properties

The understanding of the vibrational properties of thermoelectric materials is crucial for both fundamentals reasons as for the development of efficient thermoelectric devices. PbTe and SnTe are among the most efficient thermoelectric materials, due to the their very low phonon thermal conductivity, k_{lat} . [39, 42, 43, 44, 45] For some time it was believed that this

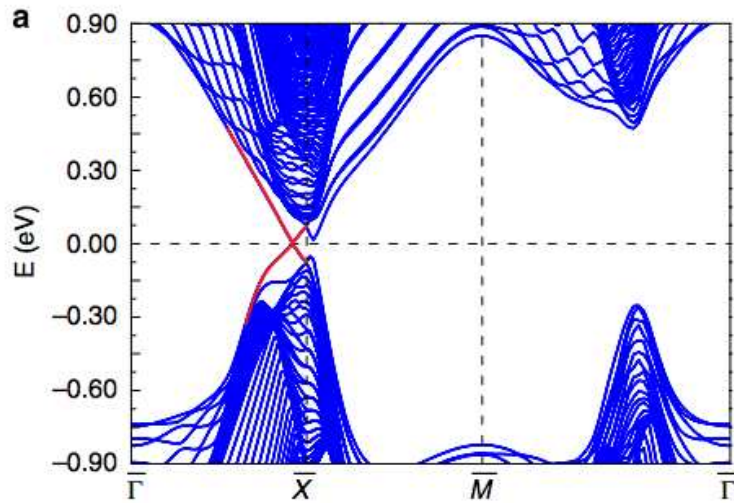


Figure 1.6: Band dispersion of SnTe. The (001) surface states are denoted by the red lines. As found in experiment, the Dirac point is slightly away from the \bar{X} point of the surface BZ. Taken from [42]

low thermal conductivity was due to the heavy masses, as well the proximity to a ferroelectric lattice instability which causes strong anharmonicity in these compounds. This strong anharmonicity causes the frequency of the low energy transverse optic modes (TO) at zone center to increase with increasing temperature [19, 46, 47].

We will start our discussion with PbTe because in principle it is simpler than SnTe due to the absence of a ferroelectric transition. For this reason it is called an incipient ferroelectric material. The work of Cochran et al [15], investigated the phonon dispersion curves of PbTe via INS experiments and, in addition, proposed some theoretical models to interpret their findings. Fig.(1.7) shows the phonon dispersion curves obtained at $T = 300$ K.

Their work reported that the TO modes at zone center have a value around 4.1 meV for $T = 300$ K. This work, in conjunction with the analysis of other IV-VI rock-salt chalcogenides, stated the first steps on the comprehension of lattice anharmonicity in this class of materials. However, due to new developments on the instrumentation, more recent INS experiments[19, 20] showed that PbTe is more complex and exhibits larger anharmonicity than SnTe. It presents a satellite peak on the neutron structure factor around the Γ point at 300 K, stating that in reality the peak obtained on the previous measurements are related to this additional peak whereas the high energy peak is close to 7.0 meV. Fig.(1.8) displays the neutron structure factor $S(\mathbf{q}, E)$ data for dispersion along $[0,0,L]$ in (113)

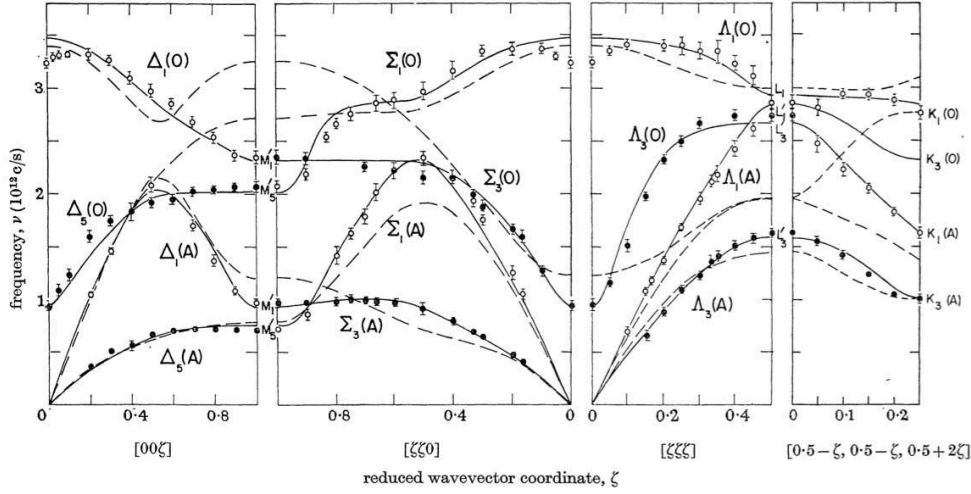


Figure 1.7: Phonon dispersion curves of PbTe at 296 K for different directions along the BZ. The dots denote the INS measurements as the solid lines represent a theoretical model for PbTe developed by the authors [15].

BZ, where pink diamonds represent the peak in the TO scans at Γ . Furthermore, they report another intriguing feature, an avoided crossing between longitudinal acoustic (LA) and TO phonon branches. The measured modes repel each other strongly for $\mathbf{q} = (0, 0, 1/3)$ as illustrated by the red arrows in Fig.(1.8) causing the avoided crossing. This feature is more evident at temperatures higher than 300 K.

Hence, due to its strong anharmonicity, the theoretical description of PbTe phonon spectra and the features reported is quite tricky. Methods based on the quasi-harmonic approximation and perturbation theory failed to describe the phonon spectra in function of temperature as well the presence of satellite peaks. [48, 49]. The use of more complex methodologies is then required in order to obtain reliable results.

Differently from PbTe, SnTe does not exhibit complex features in its INS spectra as obtained by Li et al.[20] Fig.(1.9) compares the features of the INS spectra of PbTe and SnTe. For low temperatures the spectra of SnTe show that it is close to an instability as the TO modes are low in energy. In particular, in this work they found that the ferroelectric transition occurs at $T_c \approx 42$ K.

The critical temperature for the ferroelectric transition is a debate which dates from the first works on SnTe vibrational properties. Some of the works stated that it might occur for temperatures close to 0 K, in others that its range is somehow large, varying from 0 K to 120 K.[13, 21, 22, 23] In

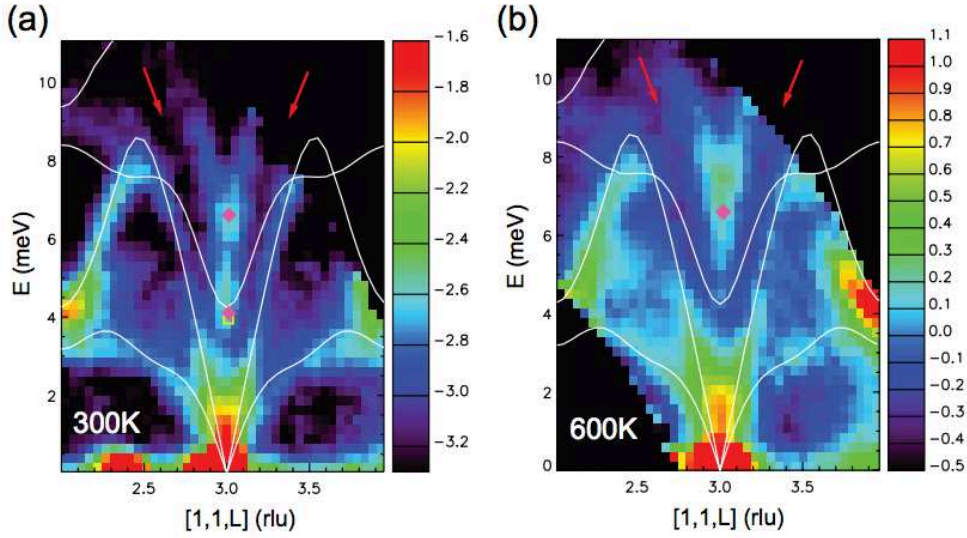


Figure 1.8: PbTe $S(\mathbf{q}, E)$ data for dispersion along $[0,0,L]$ in (113) BZ at (a) 300 K and (b) 600 K. The white lines denote harmonic calculations performed by the authors, and pink diamonds indicates the peak for the TO scans at Γ . The red arrows indicate where the avoid crossing between LA and TO modes occurs. From ref.[19]

fact, it was found that the transition temperature of SnTe depends strongly on the sample doping. Furthermore, since stoichiometric SnTe does not exist in nature due to Te vacancies [50], a careful analysis of the doping is crucial. An interesting study made by Brillson et al.[23] evaluated T_c in function of carrier concentrations via Raman scattering experiments. Since the rock-salt structure does not have Raman active modes no signal is obtained. However, when the ferroelectric transition occurs they were capable to observe the Raman signature of the rhombohedral structure.

A more in depth study as later performed by Kobayashi et al.[28] in which measurements of the electrical resistivity and Hall coefficient as functions of temperature were made for p-type SnTe crystals with carrier concentrations ranging from $(1.2 - 7.7) \times 10^{20} \text{ cm}^{-3}$. Fig.(1.10) and Fig.(1.11) illustrates the T_c dependence on doping. The first shows the results obtained via the anomaly on the resistivity, and the second combines the first with INS, Raman, neutron Bragg reflection, and x-ray results.

1.4 Summary

In this chapter we discussed some experimental findings on PbTe and SnTe. We started with the different structures that these systems can assume de-

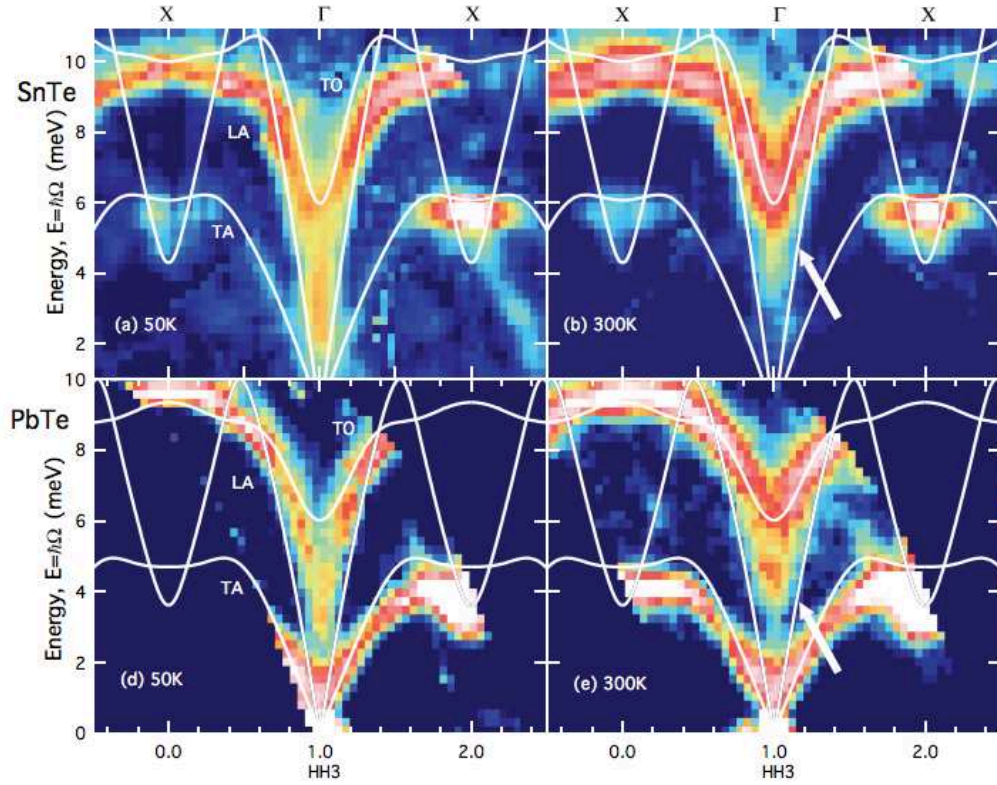


Figure 1.9: INS measurements of $S(\mathbf{q}, E)$ of SnTe. (a,b) $S(\mathbf{q}, E)$ measured at $T = 50$ and 300 K, respectively, along the $[H, H, 3]$ direction. White lines are renormalized phonon dispersion calculated at $T = 300$ K. Taken from [20]

pending on temperature and pressure. Then, we discussed their electronic properties and how it have been treated within the DFT framework. Finally, we discussed some of the main results on PbTe and SnTe lattice dynamical properties. The experiments discussed in this chapter demonstrate how anharmonicity manifests itself in these compounds, leading to a complex phonon spectra dependence on temperature, structural phase transitions for SnTe, and the presence of satellite peaks on the neutron scattering function of PbTe.

In this spirit, on the next two chapter we will introduce the theoretical framework used in this thesis in order to investigate anharmonic effects in the lattice dynamical properties of materials.

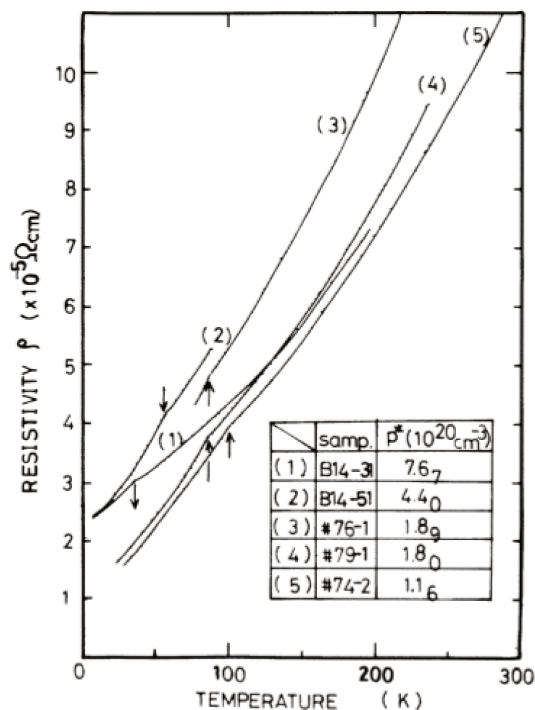


Figure 1.10: Resistivity measurements vs temperature of SnTe for various carrier concentrations from ref.[28]. The position of the kink in the curve indicates where the structural transition occurs.

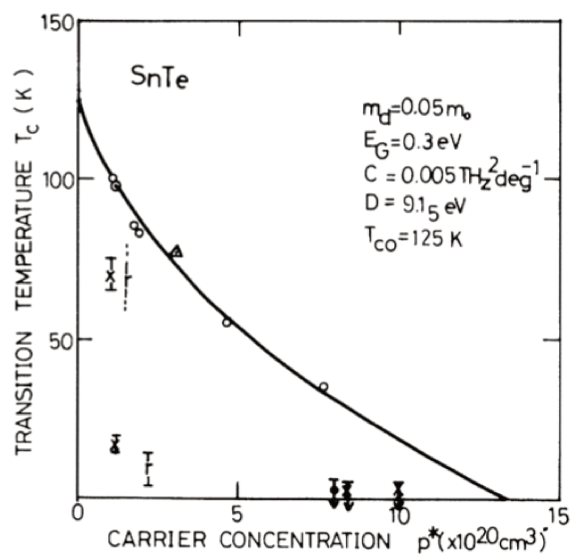


Figure 1.11: The transition temperature T_c , versus carrier concentration. resistivity (open dots); neutron Bragg reflection result (dot in circle); INS result (solid circle), x-ray results (crosses); Raman scattering results (r); anomaly position of Hall mobility at 77 K (triangle), theoretical curve obtained by a fit (solid lines). Taken from ref.[28]

Chapter 2

Dynamical properties of solids

In this chapter we describe the theoretical background and some concepts related to the evaluation of lattice-dynamical properties of solid. In order to be concise, we try to reduce the use of mathematical formalism. The majority of the condensed matters concepts discussed in this chapter are well-known and well documented [51, 52, 53].

The main objective of this chapter is to introduce briefly some key concepts concerning early developments of lattice-dynamical calculations. First, the general picture is introduced, followed by the ionic Hamiltonian and the harmonic approximation. Next, the density functional perturbation theory is presented.

Unless we state otherwise, throughout the sections introducing the methodology used in this thesis, we adopt atomic units (a.u.), so that $e = \hbar = m_e = 4\pi\epsilon_0 = 1$. In addition, considering that magnetism is not studied, spin degrees of freedom are not considered throughout.

2.1 Lattice dynamics

2.1.1 The general picture

We can think of matter as an ensemble of interacting atoms, sometimes under the influence of an external field. In order to describe its physical and chemical properties, one can treat it as a collection of atomic nuclei and electrons interacting via Coulomb electrostatic forces. The Hamiltonian for such system can be expressed on the following way:

$$\begin{aligned}
\hat{H} &= \hat{T}_{ion} + \hat{T}_e + \hat{V}_{ion,ion} + \hat{V}_{e,e} + \hat{V}_{e,ion} \\
&= \sum_I^{N_{ion}} \frac{1}{2M_I} \hat{\mathbf{P}}_I^2 + \sum_i^{N_e} \frac{1}{2} \hat{\mathbf{p}}_i^2 + \frac{1}{2} \sum_{I \neq J}^{N_{ion}} \frac{Z_I Z_J}{|\hat{\mathbf{R}}_I - \hat{\mathbf{R}}_J|} \\
&\quad + \frac{1}{2} \sum_{i \neq j}^{N_e} \frac{1}{|\hat{\mathbf{r}}_i - \hat{\mathbf{r}}_j|} - \frac{1}{2} \sum_{i,I}^{N_e, N_{ion}} \frac{Z_I}{|\hat{\mathbf{r}}_i - \hat{\mathbf{R}}_I|},
\end{aligned} \tag{2.1}$$

where \hat{T}_{ion} and \hat{T}_e are the kinetic-energy operators for the ions and electrons, respectively; $\hat{V}_{ion,ion}$, $\hat{V}_{e,e}$, $\hat{V}_{e,ion}$ are the ion-ion interaction operator, electron-electron interaction operator, and ion-electron interaction operator, respectively. In Eq.(2.1), electrons are denoted by lower case subscripts and ions, with masses M_I and atomic numbers Z_I , by upper case subscripts. The quantities $\hat{\mathbf{r}}_i$ and $\hat{\mathbf{R}}_I$ are the position operators for the i th electron and I th ion, respectively. Then as well, the momentum operators of the i th electron and I th ion as $\hat{\mathbf{p}}_i$ and $\hat{\mathbf{P}}_I$, respectively. In the framework of quantum mechanics the properties of the system can be derived by solving the associated many-body Schroedinger equation,

$$\hat{H} |\Psi\rangle = E |\Psi\rangle \tag{2.2}$$

to find the total energy E and, the eigenstates $|\Psi\rangle$. The total many-body wavefunction depends on the position of all ions and electrons in the system as:

$$\langle \mathbf{r}, \mathbf{R} | \Psi \rangle = \Psi(\mathbf{r}, \mathbf{R}) = \Psi(\mathbf{r}_1, \dots, \mathbf{r}_{N_e}, \mathbf{R}_1, \dots, \mathbf{R}_{N_{ion}}). \tag{2.3}$$

From this point, let \mathbf{r} and \mathbf{R} represent the set of all electronic and ionic positions, respectively. Excluding cases with a very small number of particles, such as hydrogenoid atoms, the problem defined by (2.1) is almost impossible to treat within a fully quantum mechanical framework. Over the past century a lot of effort has been made in order to develop methodologies capable of solving numerically the many-body problem and find good results in relation to experiments. The evolution of computers and numerical algorithms has increased the precision as well the scalability of numerical calculations and still is a very active field of research. One of the most successful methods is the so called density functional theory, which will be discussed briefly on appendix A.

2.1.2 The ionic Hamiltonian

In order to decouple the electronic from the vibrational degrees of freedom in a solid, one can use the Born-Oppenheimer approximation [54]. Since the time scale associated to the motion of the ions is much slower than that associated with electrons, we can consider that the atoms are static at a given position, and the electronic part of the Hamiltonian can be solved with ionic positions as parameters. Hence, within this approximation, we can divide the Hamiltonian in an electronic and ionic parts, $\hat{H}_{BO} = \hat{H}_e + \hat{H}_{ion}$. Assuming that the electronic Hamiltonian

$$\hat{H}_e = \hat{T}_e + \hat{V}_{e,ion} + \hat{V}_{e,e}, \quad (2.4)$$

has electronic eigenfunctions $\Psi_\alpha^e(\mathbf{r}, \mathbf{R})$ and eigenvalues $\mathcal{E}_\alpha^e(\mathbf{R})$, then using the Dirac notation, the Schroedinger equation for the electronic part is given as

$$\hat{H}_e |\Psi^e\rangle = \mathcal{E}^e(\mathbf{R}) |\Psi^e\rangle \quad (2.5)$$

Once this eigenvalue problem is solved, we have a starting point to determine the lattice-dynamical properties of a system. If the ionic potential is defined as

$$\hat{U}(\mathbf{R}) = \hat{V}_{ion,ion} + \mathcal{E}^e(\mathbf{R}), \quad (2.6)$$

the Hamiltonian related to ionic motion is rewritten as

$$\hat{H}_{ion} = \hat{T}_{ion} + \hat{U}(\mathbf{R}). \quad (2.7)$$

In writing this equation we have neglected mixed terms in the electron and phonons degrees of freedom since we are working under the framework of the Born-Oppenheimer approximation. Then, by solving the Schroedinger equation for the ions

$$\hat{H}_{ion} |\Psi^{ion}\rangle = \mathcal{E} |\Psi^{ion}\rangle \quad (2.8)$$

we find the ionic eigenfunctions $\Psi_\beta^{ion}(\mathbf{R})$ and eigenvalues \mathcal{E} . Therefore, within the Born-Oppenheimer approximation the total eigenfunctions is expressed as the product of the electronic and ionic wavefunction

$$\langle \mathbf{r}, \mathbf{R} | \Psi_\alpha^e, \Psi_\beta^{ion} \rangle = \Psi_\alpha^e(\mathbf{r}, \mathbf{R}) \Psi_\beta^{ion}(\mathbf{R}). \quad (2.9)$$

with

$$\langle \Psi_{\alpha'}^e, \Psi_{\beta'}^{ion} | \hat{H}_{BO} | \Psi_{\alpha}^e, \Psi_{\beta}^{ion} \rangle = \delta_{\alpha\alpha'} \delta_{\beta\beta'}, \quad (2.10)$$

meaning that the matrix elements of \hat{H}_{BO} is diagonal.

At this point, lets analyze closely the potential $\hat{U}(\mathbf{R})$ defined by (2.6). Let s denote an ion within the unit cell, \mathbf{R} a lattice vector, and α a Cartesian direction. Since ions generally vibrate around their equilibrium position $\mathbf{R}_{eq}^{s\alpha}$ determined by the minima of the BO energy surface, it is reasonable to expand the potential $\hat{U}(\mathbf{R})$ as a function of the ionic displacements from equilibrium $u_s^\alpha(\mathbf{R})$ as

$$\hat{U}(\mathbf{R}) = \hat{U}_0 + \sum_{n=2}^{\infty} \hat{U}_n \quad (2.11)$$

where

$$\hat{U}_n = \frac{1}{n!} \sum_{\alpha_1 \dots \alpha_n} \sum_{s_1 \dots s_n} \sum_{\mathbf{R}_1 \dots \mathbf{R}_n} \hat{u}_{s_1}^{\alpha_1}(\mathbf{R}_1) \dots \hat{u}_{s_n}^{\alpha_n}(\mathbf{R}_n) \phi_{s_1 \dots s_n}^{\alpha_1 \dots \alpha_n}(\mathbf{R}_1, \dots, \mathbf{R}_n). \quad (2.12)$$

and

$$\phi_{s_1 \dots s_n}^{\alpha_1 \dots \alpha_n}(\mathbf{R}_1, \dots, \mathbf{R}_n) = \left[\frac{\partial^{(n)} U(\mathbf{R})}{\partial u_{s_1}^{\alpha_1}(\mathbf{R}_1) \dots \partial u_{s_n}^{\alpha_n}(\mathbf{R}_n)} \right]_0 \quad (2.13)$$

In equation (2.12) α represents Cartesian coordinates, the quantity $\phi_{s_1 \dots s_n}^{\alpha_1 \dots \alpha_n}(\mathbf{R}_1, \dots, \mathbf{R}_n)$ is the n -body, or n th order force-constants and represents the n th derivative of the total energy with respect to the ionic displacements.

The first term of this expansion is a constant, the first order contribution vanishes since it is proportional to the forces acting on the ion in the equilibrium positions that, by default, are zero. By considering up to the second order contribution we are within the so called harmonic approximation [52, 55]. Therms beyond second order are associated to anharmonic effects.

2.2 Density functional perturbation theory (DFPT)

2.2.1 Dynamical matrix from the density response function

Even if the harmonic approximation give us a good starting point to study dynamical properties of materials, in order to evaluate the dynamical matrices we need to compute the derivatives of

$$U(\mathbf{R}) = \langle \Psi^{ion} | \hat{U}(\mathbf{R}) | \Psi^{ion} \rangle = V_{ion,ion} + \langle \Psi^e | \hat{H}_e(\mathbf{R}) | \Psi^e \rangle. \quad (2.14)$$

The first derivatives can be easily calculated by using the Hellmann-Feynman theorem [56]. The theorem states that the first derivative of the eigenvalues of a Hamiltonian, \hat{H}_λ , dependent on a parameter λ is given by the expectation value of the derivative of the Hamiltonian:

$$\frac{\partial E_\lambda}{\partial \lambda} = \langle \Psi_\lambda | \frac{\partial \hat{H}_\lambda}{\partial \lambda} | \Psi_\lambda \rangle \quad (2.15)$$

In this case, since the electronic Hamiltonian dependence on the ionic explicitly comes from the term $\hat{V}_{e,ion}$, we have

$$\frac{\partial U(\mathbf{R})}{\partial u_j^\beta} = \frac{\partial V_{ion,ion}}{\partial u_j^\beta} + \langle \Psi^e | \frac{\partial \hat{H}_e(\mathbf{R})}{\partial u_j^\beta} | \Psi^e \rangle = \frac{\partial V_{ion,ion}}{\partial u_j^\beta} + \int d\mathbf{r} n(\mathbf{r}, \mathbf{R}) \frac{\partial V_{e,ion}(\mathbf{r})}{\partial u_j^\beta} \quad (2.16)$$

where the electron-ion interaction between electron- i and ion- I can be viewed as an external one-body potential formed by the ionic background that acts on each electron independently as

$$V_{ext} = V_{e,ion}(\mathbf{r}), \quad (2.17)$$

with

$$V_{ext}(\mathbf{r}) = - \sum_I^{N_{ion}} \frac{Z_I}{|\mathbf{r} - \mathbf{R}_I|}, \quad (2.18)$$

and $n(\mathbf{r}, \mathbf{R})$ is the ground state electron charge density corresponding to the ionic configuration \mathbf{R} . In order to calculate the second derivatives at equilibrium, from Eq.(2.16) we have

$$\left[\frac{\partial^2 U(\mathbf{R})}{\partial u_I^\alpha \partial u_J^\beta} \right]_0 = \left[\frac{\partial^2 V_{ion,ion}}{\partial u_I^\alpha \partial u_J^\beta} \right]_0 + \int d\mathbf{r} \left[\frac{\partial n(\mathbf{r}, \mathbf{R})}{\partial u_I^\alpha} \right]_0 \left[\frac{\partial V_{ext}(\mathbf{r})}{\partial u_J^\beta} \right]_0 \quad (2.19)$$

$$+ \int d\mathbf{r} n(\mathbf{r}, \mathbf{R}) \left[\frac{\partial^2 V_{ext}(\mathbf{r})}{\partial u_I^\alpha \partial u_J^\beta} \right]_0$$

Equation (2.20) implies that the calculation of the second derivatives requires the evaluation of the ground-state electron charge density, $n(\mathbf{r}, \mathbf{R})$, as well as of its linear response to a distortion of the ionic geometry $\frac{\partial n(\mathbf{r}, \mathbf{R})}{\partial u_I^\alpha}$. The fundamental result above shows how one can extract the phonon spectrum via the electronic properties. This result was first reported by the end of the sixties by de Cicco and Johnson [57], and later by Pick, Cohen, and Martin [58].

As stated in section 2.1.2, the second derivatives of the potential give us the force constant matrices. We define the second order force constants $\mathbf{C}_{\alpha s, \beta s'}(\mathbf{R}_I - \mathbf{R}_J)$ as the sum of ionic and electronic contributions:

$$\mathbf{C}_{\alpha s, \beta s'}(\mathbf{R}_I - \mathbf{R}_J) = \mathbf{C}_{\alpha s, \beta s'}^{ion}(\mathbf{R}_I - \mathbf{R}_J) + \mathbf{C}_{\alpha s, \beta s'}^{elec}(\mathbf{R}_I - \mathbf{R}_J) \quad (2.20)$$

where

$$\mathbf{C}_{\alpha s, \beta s'}^{ion}(\mathbf{R}_I - \mathbf{R}_J) = \left[\frac{\partial^2 V_{ion,ion}}{\partial u_s^\alpha \partial u_{s'}^\beta} \right]_0; \quad (2.21)$$

$$\mathbf{C}_{\alpha s, \beta s'}^{elec}(\mathbf{R}_I - \mathbf{R}_J) = \int d\mathbf{r} \left[\frac{\partial n(\mathbf{r}, \mathbf{R})}{\partial u_s^\alpha} \right]_0 \left[\frac{\partial V_{ext}(\mathbf{r})}{\partial u_{s'}^\beta} \right]_0 \quad (2.22)$$

$$+ \int d\mathbf{r} n(\mathbf{r}, \mathbf{R}) \left[\frac{\partial^2 V_{ext}(\mathbf{r})}{\partial u_s^\alpha \partial u_{s'}^\beta} \right]_0.$$

Here, we denote \mathbf{R}_I as lattice vectors, α the cartesian coordinates, and s as the atoms in the cell. At this point, the only missing quantity that we have to calculate is the linear response of the electronic density to a phonon perturbation. On the next section we will discuss how one can obtain it via density functional perturbation theory. Once the force constant is fully determined, the harmonic phonon frequencies are then obtained by diagonalization of the dynamical matrix $D_{\alpha s, \beta s'}(\mathbf{q})$:

$$D_{\alpha s, \beta s'}(\mathbf{q}) = \frac{1}{\sqrt{M_s M_{s'}}} \mathbf{C}_{\alpha s, \beta s'}(\mathbf{q}), \quad (2.23)$$

where

$$\mathbf{C}_{\alpha s, \beta s'}(\mathbf{q}) = \sum_{\mathbf{R}} \mathbf{C}_{\alpha s, \beta s'}(\mathbf{R}) e^{i\mathbf{q} \cdot \mathbf{R}} \quad (2.24)$$

is the Fourier transform of the matrix of force constants, and M_I are the masses of the ions. In addition, we used translational invariance in order to express the force constants as a function of the generic lattice vector \mathbf{R} . With the dynamical matrix defined, then the eigenvalue problem

$$\sum_{\beta s'} D_{\alpha s, \beta s'}(\mathbf{q}) e_{\mathbf{q}v}^{\beta s'} = \omega_{\mathbf{q}v}^2 e_{\mathbf{q}v}^{\beta s'} \quad (2.25)$$

gives us the square of the frequencies $\omega_{\mathbf{q}v}^2$ and the polarization vectors $\mathbf{e}_{\mathbf{q}v}$ of mode v at momentum \mathbf{q} .

2.2.2 Density functional perturbation theory (DFPT)

On the previous section, we state that the second derivatives of the potential are determined by the electronic density linear response. In this section we will see how one can determine this response within the DFT formalism. The procedure described is the so called density functional perturbation theory (DFPT) [53, 59]. The main idea of this method is to use first order perturbation theory to investigate the Kohn-Sham orbitals variation when the ions are displaced from their equilibrium positions. The Kohn-Sham problem and the electronic density within its formulation is defined and discussed on appendix A. Considering the electronic density defined by the Kohn-Sham problem

$$n(\mathbf{r}, \mathbf{R}) = \sum_i^{N_{bands}} |\phi(\mathbf{r}, \mathbf{R})|^2, \quad (2.26)$$

where ϕ are the Kohn-Sham orbitals, the change in the density is

$$\Delta n(\mathbf{r}, \mathbf{R}) = 4Re \sum_{i=1}^{N/2} \phi_i^*(\mathbf{r}, \mathbf{R}) \Delta \phi_i(\mathbf{r}, \mathbf{R}) \quad (2.27)$$

Where the finite-difference operator Δ^λ is defined as

$$\Delta^\lambda F = \sum_i \frac{\partial F_\lambda}{\partial \lambda_i} \Delta \lambda_i. \quad (2.28)$$

We omit the superscript in Eq.(2.27) and on the subsequent formulas. This omission does not give rise to ambiguities on the development of the DFPT.

Since the imaginary part of the change in the density Eq.(2.27) vanishes, the prescription to keep only the real part can be dropped.

The variation of the Kohn-Sham orbitals is obtained by first order perturbation theory [60]:

$$(\hat{H}_{SCF} - \varepsilon_i) |\Delta\psi_i\rangle = -(\Delta\hat{H}_{SCF} - \Delta\varepsilon_i) |\psi_i\rangle \quad (2.29)$$

where

$$\hat{H}_{SCF}(\mathbf{r}) = -\frac{\nabla^2}{2} + V_{SCF}(\mathbf{r}) \quad (2.30)$$

is the unperturbed Kohn-Sham Hamiltonian,

$$\begin{aligned} \Delta V_{SCF}(\mathbf{r}) = & \Delta V_{ext}(\mathbf{r}) + \int \frac{n(\mathbf{r}', \mathbf{R}) d\mathbf{r}'}{|\mathbf{r} - \mathbf{r}'|} \\ & + \left[\frac{dv_{xc}(n)}{dn} \right]_{n=n(\mathbf{r}, \mathbf{R})} \Delta n(\mathbf{r}, \mathbf{R}), \end{aligned} \quad (2.31)$$

is the first order correction to the self-consistent potential, and $\Delta\varepsilon_i = \langle \phi_i | \Delta V_{SCF}(\mathbf{r}) | \phi_i \rangle$ is the first order variation of the Kohn-Sham eigenvalue ε_i . Equation (2.29) is analogous to the Sternheimer [61] equation within the context of atomic physics. Remarkably Eqs.(2.26) to (2.32) form a set of selfconsistent equations for the perturbed system. Hence, in order to obtain the change in density, it is possible to follow a self-consistent approach. The first-order correction to a given eigenfunction of the Schrödinger equation, given by Eq.(2.29), can be expressed in terms of a sum over the spectrum of the unperturbed Hamiltonian

$$\Delta\phi_i(\mathbf{r}, \mathbf{R}) = \sum_{j \neq i} \phi_j(\mathbf{r}, \mathbf{R}) \frac{\langle \phi_j(\mathbf{r}, \mathbf{R}) | \Delta V_{SCF} | \phi_i(\mathbf{r}, \mathbf{R}) \rangle}{\varepsilon_i - \varepsilon_j}. \quad (2.32)$$

Using Eq.(2.32), the electron charge-density response can be written as

$$\Delta n(\mathbf{r}, \mathbf{R}) = 4 \sum_{i=1}^{N/2} \sum_{j \neq i} \phi_i^*(\mathbf{r}, \mathbf{R}) \phi_j(\mathbf{r}, \mathbf{R}) \frac{\langle \phi_j(\mathbf{r}, \mathbf{R}) | \Delta V_{SCF} | \phi_i(\mathbf{r}, \mathbf{R}) \rangle}{\varepsilon_i - \varepsilon_j}. \quad (2.33)$$

It is important to state that the equation above can be recast in a form in which we do not have to estimate the change in the unoccupied states,

since only occupied states contribute to the change in the density. On the other hand, this statement is valid when for the insulating case only. A deeper discussion can be found on the DFPT review paper written by Baroni et al. In practice, the DFPT is an widely used method in order to evaluate lattice-dynamical properties of solids. However, its accuracy is dependent on the quality of the *ab-initio* calculations, leading to some errors for more complex systems and when anharmonicity is not negligible. Throughout this thesis, specially when discussing the results, we will refer to the calculations of the phonon dispersion curves made using the DFPT as harmonic calculations.

2.2.3 Born effective charges

In this section we will make some comments on how one can evaluate the Born effective charges within the linear response framework [59]. The knowledge of this quantity is particularly important in order to treat polar semiconductors, and to describe some effects such as the LO-TO splitting.

In polar semiconductors, since the Coulomb forces are long range, in the limit $\mathbf{q} \rightarrow 0$, a macroscopic electric fields rise for longitudinal optic phonons (LO). For finite \mathbf{q} , polar semiconductors are dealt with in the same way as nonpolar ones. In the long-wavelength limit, however, the macroscopic electric field \mathbf{E} , which accompanies the lattice distortion must be treated with care since the associated electronic potential $\Phi(\mathbf{r}) = -\mathbf{E} \cdot \mathbf{r}$ is not lattice-periodic. Within linear-response theory, electric fields can be dealt with during the self-consistent process performed to determine the density response to ionic displacements. One can treat long-wave vibrations in polar semiconductors by exploiting the known analytic properties of the dynamical matrix

$$\mathbf{C}_{\alpha I, \beta J}(\mathbf{q}) = \mathbf{C}_{\alpha I, \beta J}^{an}(\mathbf{q}) + \mathbf{C}_{\alpha I, \beta J}^{na}(\mathbf{q}), \quad (2.34)$$

where the analytic part $\mathbf{C}_{\alpha I, \beta J}^{an}(\mathbf{q})$ is the matrix obtained from the response to a zone-center phonon, calculated with boundary conditions corresponding to the absence of a macroscopic electric field. These conditions are implicitly assumed during electronic-structure calculations with periodic boundary conditions for the electronic wave functions. The nonanalytic part is generally expressed in terms of the high-frequency static dielectric tensor $\overset{\leftrightarrow}{\epsilon}^{\infty}$ and the Born effective charges tensor \mathbf{Z}_I^* as

$$\mathbf{C}_{\alpha I, \beta J}^{na}(\mathbf{q}) = \frac{4\pi}{\Omega} \frac{(\mathbf{q} \cdot \mathbf{Z}_I^*)_{\alpha} (\mathbf{q} \cdot \mathbf{Z}_J^*)_{\beta}}{\mathbf{q} \cdot \overset{\leftrightarrow}{\epsilon} \cdot \mathbf{q}}, \quad (2.35)$$

with I denoting the I th atom in the unit cell and Ω is the volume of the unit cell.

The Born effective charges are related to the total macroscopic polarization \mathbf{P}^{tot} induced by a zone center phonon considering zero electric boundary conditions, and are defined as

$$\mathbf{Z}_{I, \alpha\beta}^* = \Omega \frac{\partial \mathbf{P}_{\alpha}^{tot}}{\partial u_{\beta I q=0}}, \quad (2.36)$$

where $u_{\beta I q=0}$ is the amplitude of the zero-center phonon,

$$u_{\beta I}(\mathbf{R}) = u_{\beta I \mathbf{q}} e^{i\mathbf{q} \cdot \mathbf{R}}. \quad (2.37)$$

Since the total macroscopic polarization can be fully determined via linear response, the evaluation of the Born effective charges, as well the dielectric tensor, is achieved. This leads to the full knowledge of the force constant matrix $\mathbf{C}_{\alpha I, \beta J}(\mathbf{q})$, allowing then the calculation of vibrational properties for polar semiconductors.

Chapter 3

Anharmonicity

In the previous chapter we discussed how the lattice dynamical properties of solids can be evaluated within the harmonic framework. However, for systems in which anharmonic effects are not negligible, the harmonic approximation does not give reliable results, failing to describe phenomena such as phonon scattering times, finite thermal conductivity, phonon and linewidths.

In this chapter we will introduce the methods used in this thesis to include anharmonicity in our calculations. We begin by commenting on anharmonic effects, after we discuss how third order contributions can be calculated, and then, used to estimate phonons lineshifts, linewidths, and the spectral function. After, we discuss the self-consistent harmonic approximation, and its stochastic implementation that allows one to assess the third and fourth order dynamical matrices, anharmonic phonon dispersion, as well to investigate the presence of displacive second-order phase transitions.

3.1 Anharmonic effects

On the harmonic approximation we assume that the ions oscillate with a small amplitude in relation to their equilibrium positions. This assumption seems to be adequate for a large number of compounds for temperatures below the melting point. However, even if the theory can describe phonon frequencies and its associated physical properties, a fully harmonic theory fails to describe other physical phenomena since it takes on account only up to the quadratic terms on the ionic potential.

Within the harmonic approximation the Hamiltonian is diagonalized in terms of phonons that do not interact with each other leading to infinite

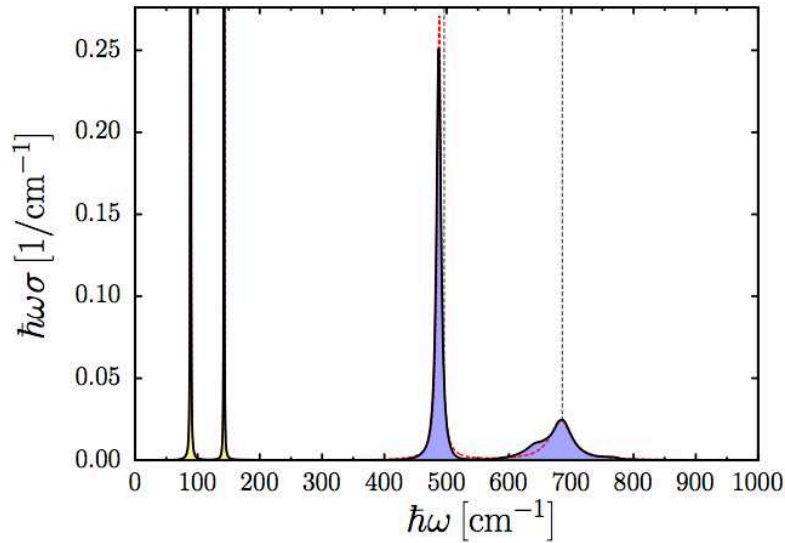


Figure 3.1: Slice of the spectral function of PdH at 80 K, $\mathbf{q} = 0, 0, \frac{1}{2}$ [62]. It is noticeable that the phonons have a width related to anharmonic effects. The dashed lines represents the position of the modes.

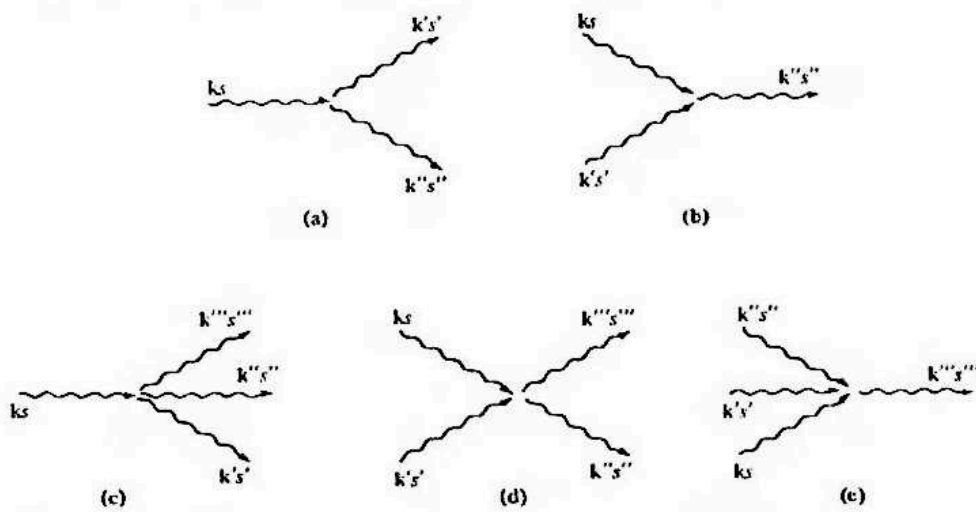


Figure 3.2: Processes produced in lowest-order perturbation theory by cubic and quartic anharmonic terms. (a) Cubic: one phonon decays into two. (b) Cubic: two phonons merge into one. (c) Quartic: one phonon decays into three. (d) Quartic: two phonons turn into two others (phonon-phonon scattering). (e) Quartic: three phonons merge into one. Taken from ref.[55]

lifetimes and the absence of phonon decay [55]. Hence, in neutron scattering experiments, on insulators, the scattering cross section for a fixed momentum transfer \mathbf{q} as a function of energy transfer is composed of delta functions centered at the $\omega_\mu(\mathbf{q})$ frequencies. On the other hand, in the mea-

sured spectra the peaks have an noticeable width which is directly related to the anharmonic contribution to the ionic potential. In addition, due to the nature of the harmonic phonons an harmonic crystal has a infinite thermal conductivity, which cannot exist in nature.

Therefore, to include higher order terms in \hat{H}_{ion} , it is necessary to search for suitable many-body approaches that include interacting phonons, since the Hamiltonian is no further diagonalizable. The diagrams in Fig.(3.2) are some examples of phonon-phonon interactions which depend directly on the number of anharmonic terms included in the Hamiltonian. In the next chapter we will discuss more on some ways phonons interact with each other and how we can treat this interaction.

3.2 Thermal expansion and the Quasi-Harmonic Approximation

Among the approaches aimed to calculate temperature dependent structural properties of solids, the quasi-harmonic approximation (QHA) provides reliable results for a large variety of compounds [63]. In this approximation, the Helmholtz free energy, F of a system is given by

$$F(T, \mathbf{a}) = E(\mathbf{a}) + k_B T \sum_{vq} \log \left[2 \sinh \left(\frac{\omega_{vq}(\mathbf{a})}{2k_B T} \right) \right], \quad (3.1)$$

where $E(\mathbf{a})$ is the static energy of the crystal, T is the temperature, k_B is the Boltzmann constant, and $\omega_{vq}(\mathbf{a})$ are the vibrational frequencies of the system as a function of the structural parameters \mathbf{a} . Particularly, QHA calculations can be quite accurate since the frequencies used in Eq.(3.1) may be determined via DFPT calculations. On the other hand, its validity depends on the magnitude of the anharmonic contribution. This method requires the absence of imaginary phonon frequencies, and thus can not describe structural transitions. In addition, the QHA must be applied for a range of temperatures below the melting point. Fig(3.3) and Fig(3.4) illustrates the case of PbTe in which even if the phonon eigenvalues are not imaginary, the QHA breaks down due to its strong anharmonicity.

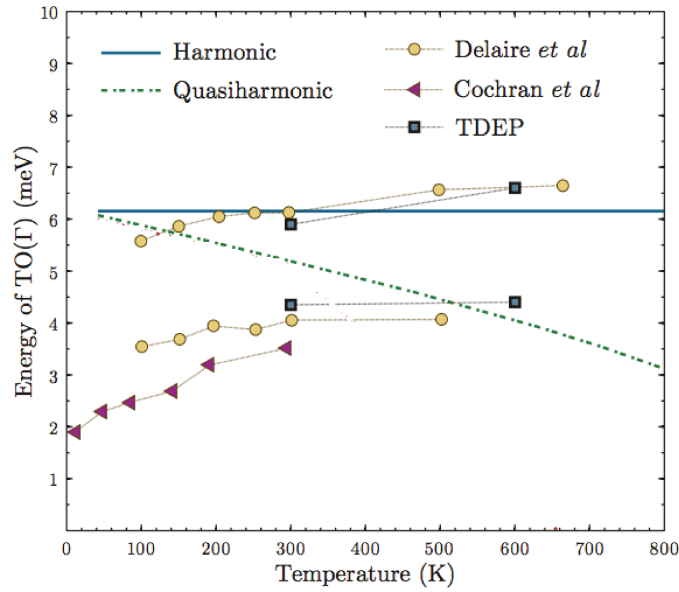


Figure 3.3: Energy of the transverse optical (TO) mode at zone center of PbTe at different temperatures. It is noticeable that the QHA approximation fails to describe the dependence on temperature for the TO mode. From ref.[64]

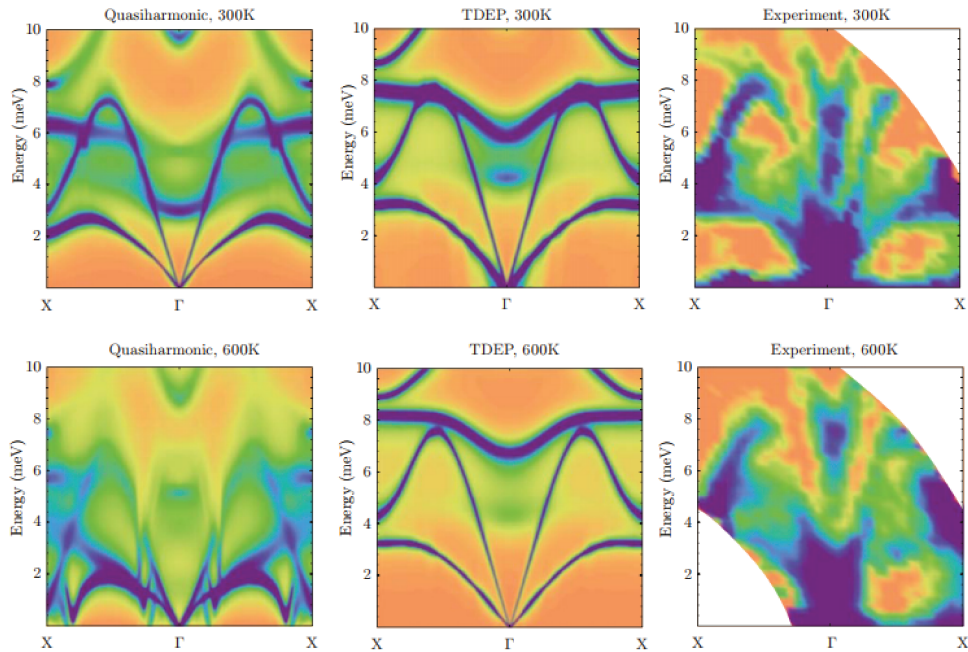


Figure 3.4: Comparison between QHA, TDEP, and experimental cross sections for PbTe. Since anharmonic effects are strong in this compound, the QHA breaks down, predicting even structural instabilities for $T = 600$ K, which is in disagreement with experimental data. From ref.[64]

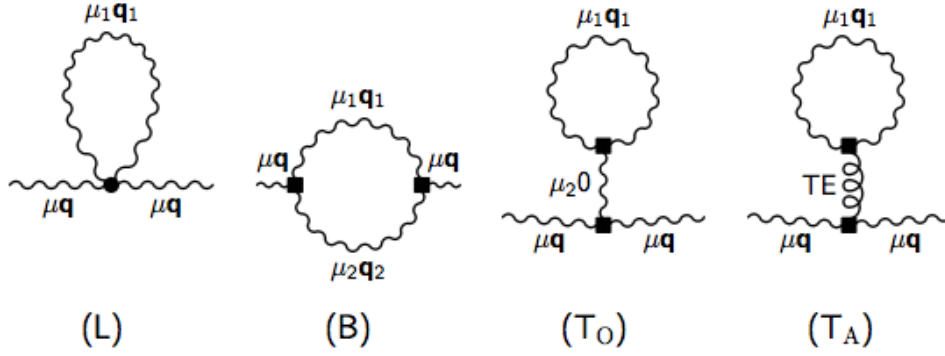


Figure 3.5: The self-energy Feynman diagrams which contribute to the total self energy $\Pi_\mu(\mathbf{q}, \omega)$ at the perturbative level [62]. The loop (L), the bubble (B), and tadpole (T) diagrams. The tadpole is divided into two optical (To) and acoustic (Ta) contributions. The latter accounts for thermal expansion (TE). The dot and squares denote a fourth-order, and third order vertex, respectively.

3.3 Perturbation theory and anharmonic effects

3.3.1 Phonon self-energies, linewidth, and lineshifts

When dealing with weak anharmonicity, a natural first approach is to treat it via perturbation theory. At lowest order, the harmonic phonon self energy is corrected by the Feynman self-energy diagrams shown in Fig.(3.5), the loop (L), bubble (B), and tadpole diagrams (T). The real part of the diagrams is responsible for a change on the phonon frequencies, the phonon lineshift; while the imaginary part is responsible for the broadening of the phonon branches, the phonon linewidth. The three phonon process linked to the bubble diagram has both imaginary and real parts, contributing to both lineshift and linewidth. The remaining diagrams only affects the change of phonon frequencies.

Their contribution to the self-energy are given by [62, 65, 66, 67, 68]

$$\Pi_\mu^L(\mathbf{q}, \omega) = \frac{1}{2N} \sum_{\mathbf{q}_1 \mu_1} \phi_{\mu\mu\mu_1\mu_1}(-\mathbf{q}, \mathbf{q}, \mathbf{q}_1, -\mathbf{q}_1) [2n_B(\omega_{\mu_1}(\mathbf{q}_1)) + 1], \quad (3.2)$$

$$\Pi_\mu^B(\mathbf{q}, \omega) = -\frac{1}{2N} \sum_{\substack{\mathbf{q}_1 \mathbf{q}_2 \\ \mu_1 \mu_2}} \sum_{\mathbf{G}} \delta_{-\mathbf{q}+\mathbf{q}_1+\mathbf{q}_2, \mathbf{G}} |\phi_{\mu\mu_1\mu_2}(-\mathbf{q}, \mathbf{q}, \mathbf{q}_2)|^2 F(\omega, \omega_{\mu_1}(\mathbf{q}_1), \omega_{\mu_2}(\mathbf{q}_2)), \quad (3.3)$$

$$\Pi_{\mu}^T(\mathbf{q}, \omega) = \frac{1}{N} \sum_{\substack{\mathbf{q}_1 \\ \mu\mu_1\mu_2}} \phi_{\mu\mu\mu_2}(-\mathbf{q}, \mathbf{q}, 0) \phi_{\mu_1\mu_1\mu_2}(-\mathbf{q}_1, \mathbf{q}_1, 0) \frac{2n_B(\omega_{\mu_1}(\mathbf{q}_1)) + 1}{\omega_{\mu_2}(0)}, \quad (3.4)$$

where

$$F(\omega, \omega_{\mu_1}(\mathbf{q}_1), \omega_{\mu_2}(\mathbf{q}_2)) = \left[\frac{2(\omega_1 + \omega_2)[1 + n_B(\omega_1) + n_B(\omega_2)]}{(\omega_1 + \omega_2)^2 - (\omega + i\delta)^2} \right] + \left[\frac{2(\omega_1 - \omega_2)[n_B(\omega_2) - n_B(\omega_1)]}{(\omega_2 - \omega_1)^2 - (\omega + i\delta)^2} \right], \quad (3.5)$$

$n_B(\omega) = 1/(e^{\beta\omega} - 1)$ is the bosonic occupation factor, \mathbf{G} is a reciprocal lattice vector, and N the number of unit cells in the system. Hence,

$$\Pi_{\mu}(\mathbf{q}, \omega) = \Pi_{\mu}^L(\mathbf{q}, \omega) + \Pi_{\mu}^B(\mathbf{q}, \omega) + \Pi_{\mu}^T(\mathbf{q}, \omega) \quad (3.6)$$

is the total self-energy at the perturbative level.

As shown in equations (3.2) to (3.4) to calculate the different contribution to the self-energy one needs to calculate the third and fourth order force constants. Several approaches have emerged in order to compute the third-order derivatives via the $2n + 1$ theorem [69, 70, 71, 72] and using finite differences [73]. However, the fourth-order term are more complicate to evaluate since the the number of fourth-order derivatives quickly increases with the number of atoms. Hence, the perturbative evaluation of the loop diagram is only affordable for few-atom highly symmetric cells. By consequence, new approaches to calculate the fourth-order contribution are needed.

The tadpole diagrams are related to the relaxation of internal structural parameters, as well the cell parameters. Usually, these diagrams can be taken on account by using the QHA framework[74].

The bubble contribution is the only one that contributes to the phonon linewidth. When the phonon self-energy is small with respect to the harmonic frequencies, $|\Pi_{\mu}(\mathbf{q}, \omega)| \ll \omega_{\mu}(\mathbf{q})$, the half-width at half maximum of phonon μ with momentum \mathbf{q} is given by the imaginary part of the bubble self-energy term is given as

$$\Gamma_{\mu}^{ph-ph}(\mathbf{q}) = -\text{Im}\Pi_{\mu}^B(\mathbf{q}, \omega_{\mu}(\mathbf{q})). \quad (3.7)$$

The real parts of the bubble and loop diagrams give the shift of the

phonon frequencies due to phonon-phonon interaction as

$$\Delta_\mu(\mathbf{q}) = \text{Re}[\Pi_\mu^L(\mathbf{q}, \omega_\mu(\mathbf{q})) + \Pi_\mu^B(\mathbf{q}, \omega_\mu(\mathbf{q}))] \quad (3.8)$$

3.3.2 Perturbation theory validity

The perturbative approach to treat anharmonicity relies on the limit where $|\Pi_\mu(\mathbf{q}, \omega)| \ll \omega_\mu(\mathbf{q})$. However, when $\omega_\mu(\mathbf{q})$ becomes very small or imaginary then this condition is violated and perturbation theory breaks down. This is the case for many ferroelectrics, thermoelectrics [20, 19], and materials which exhibit charge-density wave effects [75]. For those cases, in order to calculate the anharmonic renormalized phonon frequencies, linewidths, and lineshifts one needs to go beyond perturbation theory.

Among the most non-perturbative treatments of anharmonicity, we can mention the self-consistent ab initio lattice dynamics (SCAILD) method [76], which is an iterative way of converging the phonon frequencies at different temperatures accounting for anharmonic effects. However, it does not optimize the eigenvectors of the harmonic potential nor the internal parameters in the crystal or molecular structure, and does not include anharmonic corrections in the free energy. The temperature dependent effective potential (TDEP) [77], that has been successfully applied to study a large diversity of materials, including thermoelectric compounds. This technique can optimize the potential with respect to both polarization vectors and internal parameters, and, in principle, can include anharmonic corrections. However, since it is based on ab-initio molecular dynamics (AIMD) calculations, it lacks quantum effects and it might break down at low temperatures. Finally, the method we used in this thesis, the stochastic self-consistent harmonic approximation (SSCHA)[16, 17, 18]. This method is based on the self-consistent harmonic approximation (SCHA) [78] and aims to overcome the limitations of the perturbation theory and AIMD based methods. On the next section we will describe its formulation following close the key articles published by Errea [16, 17], and Bianco [18].

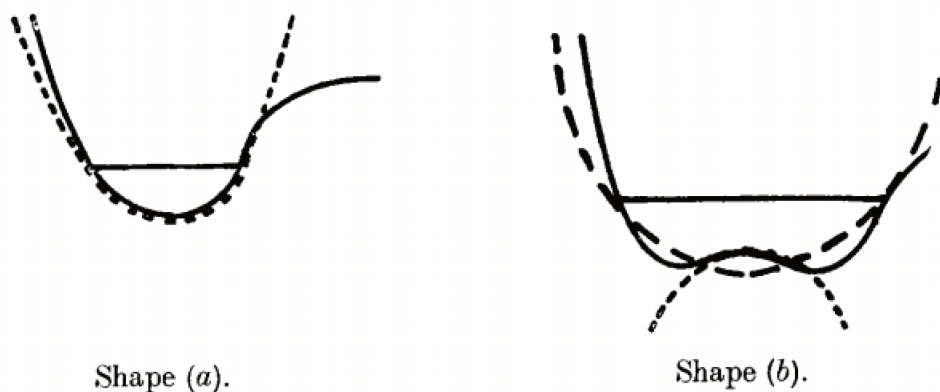


Figure 3.6: The shape (a) illustrates the vibrational problem of a molecule. When vibrations are small only the bottom of the well comes in, so in this case the harmonic approximation (dotted curve) is reasonable. If the well has a different shape, shape (b) for example, the harmonic approximation breaks down (dotted curve). However, a pseudo-harmonic approximation is still possible with a harmonic oscillator wave-function and the frequency parameter fitted by a variational principle equivalent to the fixing of average position and mean-square deviation (dashed curve). Taken from [78]

3.4 Stochastic self-consistent harmonic approximation

3.4.1 Self-consistent harmonic approximation

The main idea of the SCHA is that one can approximate the real free energy of a system by choosing an appropriate harmonic free energy. However, this free energy is different from the one obtained making use of the second derivatives of the Born-Oppenheimer potential $U(\mathbf{R})$. Fig(3.6) illustrates this idea using two different potentials.

For a given temperature T , the free energy of the ionic Hamiltonian is given by adding the total energy and the entropic contributions,

$$F_{\hat{H}} = \text{tr}[\rho_H H] + \frac{1}{\beta} \text{tr}[\rho_H \ln \rho_H], \quad (3.9)$$

where $\rho_H = e^{-\beta H} / \text{tr}[e^{-\beta H}]$ is the density matrix and $\beta = 1/(k_b T)$ with k_b being the Boltzmann constant. The direct evaluation of the free energy $F_{\hat{H}}$ can be quite cumbersome due to the many-body nature of the ionic potential. Hence, within the SCHA, a trial Hamiltonian $\mathcal{H} = T + \mathcal{U}$ defines a new trial density matrix $\rho_{\mathcal{H}}$ which replaces ρ_H , defining also a variational principle. Then, with the auxiliary free energy $\mathcal{F}_{\mathcal{H}}[\mathcal{H}]$ as

$$\mathcal{F}_{\mathcal{H}}[\mathcal{H}] = \text{tr}[\rho_{\mathcal{H}}H] + \frac{1}{\beta}\text{tr}[\rho_{\mathcal{H}} \ln \rho_{\mathcal{H}}], \quad (3.10)$$

The Gibbs-Bogoliubov (GB) variational principle states that

$$F_H \leq \mathcal{F}_H[\mathcal{H}] = F_{\mathcal{H}} + \text{tr}[\rho_{\mathcal{H}}(U - \mathcal{U})]. \quad (3.11)$$

Hence, by minimizing $F_{\mathcal{H}}$ with respect to the trial Hamiltonian \mathcal{H} , a good approximation for the free energy is obtained. It has been shown by Errea et al, that this minimization can be done using a conjugate-gradient algorithm if one has the knowledge of the total energy and forces. Within the SCHA, even if the variation principle in Eq.(3.11) is valid for any trial potential \mathcal{U} , as proposed originally by Hooton [78], we restrict the choice of \mathcal{U} to an harmonic potential parametrized in terms of the vector \mathcal{R} (the centroids) of dimension $3N_a$, with N_a corresponding to the number of atoms, and by the square positive-definite matrix $\Phi(\mathcal{R})$ of order $3N_a$ as:

$$\mathcal{U}_{\mathcal{R},\Phi} = \frac{1}{2} \sum_{ab} \Phi_{ab} (R - \mathcal{R})^a (R - \mathcal{R})^b, \quad (3.12)$$

where \mathcal{R} corresponds to the average position of the atoms for the trial density matrix $\rho_{\mathcal{H}}$, namely 'centroids'. From this point, let \mathbf{R} denote in component-free notation the quantity $R^{\alpha s}(\mathbf{l})$, which is a collective coordinate that specifies unambiguously the atomic configuration. The indexes α , s , and \mathbf{l} represent the Cartesian directions, the atom within the unit cell, and the three dimensional lattice vector, respectively. The past convention will also be applied to the centroids. In what follows we will also use a single composite index $a = (\alpha, s, \mathbf{l})$ to indicate Cartesian index, atom index and lattice vector together. In addition, throughout this section, we will use bold letters to indicate also other quantities in component-free notation.

We define $\Phi(\mathbf{R})$ as the SCHA square matrix which minimizes the functional $\mathcal{F}_H[\mathcal{H}]$, giving the best approximation for a given configurations of the centroids \mathcal{R} . This matrix satisfies the relation:

$$\Phi = \left\langle \frac{\partial^2 U}{\partial \mathbf{R} \partial \mathbf{R}} \right\rangle_{\rho_{\mathcal{H},\mathcal{R}}}; \quad (3.13)$$

where the average has to be understood as a quantum thermal average over the density matrix $\rho_{\mathcal{H}}$.

3.4.2 Structural second order phase transition, and the free energy curvature

In second order phase transitions associated to the atomic positions, such as ferroelectric and charge-density wave transitions, the centroids \mathcal{R} are suitable quantities in order to define an order parameter Q , which is the observable measured in diffraction experiments.

Landau's theory of second order phase transitions [79] states that the free energy $F(\mathcal{R})$ minimum, for temperatures above the transition temperature T_c , is achieved when the system is in a high symmetry phase i.e. in a equilibrium configuration \mathcal{R}_{hs} for the given temperature T . When T is lowered and reaches T_c , the minimum becomes less distinct, turning into a saddle point. By lowering the temperature further, $T < T_c$, the system assumes less symmetric equilibrium configurations $\mathcal{R}(T)$, in which the free energy is smaller. Therefore, the Hessian of the free energy with respect to the centroids of the high temperature phase is the meaningful parameter to study to detect phase transitions. Fig.(3.7) illustrates the process described above.

The SSCHA free-energy Hessian in a centroid position \mathcal{R} can be computed using the analytical formula (in component-free notation):

$$\frac{\partial^2 F}{\partial \mathcal{R} \partial \mathcal{R}} = \Phi + \overset{(3)}{\Phi} \Lambda(0) \left[\mathbb{1} - \overset{(4)}{\Phi} \Lambda(0) \right]^{-1} \overset{(3)}{\Phi}, \quad (3.14)$$

where Φ is given in Eq. 3.13 while $\overset{(3)}{\Phi}$ and $\overset{(4)}{\Phi}$ correspond to third and fourth order SSCHA tensors respectively. Those quantities can be defined by generalizing Eq. (3.13) to high orders:

$$\overset{(n)}{\Phi}_{a_1 \dots a_n}(\mathcal{R}) = \left\langle \frac{\partial^n U}{\partial R^{a_1} \dots \partial R^{a_n}} \right\rangle_{\rho \mathcal{H}} \quad (3.15)$$

In Eq.(3.14) the value at $z = 0$ of the 4th-order tensor $\Lambda(z)$ is used. For a generic complex number z it is defined, in components, by

$$\Lambda^{abcd}(z) = -\frac{1}{2} \sum_{\mu\nu} F(z, \omega_\mu, \omega_\nu) \times \sqrt{\frac{\hbar}{2M_a \omega_\mu}} e_\mu^a \sqrt{\frac{\hbar}{2M_b \omega_\nu}} e_\nu^b \sqrt{\frac{\hbar}{2M_c \omega_\mu}} e_\mu^c \sqrt{\frac{\hbar}{2M_d \omega_\nu}} e_\nu^d, \quad (3.16)$$

with M_a the mass of the atom a , ω_μ^2 and e_μ^a eigenvalues and corresponding

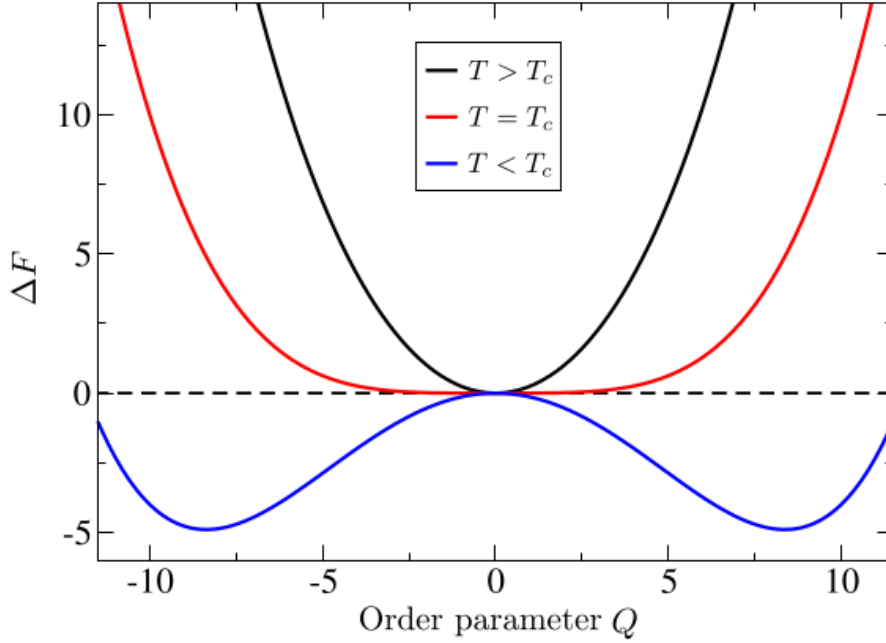


Figure 3.7: Second-order phase transition, as described by Landau's theory. Q is a macroscopic, scalar, order parameter identifying a system configuration. We consider a situation in which the symmetry $Q \rightarrow -Q$ holds. When $Q = 0$ the system assumes a high-symmetry phase. $\Delta F(Q) = F(Q) - F(0)$ is the difference between the free energy of phase Q and the free energy of the high-symmetry phase, for a given temperature T . For each T , $\Delta F(Q)$ has a minimum in the equilibrium configuration $Q_{eq}(T)$. For temperatures above the critical temperature; $T > T_c$, the free energy has a minimum in $Q_{eq}(T) = 0$. For temperatures below the critical temperature; $T < T_c$, $Q = 0$ becomes a local maximum, whereas the minimum $Q_{eq}(T)$ acquires two opposite degenerate values, different from zero. This fact can be visualized as noticing that the curve turns into a saddle. The order parameter $Q_{eq}(T)$ is a continuous function even during the transition. Figure taken from [18]

eigenvectors of $\Phi_{ab}/\sqrt{M_a M_b}$, respectively, and

$$F(z, \omega_\nu, \omega_\mu) = 2 \left[\frac{(\omega_\mu + \omega_\nu)[1 + n_B(\omega_\mu) + n_B(\omega_\nu)]}{(\omega_\mu + \omega_\nu)^2 - z^2} - \frac{(\omega_\mu - \omega_\nu)[n_B(\omega_\mu) - n_B(\omega_\nu)]}{(\omega_\mu - \omega_\nu)^2 - z^2} \right] \quad (3.17)$$

where $n_B(\omega) = 1/(e^{\beta\hbar\omega} - 1)$ is the bosonic occupation number. This relation is directly related to Eq.(3.6). In order to have a better visualization of the different terms of Eq.(3.14) one can rewrite it as:

$$\frac{\partial^2 F}{\partial \mathcal{R} \partial \mathcal{R}} = \Phi + \overset{(3)}{\Phi} \Lambda \overset{(3)}{\Phi} + \overset{(3)}{\Phi} \Lambda \Theta \Lambda \overset{(3)}{\Phi}, \quad (3.18)$$

where

$$\Theta = \left[\mathbb{1} - \begin{matrix} (4) \\ \Phi \Lambda \end{matrix} \right]^{-1} \begin{matrix} (4) \\ \Phi \end{matrix}. \quad (3.19)$$

For simplicity and to make the discussion of our results clearer, we define

$$\langle D3V \rangle = \begin{matrix} (3) \\ \Phi \Lambda \Phi \end{matrix} \quad (3.20)$$

$$\langle D4V \rangle = \begin{matrix} (3) \\ \Phi \Lambda \Theta \Lambda \Phi \end{matrix}. \quad (3.21)$$

We highlight these two terms in particular, since they will play a major role to explain the contribution to the calculated anharmonic phonon spectra of the systems studied in this thesis. If one is interested to understand better the calculation of the free-energy Hessian, a detailed derivation of Eq.(3.14) can be found on the paper by Bianco et.al. Here we simply recall that all quantities involved in Eq.(3.18) are obtained by a statistical sampling of $\rho_{\mathcal{H}}$ over randomly displaced atomic positions. The knowledge of forces on the displaced atomic configurations is sufficient to obtain both $\langle D3V \rangle$ and $\langle D4V \rangle$ as well as the Hessian of the free energy. Therefore, Eq.(3.14) allows the study of structural second order phase transitions by evaluating the second derivatives of $F(\mathcal{R})$. The additional terms beyond Φ allow the free energy Hessian elements to assume negative values.

3.4.3 Phonon quasiparticles

From the harmonic theory it is possible to define the zero temperature harmonic dynamical matrix on a similar fashion as we did for Eq.(2.23) as

$$D_{ab}^{(0)} = \frac{1}{\sqrt{M_a M_b}} \left. \frac{\partial^2 U}{\partial R^a \partial R^b} \right|_{\mathcal{R}_{(0)}}, \quad (3.22)$$

where $\mathcal{R}_{(0)}$ is the temperature-independent configuration for which $U(\mathbf{R})$ has a minimum. Hence, for each temperature, by considering the free energy Hessian in the corresponding equilibrium configuration \mathcal{R}_{eq} divided by the square root of the masses, we can define the generalization of Eq.(3.22) at finite temperature as:

$$D_{ab}^{(F)} = \frac{1}{\sqrt{M_a M_b}} \frac{\partial^2 F}{\partial \mathcal{R}^a \partial \mathcal{R}^b} \Big|_{\mathcal{R}_{eq}} = \quad (3.23)$$

$$= D_{ab}^{(S)} + \Pi_{ab}^{(S)}. \quad (3.24)$$

where the Hessian is obtained from Eq.(3.14) and $D_{ab}^{(S)} = \Phi_{ab}/\sqrt{M_a M_b}$. At this point the quantity $\Pi_{ab}^{(S)}$ has no particular physical meaning. However, later it will be interpreted as a self-energy.

It is worth to explore the limit case of Eq.(3.14) where $\overset{(4)}{\Phi}\Lambda$ is negligible with respect to the identity matrix. In this case the Hessian is given by the SCHA matrix plus the so-called "bubble" term $\overset{(3)}{\Phi}\Lambda\overset{(3)}{\Phi}$ only. With the dynamical matrices defined, the free-energy phonons can be obtained solving the eigenvalue equation

$$\sum_b D_{ab}^{(F)} \epsilon_\mu^b = \Omega_\mu^2 \epsilon_\mu^a, \quad (3.25)$$

where Ω_μ represents the phonon frequencies, and ϵ_μ^a the polarization vectors.

$$D_{ab}^{(S)} = \frac{1}{\sqrt{M_a M_b}} \Phi_{ab}(\mathcal{R}_{eq}). \quad (3.26)$$

3.4.4 SSCHA self-energies

in the context of the SSCHA it is possible to formulate an *ansatz* in order to give an approximate expression to the one-phonon Green function $\mathbf{G}(z)$ for the variable $\sqrt{M_a}(R^a - \mathcal{R}_{hs}^a)$

$$\mathbf{G}^{-1}(z) = z^2 \mathbf{1} - \mathbf{M}^{-\frac{1}{2}} \Phi \mathbf{M}^{-\frac{1}{2}} - \mathbf{\Pi}(z) = -\mathbf{D}^{(F)}, \quad (3.27)$$

where $\mathbf{\Pi}(z)$ is the SSCHA self-energy, given by

$$\mathbf{\Pi}(z) = \mathbf{M}^{-\frac{1}{2}} \overset{(3)}{\Phi}\Lambda(z) \left[\mathbf{1} - \overset{(4)}{\Phi}\Lambda(z) \right]^{-1} \overset{(3)}{\Phi}\mathbf{M}^{-\frac{1}{2}}, \quad (3.28)$$

where $M_{ab} = \delta_{ab} M_a$ is the mass matrix. When the term $\overset{(4)}{\Phi}\Lambda(z)$ is much smaller than the identity matrix the dynamical case reduces the SSCHA self-energy to the so-called *bubble* self-energy, namely

$$\mathbf{\Pi}(z) \approx \mathbf{\Pi}^{(B)}(z) = \mathbf{M}^{-\frac{1}{2}} \overset{(3)}{\Phi}\Lambda(z) \overset{(3)}{\Phi}\mathbf{M}^{-\frac{1}{2}}, \quad (3.29)$$

We then neglect the mixing between different phonon modes and assume that $\mathbf{\Pi}(z)$ is diagonal in the basis of the eigenvectors $e_{\mu}^{\alpha s}(\mathbf{q})$ of $\Phi_{\alpha s, \beta t}(\mathbf{q})/\sqrt{M_s M_t}$ where $\Phi_{\alpha s, \beta t}(\mathbf{q})$ is the Fourier transform of $\Phi_{\alpha s, \beta t}$. We then define

$$\Pi_{\mu}(\mathbf{q}, \omega) = \sum_{\alpha s, \beta t} e_{\mu}^{\alpha s}(\mathbf{q}) \Pi_{\alpha s \beta t}(\mathbf{q}, \omega + i0^+) e_{\mu}^{\beta t}(\mathbf{q}) \quad (3.30)$$

and $\omega_{\mu}^2(\mathbf{q})$ are the eigenvalues of the Fourier transform of $\mathbf{D}^{(S)}$. The phonon frequencies squared, $\Omega_{\mathbf{q}\mu}^2$, corrected by the *bubble* self-energy are then obtained as

$$\Omega_{\mathbf{q}\mu}^2 = \omega_{\mu}^2(\mathbf{q}) + \text{Re}\Pi_{\mu}(\mathbf{q}, \omega_{\mathbf{q}\mu}) \quad (3.31)$$

In studying the response of a lattice to neutron scattering we need the one-phonon spectral function. By using Eq. (3.27) for $\mathbf{G}(z)$ we can calculate the cross-section $\sigma(\omega) = -\omega \text{Tr Im } \mathbf{G}(\omega + i0^+)/\pi$, whose peaks signal the presence of collective vibrational excitations (phonons) having certain energies, as they can be probed with inelastic scattering experiments (here the chosen normalization factor is such that $\int d\omega \sigma(\omega)$ is equal to the total number of modes). Again, we take advantage of the lattice periodicity and we Fourier transform the interesting quantities with respect to the lattice indices. In particular, we consider the Fourier transform of the SSCHA self-energy, $\Pi_{\alpha s \beta t}(\mathbf{q}, z)$. Neglecting the mixing between different modes, the cross section is then given by

$$\sigma(\mathbf{q}, \omega) = \frac{1}{\pi} \sum_{\mu} \frac{-\omega \text{Im}\Pi_{\mu}(\mathbf{q}, \omega)}{(\omega^2 - \omega_{\mu}^2(\mathbf{q}) - \text{Re}\Pi_{\mu}(\mathbf{q}, \omega))^2 + (\text{Im}\Pi_{\mu}(\mathbf{q}, \omega))^2}. \quad (3.32)$$

3.5 Summary

In this chapter we discussed how one can treat anharmonicity within different frameworks. In this section, we will summarize some cases and for the sake of clarity, we will point out some of them that we considered in our preliminary investigations on anharmonic effects in PbTe and SnTe.

First, on the weak anharmonicity limit one can use directly perturbation theory as it is described via equations (3.2) to (3.4). Here, one must work on the limit $|\Pi_{\mu}(\mathbf{q}, \omega)| \ll \omega_{\mu}(\mathbf{q})$.

The second approach is to couple perturbation theory to the SSCHA

as done before in the literature. In this case the the loop and tadpole contributions are given by the SSCHA, and the bubble term is added on top of them via perturbation theory. In this approach the bubble can be calculated using different methods, such as finite differences and implementations of the $2n + 1$ theorem. At this point we recall the contribution of each phonon diagram to the linewidth and lineshift. The tadpole accounts for relaxation of internal structural parameters.

Perturbation theory	Equation
Linewidth	$\Gamma_{\mu}^{ph-ph}(\mathbf{q}) = -\text{Im}\Pi_{\mu}^B(\mathbf{q}, \omega_{\mu}(\mathbf{q}))$
Lineshift	$\Delta_{\mu}(\mathbf{q}) = \text{Re}[\Pi_{\mu}^L(\mathbf{q}, \omega_{\mu}(\mathbf{q})) + \Pi_{\mu}^B(\mathbf{q}, \omega_{\mu}(\mathbf{q}))]$

The next case is to use only the SSCHA. In this scenario we can explore Eq.(3.14) for the cases in which $z = 0$, denoted as static, and for z being a generic complex number, in our case the phonon frequencies obtained via SSCHA. For the static case one can obtain the second derivatives of the free energy considering different anharmonic contributions as illustrated in table 3.5. For the different cases one can obtain the dynamical via Eq.(3.24).

Case ($z = 0$)	Eq.(3.18)
SSCHA	$\frac{\partial^2 F}{\partial \mathcal{R} \partial \mathcal{R}} = \Phi$
SSCHA + $\langle D3V \rangle$	$\frac{\partial^2 F}{\partial \mathcal{R} \partial \mathcal{R}} = \Phi + \overset{(3)}{\Phi} \Lambda(0) \overset{(3)}{\Phi}$
SSCHA + $\langle D3V \rangle + \langle D34 \rangle$	$\frac{\partial^2 F}{\partial \mathcal{R} \partial \mathcal{R}} = \Phi + \overset{(3)}{\Phi} \Lambda(0) \overset{(3)}{\Phi} + \overset{(3)}{\Phi} \Lambda \Theta \Lambda(0) \overset{(3)}{\Phi}$

For the dynamical case, an ansatz to consider a general z was proposed and explained with details by Bianco et al and briefly discussed in (3.4.4). Under this ansatz, the phonon self energies are given by Eq.(3.28). In our calculations, we approximate the SSCHA self-energy to the bubble self-energy. Up to this point we are considering an off-diagonal self energy. We can then neglect the mixing between different phonon modes and assume that $\mathbf{\Pi}(z)$ is diagonal. The different approaches to calculate the self-energies are shown on the table below.

Case ($z = \omega = \omega_{\mathbf{q}\mu}^{sscha}$)	self-energy
Off-diagonal	$\mathbf{\Pi}(z) \approx \mathbf{\Pi}^{(B)}(z) = \mathbf{M}^{-\frac{1}{2}} \mathbf{\Phi} \mathbf{\Lambda}(z) \mathbf{\Phi} \mathbf{M}^{-\frac{1}{2}}$
Diagonal	$\Pi_{\mu}(\mathbf{q}, \omega) = \sum_{\alpha s, \beta t} e_{\mu}^{\alpha s}(\mathbf{q}) \Pi_{\alpha s \beta t}(\mathbf{q}, \omega + i0^+) e_{\mu}^{\beta t}(\mathbf{q})$

Chapter 4

Magnitude of the anharmonic contribution

On chapter 3 we introduced the SSCHA method which allows the access the anharmonic free energy Hessian using a non-perturbative approach. As the development of the SSCHA method is quite recent, it needs to be tested and extensively applied to real materials. Thermoelectrics such as PbTe and SnTe are a perfect playground to validate the SSCHA due to the occurrence of anharmonicity in their phonon spectra and due to their simple crystal structure.

In this spirit, this chapter is devoted to apply the SSCHA in different scenarios, in order to validate our approach as well to investigate the magnitude of the anharmonic contribution to the phonon spectra and self-energies for our systems of interest. We start our discussion by exploring the harmonic phonons and its dependence on the cell volume, born-effective charges, and \mathbf{k} -point sampling. After, we evaluate the contribution of the different terms on the SSCHA free energy Hessian, Eq.(3.18). Then, the thermal expansion for PbTe was investigated. In addition, the dependence of the phonon spectra on the supercell size is analyzed using an auxiliary model potential. Then, we compare the results obtained via perturbation theory with SSCHA results using third-order force constants calculated via finite differences. Finally, the phonon spectral function, is calculated using third-order force constants obtained using both methods, finite differences as well the SSCHA.

4.1 Calculation details

In order to make our tests we perform DFT calculations using the QUANTUM-ESPRESSO package [80]. For both PbTe and SnTe the exchange-correlation interaction is treated with the Perdew-Burke-Ernzerhof (PBE) generalized gradient approximation [81]. To describe the interaction between electrons and ions, we use norm-conserving pseudopotentials [82] for PbTe, and PAW [83] pseudopotentials for SnTe. In both case the semi-core $4d$ states in valence are included for Te and Sn, and $5d$ for Pb. Electronic wave functions are expanded in a plane-wave basis with kinetic energy cutoffs of 65 Ry and 28 Ry for scalar relativistic pseudopotentials, for PbTe and SnTe respectively.

Integrations over the Brillouin zone (BZ) are performed using a uniform grid of $8 \times 8 \times 8$ \mathbf{k} -points for PbTe, and a denser grid of $12 \times 12 \times 12$ \mathbf{k} for SnTe. Particular care must be taken in converging SnTe with respect to \mathbf{k} -points as the depth of the potential well as a function of phonon displacements is strongly dependent on the sampling, see Fig.(4.4) and subsection 4.2.2. Previous calculations [20] carried out with smaller samplings are found to be underconverged. Born effective charges calculated via DFPT are included for PbTe calculations only. For both PbTe and SnTe we consider the high temperature rock-salt structure, and the PBE optimized lattice parameters of 6.55 Å and 6.42 Å respectively. The effect of the thermal expansion is discussed in section 4.3.2.

The Harmonic phonon frequencies are obtained within the DFPT [53] as implemented in QUANTUM-ESPRESSO. For the tests reported in this work, we make use of the $2 \times 2 \times 2$, and then, the $4 \times 4 \times 4$ \mathbf{q} -point grids for both systems. Fourier interpolation is used to obtain the phonon dispersion along high symmetry lines.

To calculate the anharmonic renormalized phonons we use the SSCHA [16, 17, 18]. The trial Hamiltoniana is minimized in a supercell. As mentioned on chapter 3, the minimization process requires the energies and forces acting on a supercell for a set of random configurations generated by the trial density matrix. Those elements have been calculated on $2 \times 2 \times 2$ and $4 \times 4 \times 4$ supercells using the same parameters for the harmonic DFPT calculations. The number of random configurations we use is of the order of one thousand which is sufficient to converge our calculations. For PbTe no interpolation is used since the $4 \times 4 \times 4$ supercell is converged and adequate to describe the experimental results. In addition, we compare the third order force constants obtained via the SSCHA with the ones calculated using

the finite difference method implemented on the ShengBTE package [73].

4.2 Harmonic phonon dispersion

4.2.1 Dependence on the volume

It is well known that in ferroelectrics and thermoelectrics the phonon spectra strongly depends on the volume used in the calculations. Hence, The choice of an appropriate lattice parameter is crucial for the analysis. In the literature, several papers debate the advantages and drawbacks of using the experimental lattice constant over the DFT optimized lattice parameter, and vice versa. For this reason, we carry out our independent analysis on the dependence of the harmonic phonon spectra on the lattice parameters. In Fig.(4.1) we show harmonic phonon dispersions calculated within DFPT for PbTe and SnTe using (i) the zero temperature PBE theoretical lattice parameter and (ii) the experimental ones $a_{\text{exp}} = 6.46\text{\AA}$ and 6.32\AA , respectively. In both cases the experimental parameter is smaller than the theoretical one, as if the systems were experiencing a finite pressure.

As expected, the results are strongly volume dependent. In the case of PbTe, the use of the experimental lattice parameter hardens all the phonons, but this hardening is particularly large for the transverse optical (TO) mode at zone center that is shifted from 3.17 meV to 6.19 meV. However in both cases, the harmonic phonon frequencies remain positive and no structural instability is detected in PbTe, in agreement with experiments. PbTe is usually referred as an incipient ferroelectric because of the softness of the TO phonon mode. It is important to underline that in the case of PbTe INS experiments find a clear LO/TO splitting. We thus included this effect in our harmonic calculation.

At ambient pressure SnTe undergoes a phase transition in the 0 – 100 K temperature range. At low temperature the crystal symmetry changes from cubic ($Fm\bar{3}m$) to rhombohedral ($R3m$). The distortion is a displacive phase transition involving a small dimerization in the unit cell. The distortion is compatible with a phonon instability at zone center. Real samples of SnTe are non stoichiometric and the ferroelectric transition temperature strongly depends on the number of holes present in the system. It is approximately 100 K for hole concentrations of the order of $1 \times 10^{20} \text{ cm}^{-3}$ and decreases to approximately 30 K for ten times larger hole concentrations. At these large doping no LO/TO splitting is expected, so we neglect it in our simulations.

The dependence of the harmonic calculation on volume is stronger in the

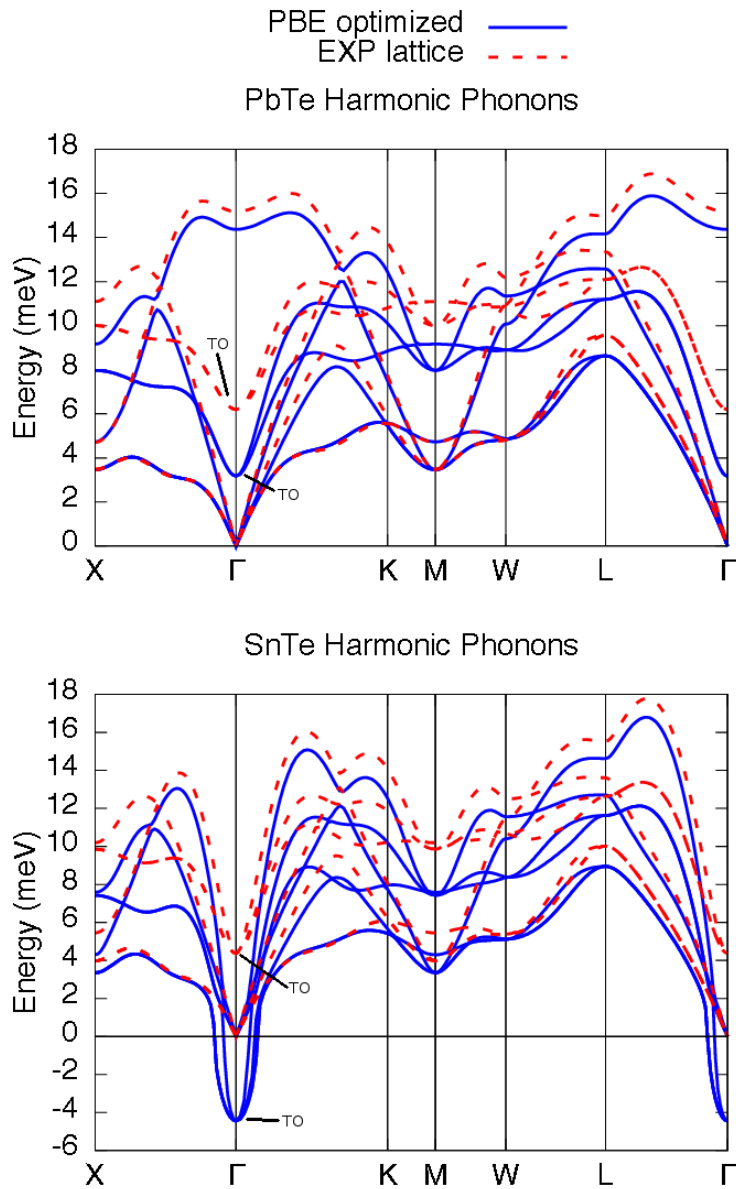


Figure 4.1: Harmonic phonons dispersion of PbTe and SnTe for different lattice constants. For the experimental lattice parameter (red lines) both systems do not present negative frequencies. For the PBE optimized lattice parameter (blue lines), the SnTe phonon spectra has negative frequencies on Γ , indicating a structural instability. The TO modes at Γ exhibit a strong dependence on the volume.

case of SnTe. The ferroelectric transition (imaginary TO phonon at zone center) is present when using the more expanded theoretical PBE volume while it disappears if the experimental volume is used. This again underlines the critical role of the volume and functional used in the calculation of phonon spectra in ferroelectrics and thermoelectrics.

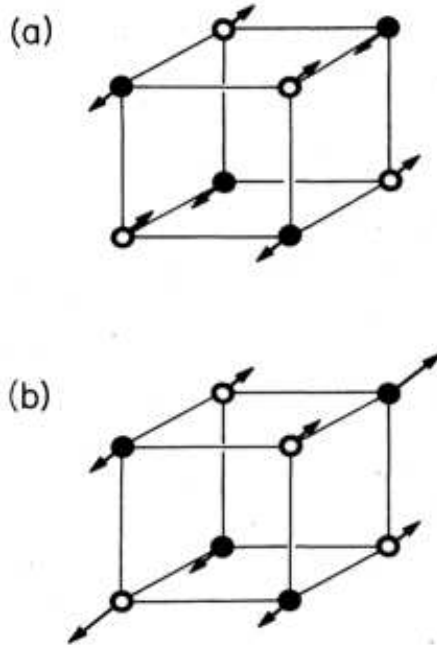


Figure 4.2: Low-temperature rhombohedral structure of SnTe can be obtained as a small distortion of the rock-salt structure by (a) displacing the two fcc sublattices relative to each other by $a_0\tau$ along the (111) direction, corresponding to a frozen-in $\mathbf{k}=0$ optic phonon, followed by (b) a rhombohedral shear in the (111) direction. To construct the phonon potential we considered step (a). Figure from ref.[31]

4.2.2 \mathbf{k} -points sampling in SnTe

An additional complications concerning the convergence of DFT calculations for SnTe is the \mathbf{k} -point sampling. Even if the difference on the total energy of the $Fm\bar{3}m$ structure between the $8 \times 8 \times 8$ and $20 \times 20 \times 20$ \mathbf{k} -point grids is of the order of 0.8 meV/atom, upon distortion towards the $R\bar{3}m$ structure illustrated in Fig.(4.2), the depth of the potential well differs of 1.55 meV/cell.

Thus, using a smaller \mathbf{k} -point grid, as done previous calculations, illustrated in Fig.(4.3), substantially overestimates the ferroelectric instability, as shown in Fig. 4.4. For this reason, we used a converged $12 \times 12 \times 12$ \mathbf{k} -point grid in our SnTe calculations.

4.2.3 Born effective charges and doping

The fact that both undoped PbTe and SnTe do not exist stoichiometric raises questions on how those systems should be simulated. For PbTe, since the typical doping is quite small and the LO-TO splitting is quite

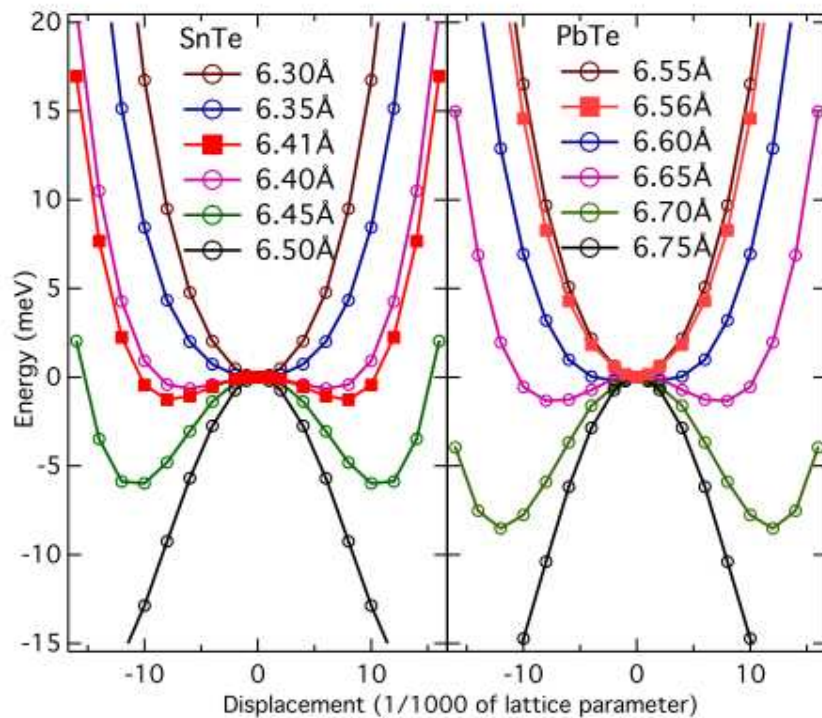


Figure 4.3: Double-well anharmonic phonon potential. Frozen phonon potentials of Γ -point TO phonon mode of SnTe and PbTe. Red solid boxes and lines correspond to relaxed lattice parameters at 0 K. The depth of the well in this case is close to 1 meV. Taken from the supplemental material of ref. [20]

pronounced, the inclusion of the Born effective charges is a natural choice. The effective charges for PbTe are calculated via DFPT and a posteriori added to the SSCHA dynamical matrices. On the other hand, on SnTe the effects of doping on the phonon dispersion are way more significant. Undoped SnTe should be ferroelectric, however its nature depends on the carriers concentration. Typically SnTe is heavily hole doped [28]. As hole concentration increases, the transition temperature decreases down to a point in which the system remains cubic, even at low temperatures, hence losing the ferroelectric phase. In order to tackle this problem, we compared the harmonic phonon dispersion for doped and undoped SnTe on a $4 \times 4 \times 4$ supercell. We have not included the Born effective charges as they would be screened by doping, and we used $n_h = 3.23 \times 10^{20} \text{ cm}^{-3}$ from ref [84] as the carrier concentration. Fig.(4.5) shows that the instability remains at this doping level, and the phonon dispersion along high symmetry directions are almost unaffected within the BZ.

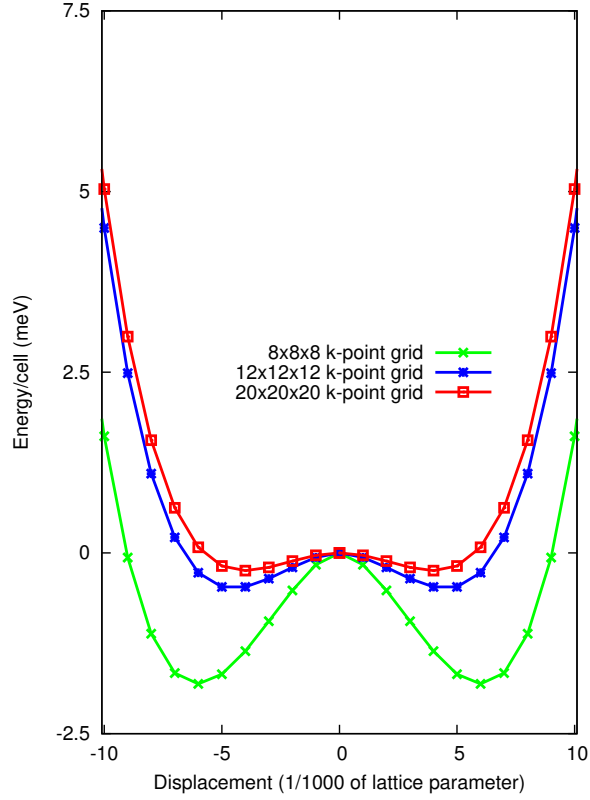


Figure 4.4: Frozen phonon potential for SnTe in function of the k-point grid.

4.3 Anharmonic contribution to the phonon dispersion: static limit ($z = 0$)

4.3.1 Magnitude of $\langle D3V \rangle$ and $\langle D4V \rangle$ terms

In order to evaluate the magnitude of anharmonic affects on the phonon spectra and the role of the different terms of Eq.(3.14), we will consider the static version of Eq.(3.18), namely ($z = 0$). One can rewrite it as:

$$\frac{\partial^2 F}{\partial \mathcal{R} \partial \mathcal{R}} = \Phi + \overset{(3)}{\Phi} \Lambda(0) \overset{(3)}{\Phi} + \overset{(3)}{\Phi} \Lambda(0) \Theta \Lambda(0) \overset{(3)}{\Phi} \quad (4.1)$$

As before, for simplicity we define:

$$\Theta = \left[\mathbb{1} - \overset{(4)}{\Phi} \Lambda(0) \right]^{-1} \overset{(4)}{\Phi}. \quad (4.2)$$

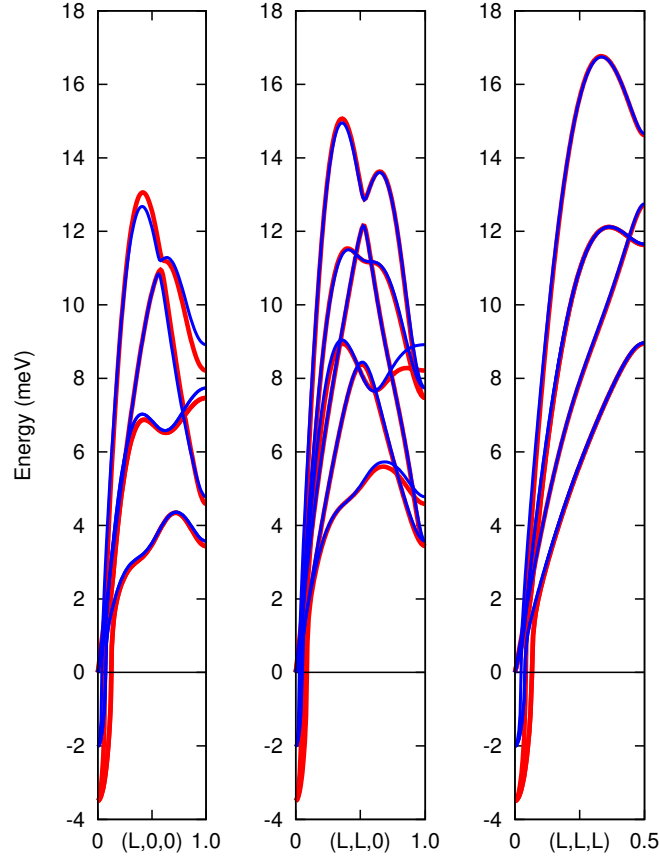


Figure 4.5: SnTe harmonic phonon dispersion using a $4 \times 4 \times 4$ supercell: undoped (red) and doped (blue) case. Besides points very close to the zone center, doping does not change considerably the dispersion curves.

and

$$\langle D3V \rangle = \overset{(3)}{\Phi} \Lambda(0) \overset{(3)}{\Phi} \quad (4.3)$$

$$\langle D4V \rangle = \overset{(3)}{\Phi} \Lambda(0) \Theta \Lambda(0) \overset{(3)}{\Phi} \quad (4.4)$$

To investigate the different terms in Eq.(3.18), and in particular the mutual role of $\langle D3V \rangle$ and $\langle D4V \rangle$ we perform SSCHA runs, on a $2 \times 2 \times 2$ supercell, for different temperatures; 300 and 600 K for PbTe, and 50 and 100 K for SnTe.

Fig.(4.6) and Fig.(4.7) compare the contribution of $\langle D3V \rangle$ and $\langle D4V \rangle$ to the phonon frequencies. Our calculations show that for PbTe the $\langle D4V \rangle$ term is negligible below 300 K while it is somewhat more relevant at 600 K. For SnTe in the temperature range studied in this work the $\langle D4V \rangle$ term is also negligible. As a consequence, in these temperature regions the

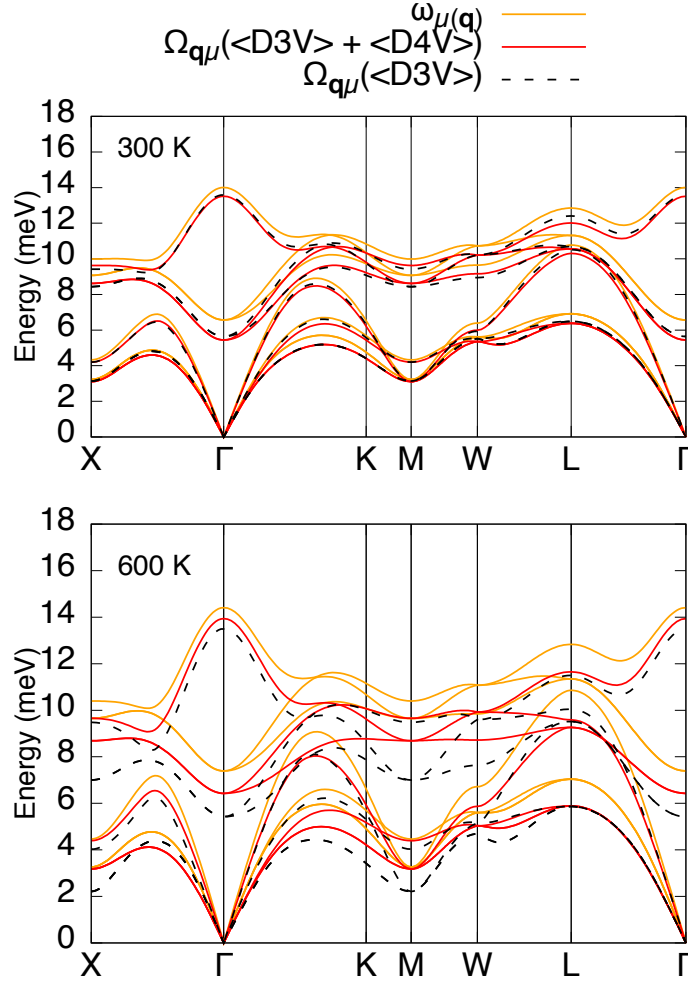


Figure 4.6: Anharmonic phonon dispersion curves for PbTe at 300 K and 600 K. Orange lines denote calculations neglecting the *bubble* and superior order terms, $(\omega_\mu(\mathbf{q}))$; black dashed lines represent the calculations including $\langle D3V \rangle$, while red lines includes the full expression, $\langle D3V \rangle + \langle D4V \rangle$, $(\Omega_{\mu\mathbf{q}})$. The phonon frequencies are obtained using Eq.(3.31) in the static limit, namely by using $\Pi_\mu(\mathbf{q}, 0)$.

Hessian of the free energy is entirely determined by the $\mathbf{D}^{(S)}$ matrix and the so-called "bubble" term $\langle D3V \rangle$.

This analysis justifies why we neglect the $\langle D4V \rangle$ term in the calculations for larger supercells. This test is important since the contribution related to $\langle D4V \rangle$ can be calculated only using smaller supercells, like the $2 \times 2 \times 2$. On the SSCHA recent implementation, the calculation of $\langle D4V \rangle$ is expensive and very memory consuming for larger supercells.

Having determined the smallness of $\langle D4V \rangle$ we proceed towards larger supercell calculations. By using an empirical potential fitted on the SSCHA configurations we check the convergence with respect to supercell

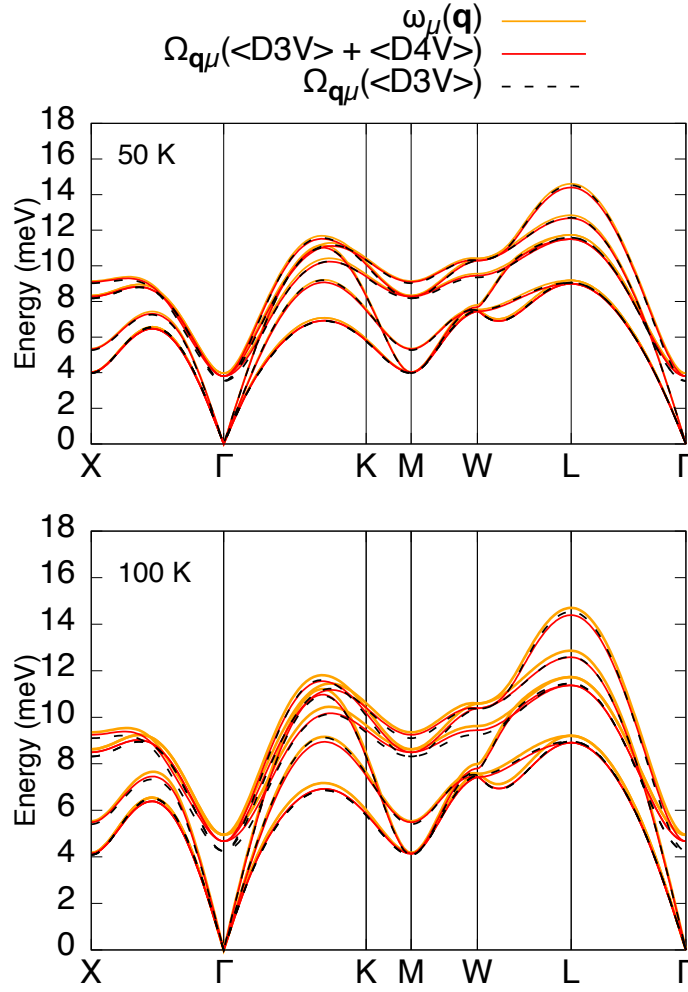


Figure 4.7: SSCHA runs for SnTe at 50 K and 100 K . Orange lines denote calculations neglecting the bubble and superior order terms, $(\omega_{\mu}(\mathbf{q}))$; black dashed lines represent the calculations including the bubble, $\langle D3V \rangle$; while red lines includes the full expression, $\langle D3V \rangle + \langle D4V \rangle$, $(\Omega_{\mu\mathbf{q}})$. The phonon frequencies are obtained using Eq.(3.31) in the static limit, namely by using $\Pi_{\mu}(\mathbf{q}, 0)$.

size. We found that the use of a $4 \times 4 \times 4$ supercell leads to converged phonon frequencies. So we use this supercell to carry out our first principles calculations. These test will be discussed deeply in section 4.3.3.

4.3.2 Evaluation of PbTe thermal expansion at 600K

To evaluate the effects of thermal expansion in our calculations for PbTe at 600 K , we perform several SSCHA runs for different volumes using a $2 \times 2 \times 2$ supercell. We add the vibrational free energy to the BO total energy to construct an energy vs lattice parameter curve, illustrated in Fig(4.8). By

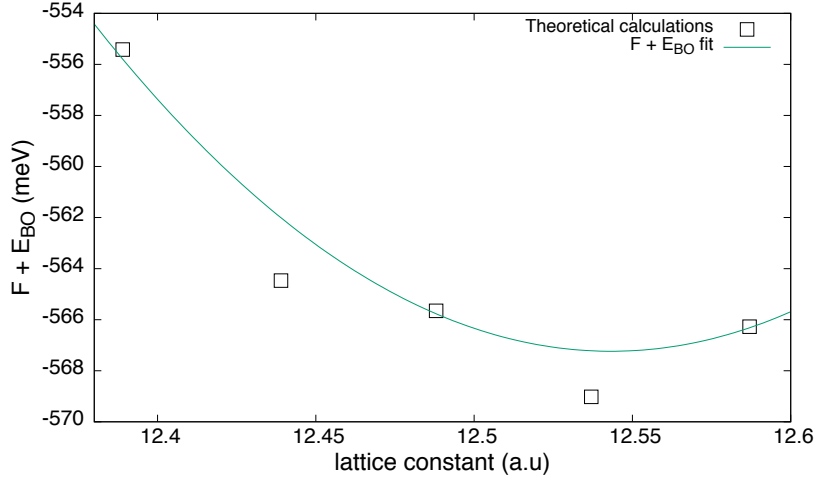


Figure 4.8: vibrational free energy plus the BO total energy vs lattice parameter.

finding the minimum of this curve we obtain a lattice parameter of 6.642 Å for PbTe at 600 K using the PBE functional in our calculations.

With this new lattice constant, we then compute the anharmonic phonon dispersion as before. Fig.(4.9) shows the phonon spectra for the two lattice parameters (PBE $T = 0 K$ and $T = 600 K$) considering just $\langle D3V \rangle$ and the case $\langle D3V \rangle + \langle D4V \rangle$. The phonon frequencies shift towards smaller values in relation to the PBE at 0 K as illustrated in Fig.(4.7). The shift is not significant for the $\langle D3V \rangle + \langle D4V \rangle$ case, whereas for the other case it is bigger.

4.3.3 Empirical potential calculations

In order to investigate supercell size effects on the phonons modes, specially at the zone center, in addition to the full ab-initio calculations contained in this thesis, we made use of a model potential based on the formulation developed by Marianetti et al [85, 86]. This potential was developed to study mainly rock-salt compounds and is well tested on lead telluride. The potential has the following form:

$$V(\mathbf{R}) = \frac{1}{2} \sum_{ab} \phi_{ab} u^a u^b + V_A^{(3)}(\mathbf{u}) + V_A^{(4)}(\mathbf{u}), \quad (4.5)$$

where $\mathbf{u} = \mathbf{R} - \mathbf{R}_{(0)}$, $\mathbf{R}_{(0)}$ corresponding to the equilibrium configuration on the rock-salt structure. The harmonic matrices ϕ_{ab} were calculated using the same parameters as for the DFPT calculations described on the main text. Anharmonic terms $V_A^{(3)}$ and $V_A^{(4)}$ are defined as:

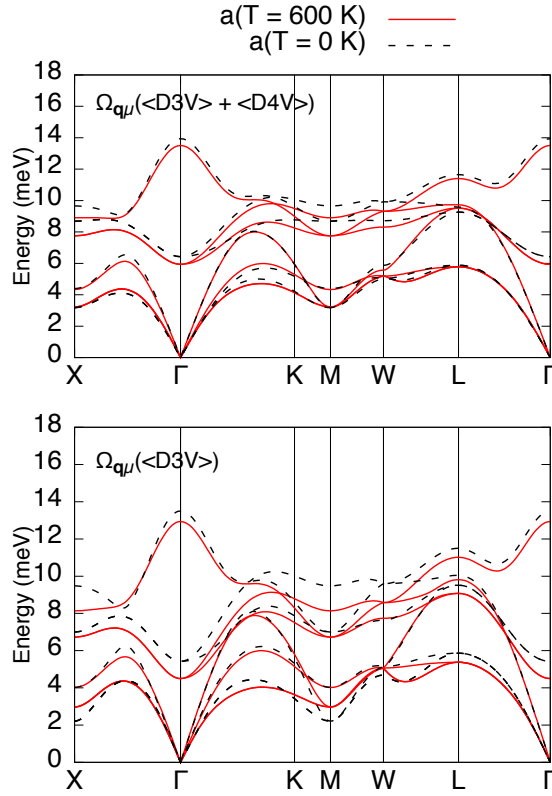


Figure 4.9: Anharmonic phonon spectra for the PBE at 600 K lattice parameter versus the PBE at 0 K case. It is noticeable that the difference is larger by including only $\langle D3V \rangle$. The phonon frequencies ($\Omega_{\mathbf{q}\mu}$) are obtained using Eq.(3.31) in the static limit, namely by using $\Pi_{\mu}(\mathbf{q}, 0)$.

$$V_A^{(3)}(\mathbf{u}) = p_3 \sum_{s=1}^{N_a} \sum_{\alpha=x,y,z} \left[\mathcal{A}_{s,\alpha+}^3 - \mathcal{A}_{s,\alpha-}^3 \right] \quad (4.6)$$

and

$$\begin{aligned} V_A^{(4)}(\mathbf{u}) = & p_4 \sum_{s=1}^{N_a} \sum_{\alpha=x,y,z} \left[\mathcal{A}_{s,\alpha+}^4 + \mathcal{A}_{s,\alpha-}^4 \right] \\ & + p_{4x} \sum_{s=1}^{N_a} \sum_{\alpha=x,y,z} \left[\mathcal{A}_{s,\alpha+}^2 \left((\mathcal{E}_{s,\alpha+}^{(1)})^2 + (\mathcal{E}_{s,\alpha+}^{(2)})^2 \right) \right. \\ & \left. + \mathcal{A}_{s,\alpha-}^2 \left((\mathcal{E}_{s,\alpha-}^{(1)})^2 + (\mathcal{E}_{s,\alpha-}^{(2)})^2 \right) \right] \end{aligned} \quad (4.7)$$

where, for example

$$\begin{aligned}
\mathcal{A}_{s,x_{\pm}} &= \frac{1}{\sqrt{2}} \left(u^{x_{\pm}(s),x} - u^{s,x} \right) \\
\mathcal{E}_{s,x_{\pm}}^{(1)} &= \frac{1}{\sqrt{2}} \left(u^{x_{\pm}(s),y} - u^{s,y} \right) \\
\mathcal{E}_{s,x_{\pm}}^{(2)} &= \frac{1}{\sqrt{2}} \left(u^{x_{\pm}(s),z} - u^{s,z} \right).
\end{aligned} \tag{4.8}$$

The variables $x_+(s)$ and $x_-(s)$ represent the nearest-neighbour of atom s , along the cartesian direction $+x$ and $-x$, respectively. For the other cartesian directions, $\pm y$ and $\pm z$, we generalized this notation. The quantity u is the displacement from the equilibrium position.

The potentials for both systems were defined by fitting the parameters p_3 , p_4 , and p_{4x} to ab-initio forces calculated for one thousand random atomic configurations generated in the first principles SSCHA calculation. For PbTe we used a combination of configurations generated at 300 K and 600 K, resulting on the coefficients $p_3 = 2.99 \text{ eV}/(\text{\AA})^3$, $p_4 = 4.17 \text{ eV}/(\text{\AA})^4$, and $p_{4x} = -1.32 \text{ eV}/(\text{\AA})^4$. For SnTe we used configurations generated at 100 K obtaining $p_3 = 2.51 \text{ eV}/(\text{\AA})^3$ and $p_4 = 6.18 \text{ eV}/(\text{\AA})^4$, in this case p_{4x} was neglected since its contribution was not relevant.

Fig.(4.10) and Fig.(4.11) compare the phonon dispersion on a $4 \times 4 \times 4$ supercell calculated ab-initio and using the empirical potential for PbTe (300 K) and SnTe (100 K), respectively. For PbTe the larger difference is at zone center, this may be due to the fact that we used random configurations generated on a broader range of temperatures. However, this is not a problem in order to study the convergence of the TO modes using the empirical potential for different supercell sizes. For SnTe, since we generated our random configurations at 100 K, one may expect a better agreement.

Fig.(4.14) presents the convergence tests regarding the TO modes of PbTe and SnTe. For the first compound, the difference between the $2 \times 2 \times 2$ and $4 \times 4 \times 4$ is small for the points which are included exactly by using the $2 \times 2 \times 2$ supercell (X, Γ, L), as shown in Fig.(4.12). However, as stated before, we used the $4 \times 4 \times 4$ supercell in order to include more points along on the BZ and, as a consequence, to describe more accurately the phonon dispersion of PbTe.

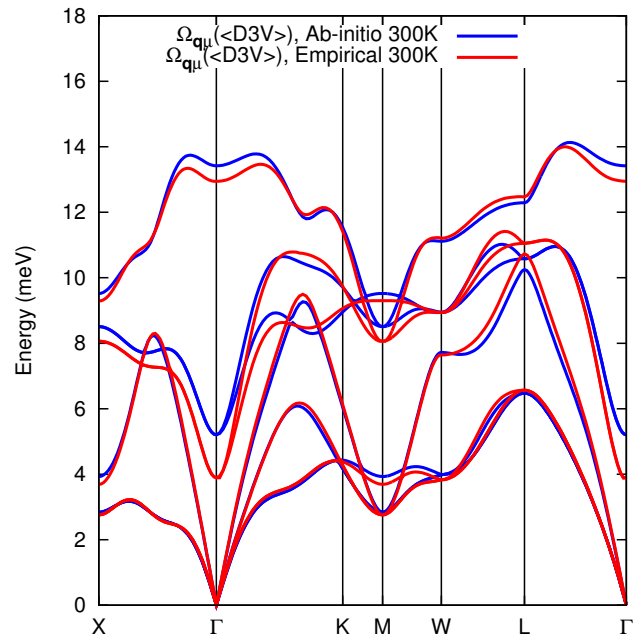


Figure 4.10: Anharmonic PbTe phonon dispersion at 300 K on a $4 \times 4 \times 4$ supercell: Ab-initio vs (blue lines) empirical potential (red lines).

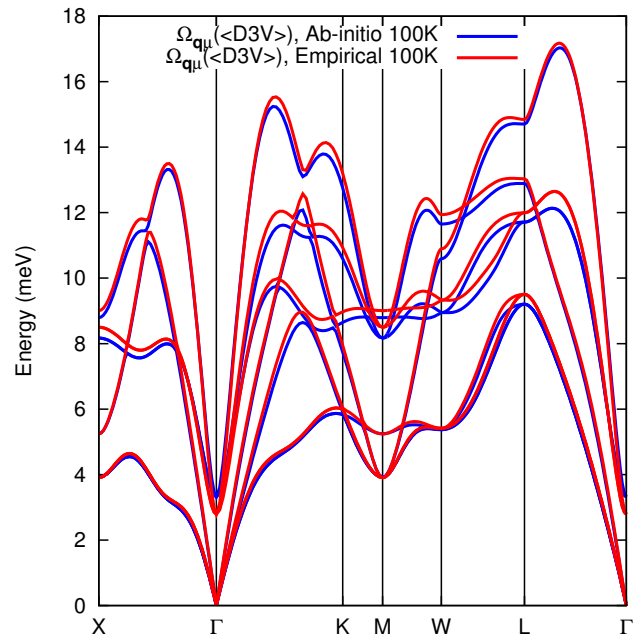


Figure 4.11: Anharmonic SnTe phonon dispersion at 100 K on a $4 \times 4 \times 4$ supercell: Ab-initio vs (blue lines) empirical potential (red lines). The phonon frequencies ($\Omega_{\mu\mathbf{q}}$) are obtained using Eq.(3.31) in the static limit, namely by using $\Pi_{\mu}(\mathbf{q}, 0)$.

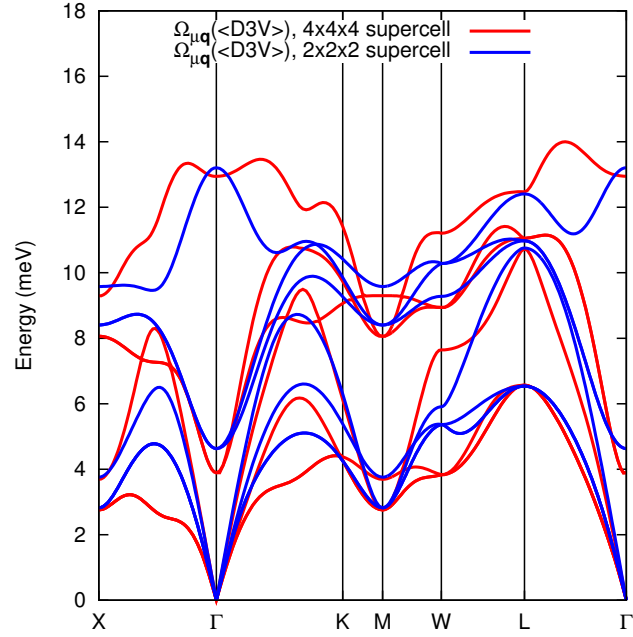


Figure 4.12: Comparison between PbTe anharmonic phonon spectra using a $2 \times 2 \times 2$ (blue) and $4 \times 4 \times 4$ (red) supercell. Both dispersions were calculated using an empirical potential and including the bubble term. The phonon frequencies ($\Omega_{\mu q}$) are obtained using Eq.(3.31) in the static limit, namely by using $\Pi_{\mu}(\mathbf{q}, 0)$.

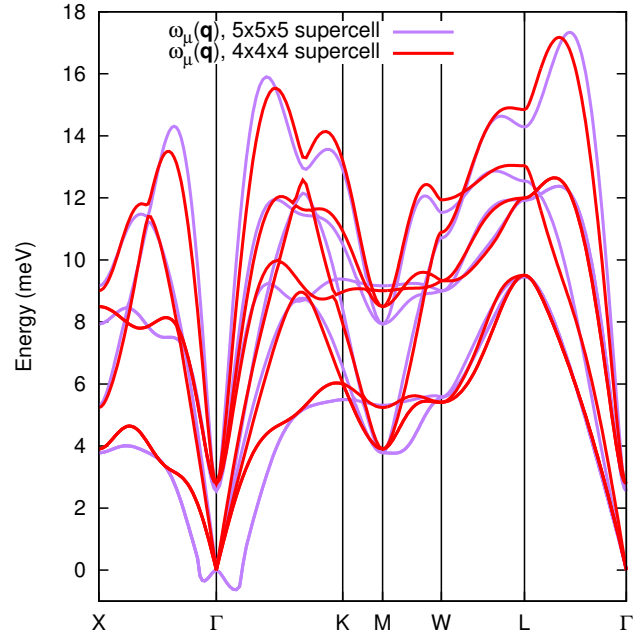


Figure 4.13: Comparison between SnTe anharmonic phonon spectra using a $4 \times 4 \times 4$ (red) and $5 \times 5 \times 5$ (purple) supercell. In this case the *bubble* and higher order terms are neglected on our calculations. The phonon frequencies ($\omega_{\mu}(\mathbf{q})$) are obtained using Eq.(3.31).

As mentioned before, for SnTe we considered at least a $4 \times 4 \times 4$ supercell in our ab-initio calculations, since the $2 \times 2 \times 2$ does not seem to be sufficient. In order to test the convergence we explored the model potential on the $4 \times 4 \times 4$ and also on the $5 \times 5 \times 5$ supercells. In this case, we compared just the SSCHA runs without including extra terms due to the computationally costly evaluation of third-order force constants for larger supercells. Fig.(4.13) shows the phonon dispersion for the $4 \times 4 \times 4$ and $5 \times 5 \times 5$ supercell. It is necessary to emphasize that the latter presents some wiggles due to the Fourier transform, so the negative energies are not physical, just an interpolation artifact.

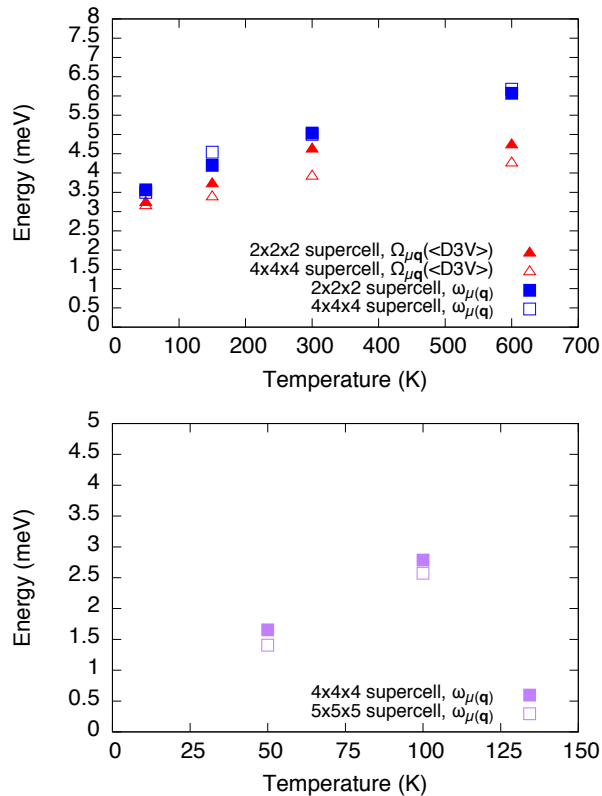


Figure 4.14: On the TO modes in function of T for PbTe (top) and SnTe (bottom) for different supercell sizes. The *bubble* contribution was taken on for supercells up to the $4 \times 4 \times 4$. The phonon frequencies ($\Omega_{\mu\mathbf{q}}$) are obtained using Eq.(3.31) in the static limit, namely by using $\Pi_{\mu}(\mathbf{q}, 0)$.

As can be viewed in Fig.(4.14), the difference between the TO modes using different supercells is not significant for our purposes.

4.4 Anharmonic contribution to the phonon dispersion: Dynamical self-energy calculations, $(z = \omega = \omega_{\mathbf{q}\mu}^{sscha})$

In this section we consider the dynamic case, denoted $(z = \omega = \omega_{\mathbf{q}\mu}^{sscha})$, to make some relevant tests. First, we explore the differences between considering the diagonal and off-diagonal self energies. To do it, we compare the spectral weight for the Γ point in the BZ, we plot the phonons frequencies obtained by the first case on top of the spectral function found by the latter, and we contrast the spectral function obtained by both. Finally, we investigate the nature of the third-order force constants given by the SSCHA. In the following tests, full ab-initio calculations were used and $4 \times 4 \times 4$ supercells considered.

4.4.1 Diagonal vs off-diagonal self-energies

As stated on chapter 3 the phonon self-energies can be evaluated using perturbative and non-perturbative approaches. In this section we compare the results obtained considering the diagonal self-energy and the off diagonal self energy. In the spirit of our analysis in section 4.3 we will neglect terms beyond the bubble in our calculations, since they do not have a substantial contribution to the self-energy. In this approximation we then, consider the diagonal self energy given by

$$\Pi_{\mu}(\mathbf{q}, \omega) = \sum_{\alpha s, \beta t} e_{\mu}^{\alpha s}(\mathbf{q}) \Pi_{\alpha s \beta t}(\mathbf{q}, \omega + i0^{+}) e_{\mu}^{\beta t}(\mathbf{q}). \quad (4.9)$$

The phonon frequencies squared, $\Omega_{\mathbf{q}\mu}^2$, corrected by the *bubble* self-energy are than obtained as

$$\Omega_{\mathbf{q}\mu}^2 = \omega_{\mu}^2(\mathbf{q}) + \text{Re}\Pi_{\mu}(\mathbf{q}, \omega_{\mathbf{q}\mu}). \quad (4.10)$$

On this limit one may recover the perturbation theory results. This fact is well demonstrated on the paper of Bianco et al.

For the off-diagonal self-energy we work on the case when

$$\Pi(z) \approx \Pi^{(B)}(z) = \mathbf{M}^{-\frac{1}{2}} \mathbf{\Phi} \mathbf{\Lambda}(z) \mathbf{\Phi} \mathbf{M}^{-\frac{1}{2}}. \quad (4.11)$$

We then calculate the spectral weight, spectral function, and the phonon modes for the diagonal case.

Regardless the nature of the method, one must have the knowledge of high-order force constants to do it. For example, within perturbation theory, the calculation of the bubble term given by Eq.(3.3) relies on the knowledge of the third-order force constants, which are the third derivatives of the potential

$$\phi_{s_1 s_2 s_3}^{\alpha_1 \alpha_2 \alpha_3}(\mathbf{R}_1, \mathbf{R}_2, \mathbf{R}_3) = \left[\frac{\partial^3 U(\mathbf{R})}{\partial u_{s_1}^{\alpha_1}(\mathbf{R}_1) \partial u_{s_2}^{\alpha_2}(\mathbf{R}_2) \partial u_{s_3}^{\alpha_3}(\mathbf{R}_3)} \right]_0. \quad (4.12)$$

In order to calculate this object we make use of the finite difference method implemented on the code `thirdorder.py` part of the ShengBTE package [73]. First, the code generates a minimal set of displaced supercell configurations, then we use DFT calculations to obtain the forces for these configurations, and finally the code use the results to construct the whole anharmonic force constants set. For the sake of consistency, our tests are carried out using the regular third-order force constants instead of the SS-CHA third-order force constants $\overset{(3)}{\Phi}$. The comparison between the first and the latter will be addressed in the following section.

We start by comparing the anharmonic phonon dispersion and the spectral function obtained by using the diagonal and off-diagonal self-energies, respectively. For PbTe, Fig.(4.15) shows the anharmonic phonon dispersion at 300 and 600 K on top of the spectral function calculated using the off-diagonal case.

It is noticeable that the phonon dispersion coincide with the most intense branches on the spectral function. Hence, for this system, this test shows there are not significant differences between the diagonal and off-diagonal self energies. Another remarkable feature, is the presence of the satellite peak at Γ . This peak is more intense at 300 K and becomes more diffuse for the other case. Past TDEP calculations carried by Romero et al [64]. found a similar behaviour for this satellite. We will discuss more on this matter on the following chapter, when the experimental results will be mentioned.

Fig.(4.16) shows the anharmonic phonon spectra along special points on the BZ for SnTe at 50 and 100 K. Also for this system the differences between using the diagonal and off-diagonal self-energies are minimal. Hence, there is no a significant difference between the position of the phonon modes

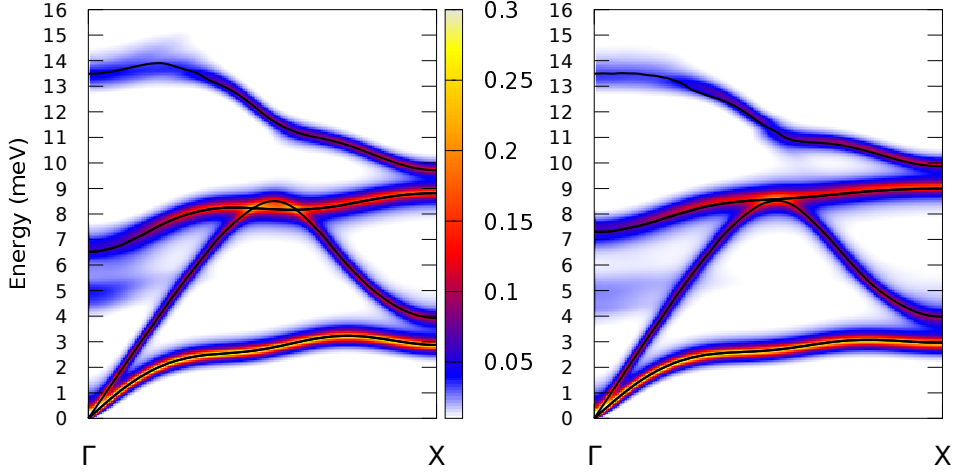


Figure 4.15: Anharmonic phonon spectra of PbTe at 300 K (left) and 600 K (right) calculated via perturbation theory, diagonal case (solid lines), on top of the spectral function calculated considering off-diagonal self-energies (heat map). The presence of a satellite peak is verified at $\mathbf{q}=\Gamma$. The third-order forces constants were calculated using the finite differences method.

and the branches on the spectral function.

Another way to compare both approaches is to analyse the spectral weight curve obtained by considering only one point on the BZ. In this tests we considered the Γ point, since it is where the most interesting physics happens in these compounds. For both systems, the peaks related to the TO modes, displayed on Fig.(4.17) and Fig(4.18), softens at low temperatures. For the case of PbTe, by raising the temperature, the intensity of the satellite peak decreases, and it becomes broader. SnTe exhibits a single peak as expected, since no additional feature is reported in literature.

4.4.2 Third order force constants

The implementation of the SSCHA allows one to calculate the SSCHA third order force constants

$$\Phi_{a_1 a_2 a_3}^{(3)}(\mathcal{R}) = \left\langle \frac{\partial^3 U}{\partial R^{a_1} \partial R^{a_2} \partial R^{a_3}} \right\rangle_{\rho_{\mathcal{H}}} \quad (4.13)$$

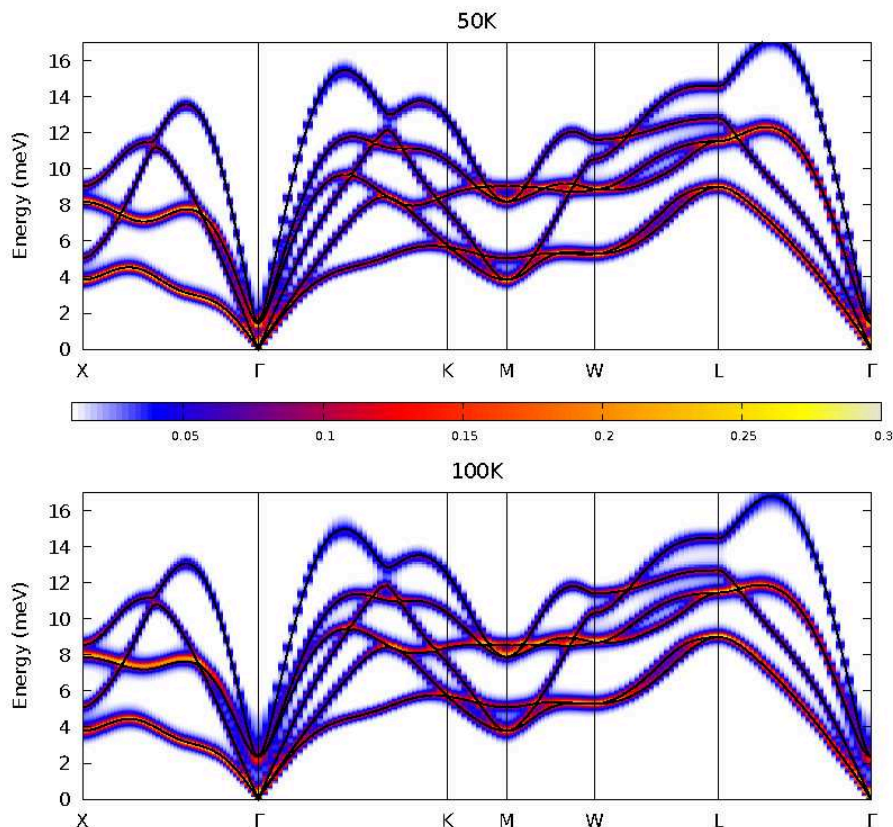


Figure 4.16: Anharmonic phonon spectra of SnTe at 50 K (top) and 100 K (bottom) calculated via perturbation theory, diagonal case (solid lines) on top of the spectral function (heat map) calculated considering off-diagonal self-energies. A good agreement between the phonon frequencies and the spectral function is obtained. Differently to PbTe, we do not verify the existence of satellites. As before, the third-order forces constants were calculated using the finite differences method.

using an stochastic procedure. Here, we recall that during the developments concerning the SSCHA we defined the composite index $a = (\alpha, s, \mathbf{l})$, which indicates cartesian index, atom index and lattice vector together. However, since these force constants are obtained stochastically, their "quality" depends on the number of configurations used. On the ideal case for an infinite number of configurations, they should be equivalent to the regular force constants. In order to clarify this matter, we used the off-diagonal self-energies to compare the spectral function obtained using the SSCHA third-order force constants and the ones used in the previous subsection. In our tests we made use of one thousand configurations to ensure the convergence of the SSCHA runs.

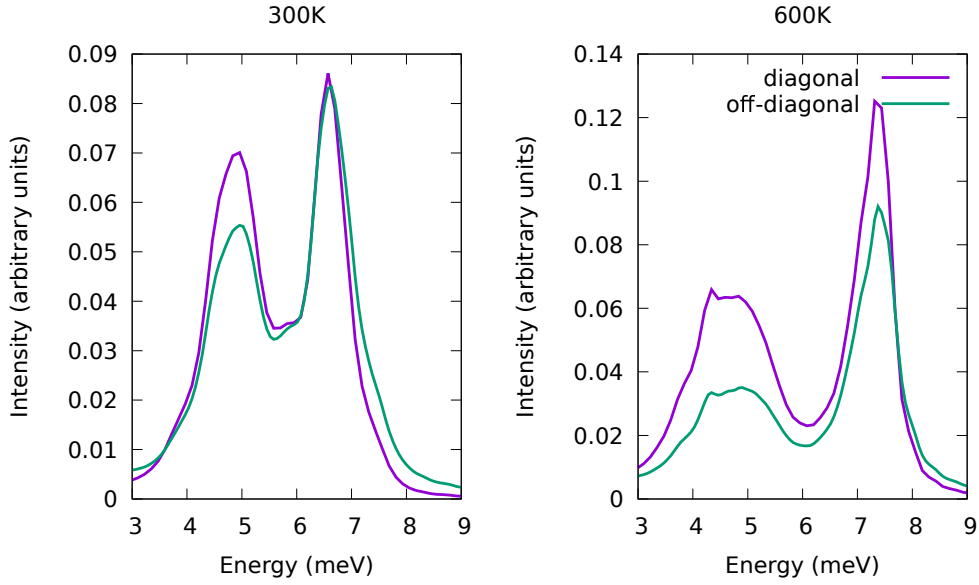


Figure 4.17: Spectral weight of PbTe at 300K (right) and 600 K (left), for $\mathbf{q}=\Gamma$. The position of the peaks as well the shape of the curves demonstrate that there is no significant difference in considering the diagonal and off-diagonal case.

Fig.(4.19) and Fig.(4.20) displays the calculations for PbTe at 300 K, they correspond to the spectral function along the Γ -X directions along the BZ, and a slice for the zone center, respectively. It is noticeable that the two plots on Fig.(4.19) are very similar, and the shift of the peak positions on Fig.(4.20) are small.

We have a similar behaviour for the calculations at 600 K shown in Fig.(4.21) and Fig.(4.22). In this case the most noticeable difference is that the satellite is broader for the case in which we use the SSCHA third-order force constants.

For SnTe we repeated the same tests for 50 and 100 K. Fig.(4.23) to Fig.(4.26) show the comparison between the spectral functions obtained using the two types of force constants, and the spectral weight on Γ . By looking to these pictures we can state that for this range of temperatures, the calculations using SSCHA third-order force constants or regular third-order force constants is equivalent. The validity of this statement has to be investigated for each case. However, we believe that the use of a sufficient large number of random configurations on the SSCHA allow a good description of effects related to the third-order contribution to the anharmonic potential.

We can conclude then that the stochastic force constants are suitable

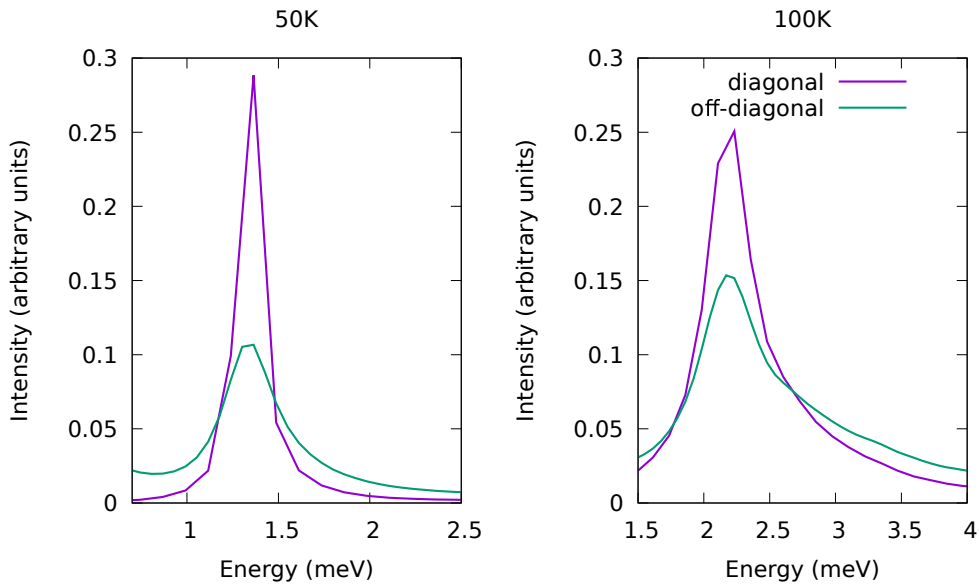


Figure 4.18: Spectral weight of SnTe at 50K (right) and 100 K (left), for $\mathbf{q}=\Gamma$.

to carry out the evaluation of anharmonic properties, since they give very similar results in comparison with the ones obtained via third-order force constants calculated using finite differences. In addition, this result demonstrates the power of the SSCHA, since it is able to evaluate on the same run anharmonic contributions of different orders. Thus, not requiring any additional external calculations.

4.5 Summary

In this chapter some tests were carried out in order to explore the validity and some limits of the SSCHA. It is important to stress that these tests are very important since the new developments on the SSCHA are quite recent. We started our analysis by exploring the harmonic theory. We observed that the choice of the lattice parameter considerably affects the phonon spectra of PbTe and SnTe. In addition, specially for SnTe, the TO modes at zone center may even be imaginary depending on this choice. After, we commented on the k-point sampling for SnTe which has shown to be a delicate issue, requiring a larger grid.

We used the SSCHA on the static, ($z = 0$), limit to verify that for our systems of interest, the most relevant terms on the anharmonic potential comes mainly from contributions up to the third-order. This allowed us to

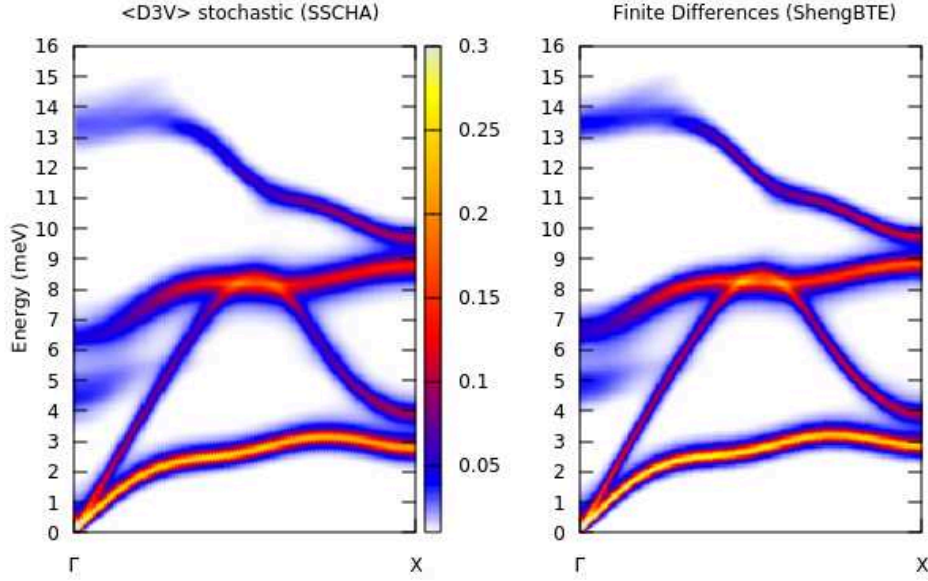


Figure 4.19: Spectral function of PbTe at 300K. The third-order forces constants were calculated via the SSCHA (left) and by the finite difference method (right).

compare directly SSCHA calculations with perturbation theory findings, since by using the latter one can include the bubble term. Furthermore, PbTe thermal expansion and dependence on the supercell size were tackled under this limit.

We explored also the dynamic case, ($z = \omega = \omega_{\mathbf{q}\mu}^{sscha}$), and investigated the differences between the diagonal and off-diagonal self-energies. For PbTe and SnTe, the differences are not significant, however this may not be the case for systems in which terms beyond the bubble are relevant. Finally the impact on the numerical calculations using SSCHA third-order forces constants was studied. We noticed that for a sufficient number of random configurations on the SSCHA runs, the SSCHA force constants should be equivalent, or at least very similar, to the force-constants obtained by third derivatives of the ionic potential.

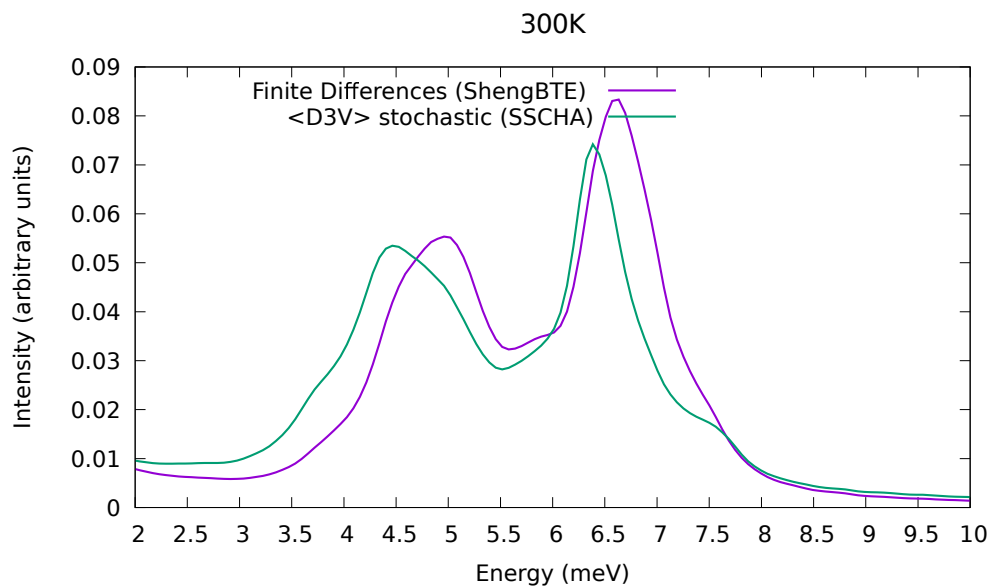


Figure 4.20: Spectral weight of PbTe at 300K (right) and 600 K (left), for $\mathbf{q}=\Gamma$. The position of the peaks is very similar, the different

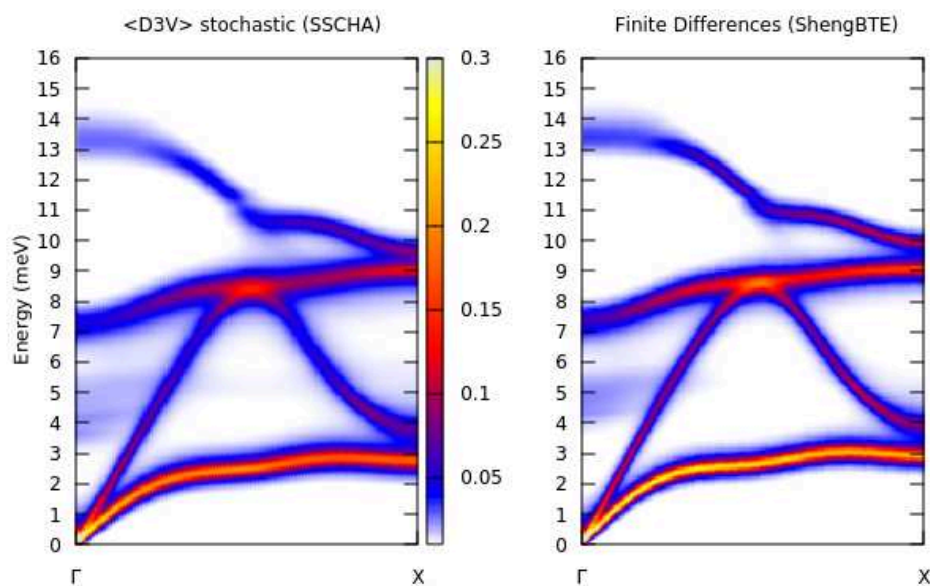


Figure 4.21: Spectral function of PbTe at 600K. The third-order forces constants were calculated via the SSCHA (left) and by the finite difference method (right). In this case, the low energy region at Γ exhibits a more diffusive behaviour for the SSCHA calculations.

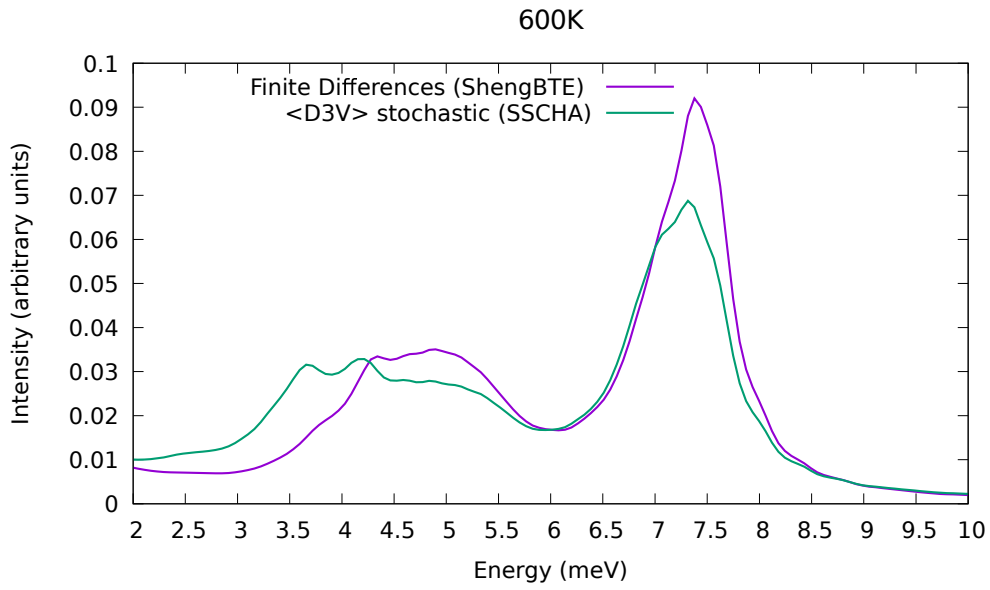


Figure 4.22: Spectral function of PbTe at 600K for $\mathbf{q} = \Gamma$. The third-order forces constants were calculated via the SSCHA (left) and by the finite difference method (right).

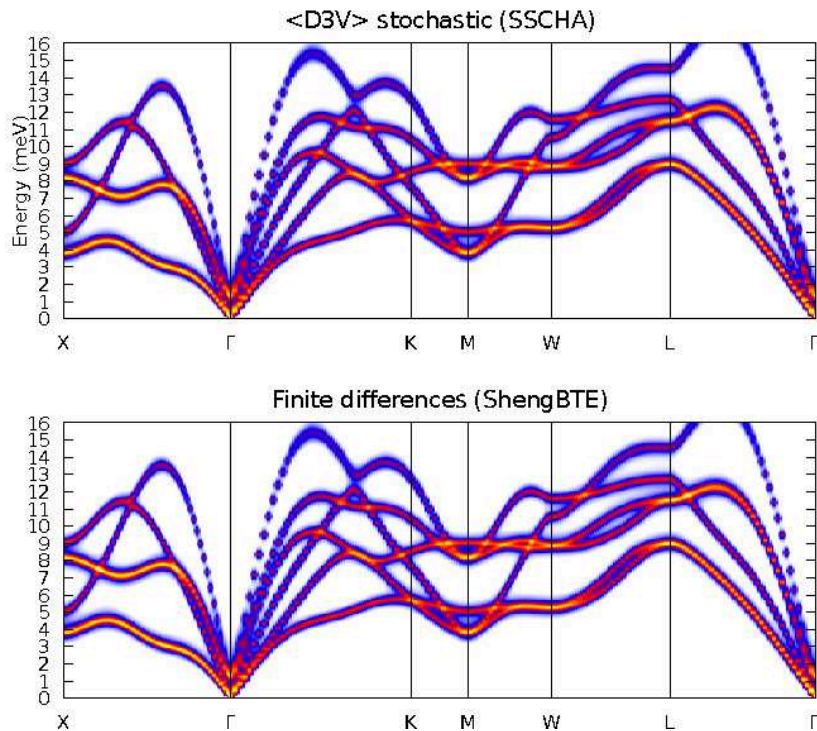


Figure 4.23: Spectral function of SnTe at 50K. The third-order forces constants were calculated via the SSCHA (top) and by the finite difference method (bottom). For SnTe we do not verify the presence of a satellite peak at Γ .

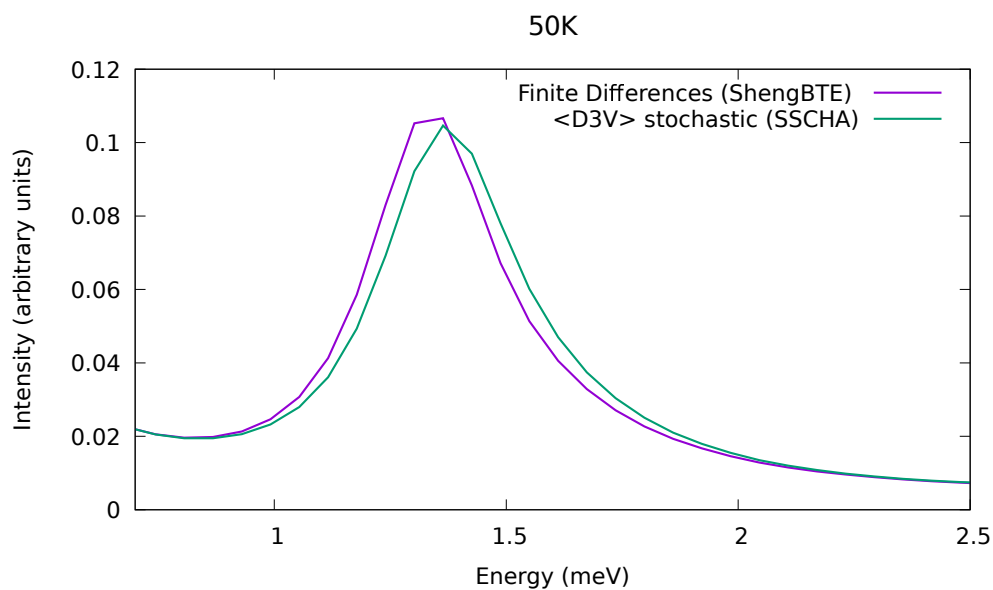


Figure 4.24: Slice of the spectral function of SnTe at 50 K, $\mathbf{q} = \Gamma$. The third-order force constants were calculated via the SSCHA and by the finite difference method.

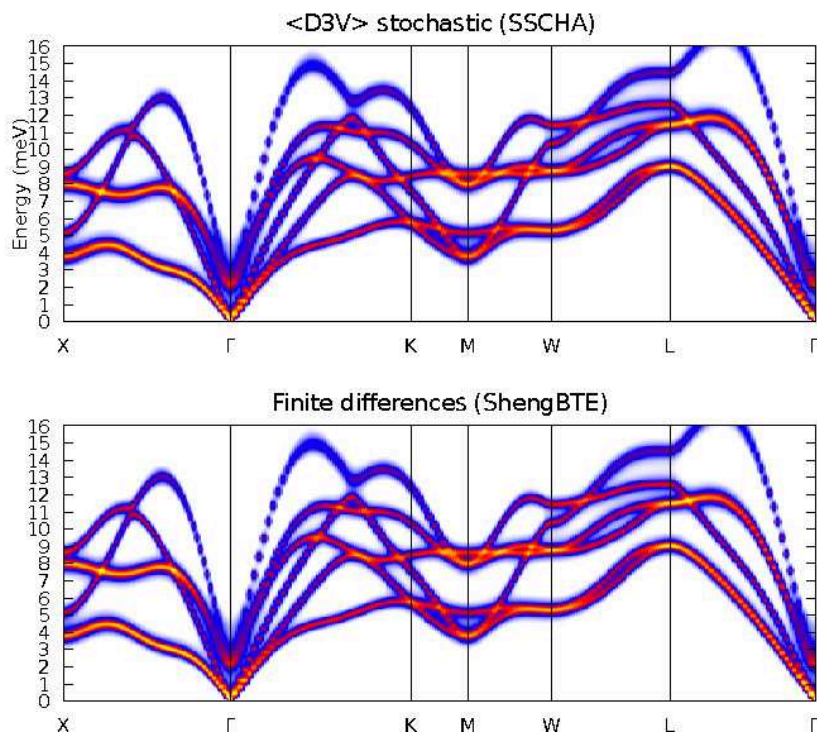


Figure 4.25: Spectral function of SnTe at 100 K along special point on the BZ. The third-order force constants were calculated via the SSCHA (top) and by the finite difference method (bottom).

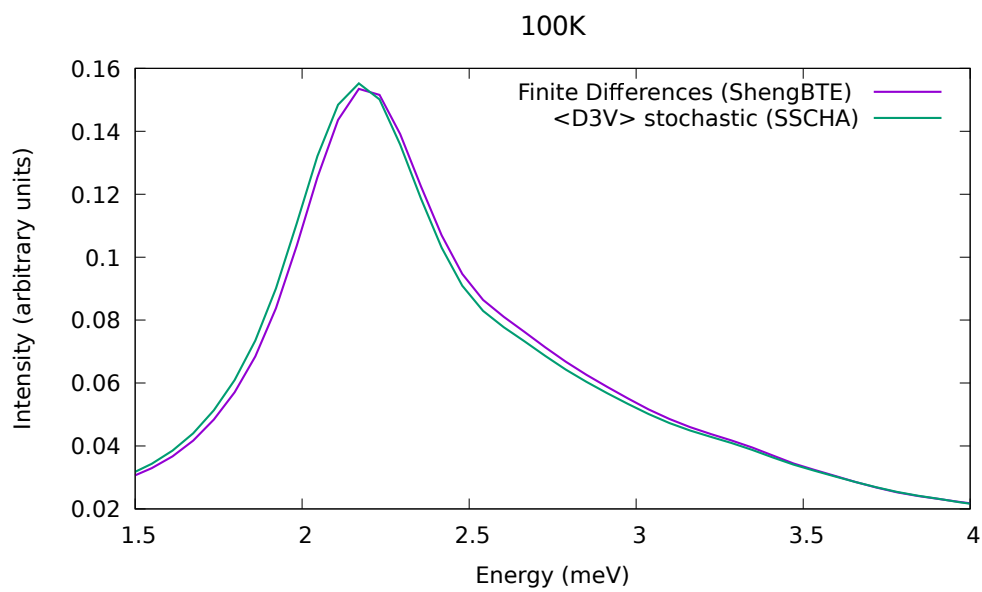


Figure 4.26: Slice of the spectral function of SnTe at 100 K, $\mathbf{q} = \Gamma$. The third-order force constants were calculated via the SSCHA and by the finite difference method. The agreement between the curves is evident.

Chapter 5

Lattice-dynamics of PbTe and SnTe

On chapter (4) we tested the validity and different limits of the SSCHA method. With this tests in hand, we established a consistent approach to carry on our final calculations.

The objective of this chapter is to apply our converged approach to PbTe and SnTe, and compare our findings using the SSCHA to experimental data and other articles in the literature. We start by commenting on the possible origins of the strong anharmonicity on PbTe. After, we compare our calculated anharmonic phonon frequencies obtained for different temperatures. Then, we compare experimental INS data with our calculations, exploring the anharmonic spectra as well our calculated spectral function. For the latter, we discuss the presence of an additional peak found at center of the BZ and how it is affected by temperature.

For SnTe, we carry out a similar analysis. However, in addition to the case of PbTe, for this system we estimate the transition temperature at which a displacive structural phase transition occurs. To do it, we calculate the square of the TO modes at zone center as a function of temperature, where the phonon instability is present.

5.1 Lead telluride (PbTe)

5.1.1 Anharmonic phonon dispersion

The anharmonic effects in PbTe have been extensively studied experimentally using techniques such as INS, and various theoretical models to explain features such as the dependence of the TO modes on temperature,

and why it is strong anharmonic. The mechanisms behind its anharmonicity are still debated in literature. One of the main explanations proposed by Li et al [20]. relies on a nesting between its longitudinal acoustic modes and transverse optical modes, denoted by the parallel sections on Fig.(5.1).

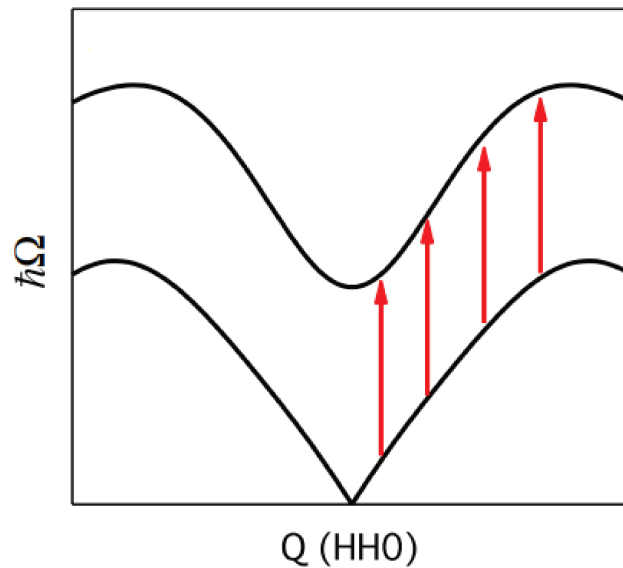


Figure 5.1: Schematic of nesting between acoustic and optical branches in phonon dispersions of PbTe from ref.[20].

This theory is linked to the analysis of the joint density of states (JDOS), which is proportional to the imaginary part of the phonon self energy when $\phi_{\mu\mu_1\mu_2}(-\mathbf{q}, \mathbf{q}, \mathbf{q}_2)$ is a constant. In Fig.(5.2) the sharp peak occurs around 4 meV for PbTe, while a broader peak is found at 3 meV for SnTe. Hence, the sharp peak and the joint DOS reflects the nesting in phonon dispersions of PbTe. The key difference between the two materials is that this peak is sharper in PbTe than in SnTe, because of better nesting of the acoustic and optic phonon bands in PbTe.

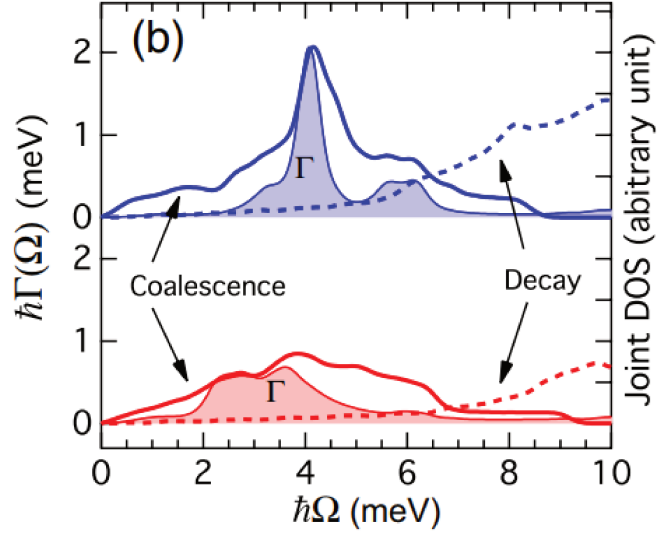


Figure 5.2: Joint density of states of PbTe and SnTe calculated by Li et al [20].

We start our analysis by comparing the anharmonic phonon dispersion curves calculated via Eq.(5.3) for PbTe at 300 K, 600 K, and the harmonic spectra. As stated on the previous chapter, the calculations include up to the bubble term in the phonon self-energy. By looking at the spectra, it is noticeable that the TO modes at zone center softens for lower temperatures. In addition, at the middle of the path Γ -K in the BZ, for energies around 8 meV, due to the shift of the TO modes an avoided crossing is expected for temperatures above 600 K. This avoided crossing is reported experimentally on the paper of Delaire et al [19]. In the same paper the authors infer that this avoided crossing may be one of the sources of the strong anharmonicity in PbTe, making a link with the analysis of the joint DOS.

In Fig.(A.2) we compare the PbTe phonon dispersion curves at 300 K obtained by the SSCHA to INS experimental data obtained by Cochran et al [15]. Our calculated curves are in good agreement with experimental results. We obtain a higher value than the experiments for the TO modes at zone center, this is consistent to newer observations of a double peak in this region [19]. Previous calculations[87] found a good agreement for the lower energy TO mode at Γ , however not obtaining a good description of the high energy phonon branches. More recent INS measurements[19] have suggested the presence of a strong temperature dependent phonon satellite close to Γ originated from the TO mode.

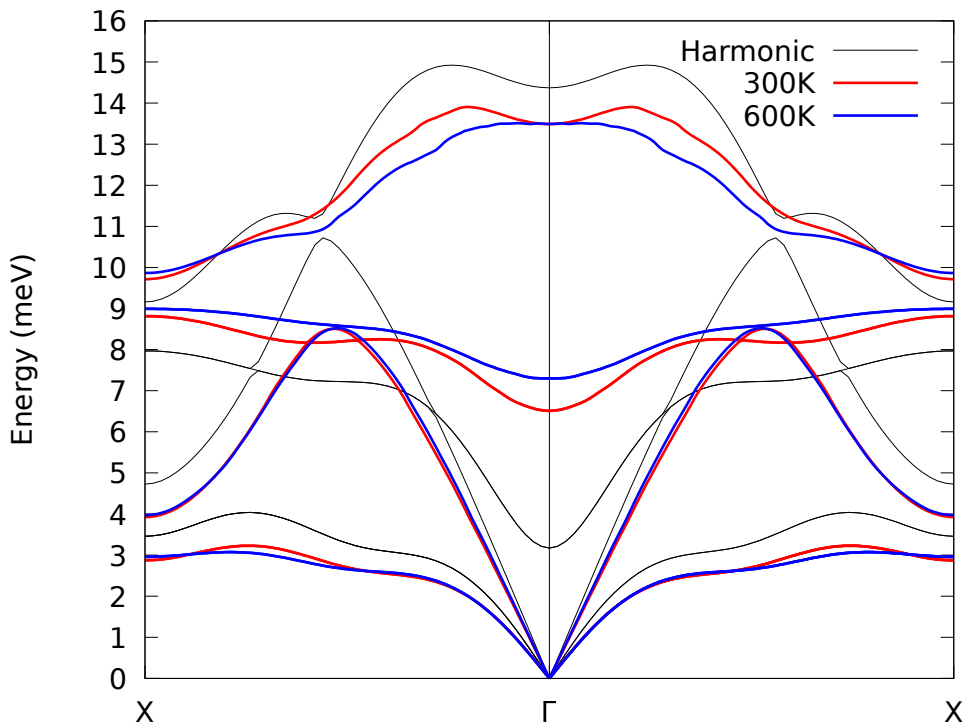


Figure 5.3: PbTe harmonic (dashed lines) and anharmonic (solid lines) phonon dispersion curves at 300 K compared with INS experiments at 300 K (black dots). The anharmonic phonon dispersion ($\Omega_{\mathbf{q}\mu}$) is obtained from Eq.(3.31) and includes the contribution from the *bubble* self-energy.

5.1.2 Satellite peak due to phonon-phonon scattering.

In order to determine if the SSCHA approximation can describe correctly the phonon satellites for PbTe, the phonon self-energy is calculated performing Fourier interpolation over a denser $40 \times 40 \times 40$ phonon momentum grid. Fig.(5.5) and Fig.(5.6) shows our calculated anharmonic phonon dispersion versus the spectral function of PbTe at 300 and 600 K obtained by using the SCHA self-energy.

We also display on Fig.(5.5), with pink dots, the Energy of the TO phonon and of its satellite as measured in INS experiments detailed in ref.[19].

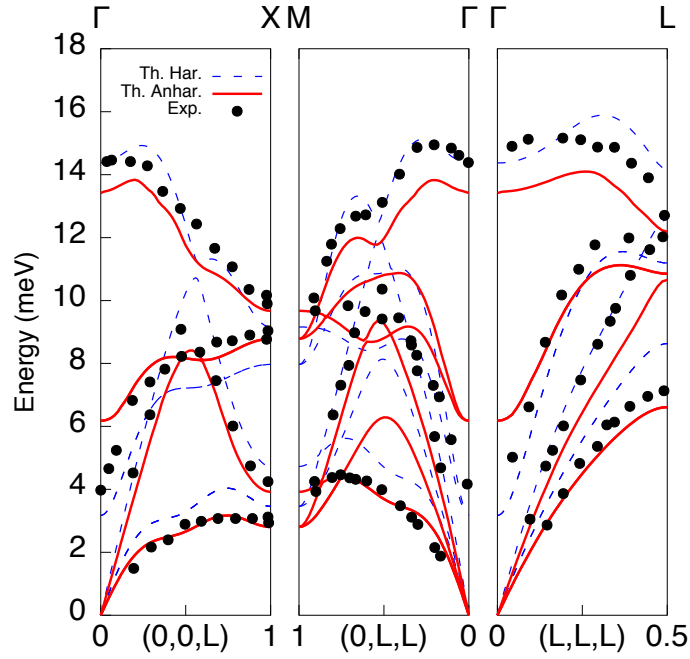


Figure 5.4: PbTe harmonic (dashed lines) and anharmonic (solid lines) phonon dispersion curves at 300 K compared with INS experiments at 300 K (black dots) from ref.[15]. The anharmonic phonon dispersion ($\Omega_{\mathbf{q}\mu}$) is obtained from Eq.(3.31) and includes the contribution from the *bubble* self-energy.

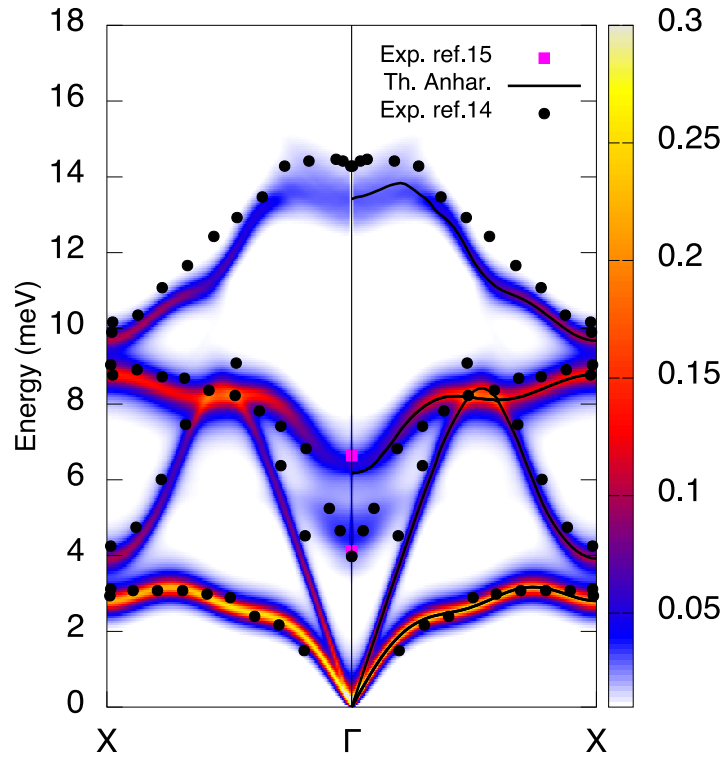


Figure 5.5: PbTe Spectral function at 300 K calculated along the X- Γ -X path (color map). Solid lines denote the anharmonic phonon dispersion curves, black dots denote the experimental data from Ref. and pink squares denote the experimental values for the peaks at the zone center from more recent experiments described in ref.[19]. The color code is determined by the value of $\sigma(\mathbf{q}, \omega)$ in Eq.(3.32).

Both the satellite, more intense for 300 K, and the tendency of a avoided crossing LA and TO bands for temperatures above 600 K are well described by our methodology. Moreover, the energies of the TO peaks at Γ obtained by the SSCHA are compatible with the observed values. The presence of these features were also investigated in the literature using different methods. In particular, non-perturbative methods such as theTDEP were able to obtain similar results [64].

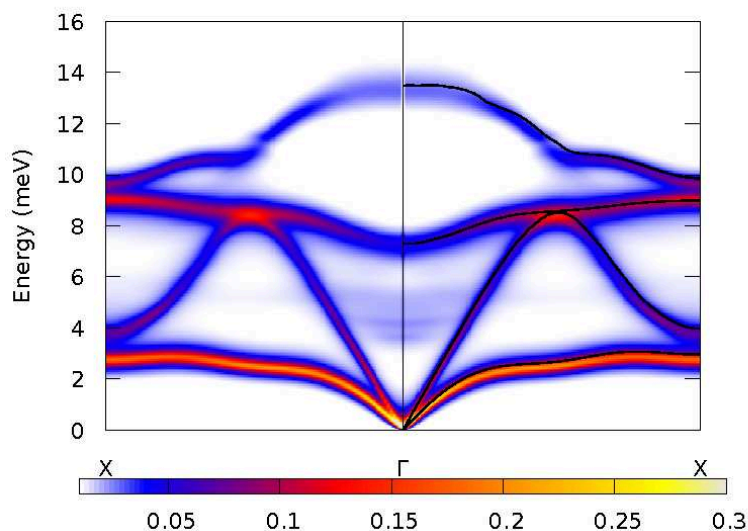


Figure 5.6: PbTe Spectral function at 600 K calculated along the X- Γ -X path (color map). Solid lines denote the anharmonic phonon dispersion curves. The intensity of the satellite peak decreases with increasing temperature, and the TO modes shift towards higher energies.

5.2 Tin telluride (SnTe)

We start our calculation for SnTe by comparing the harmonic spectra and the anharmonic phonon dispersion at 50 and 100 K. On the harmonic case it is evident the presence of the phonon stabilities at the Γ point in the BZ. By raising the temperature, the TO modes shift towards higher energies close to 1.4 meV for $T = 50$ K and 2.4 meV for $T = 100$ K. This range of values is consistent with INS measurements performed by Li et al [20].

Calculations for SnTe are reported in Fig.(5.8) where the comparison between the phonon spectra obtained via SSCHA at $T = 100$ K and recent IXS experiments[84] at $T = 75$ K is shown.

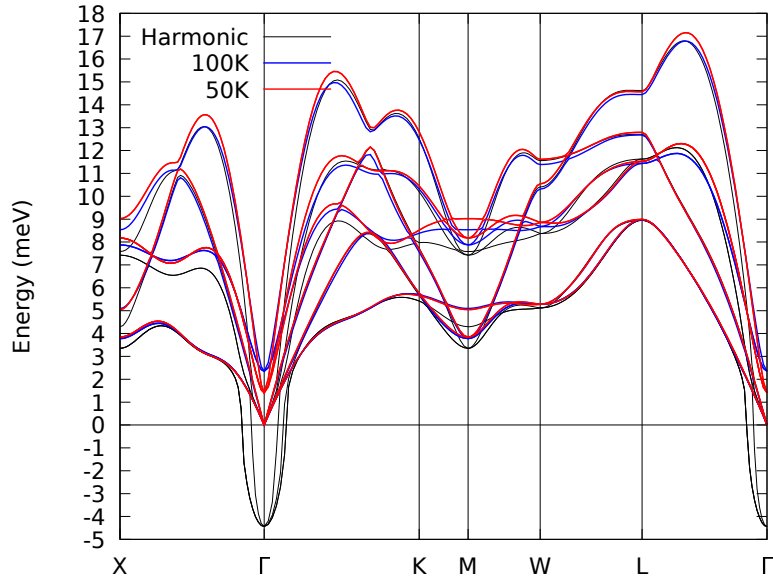


Figure 5.7: Comparison between the harmonic (black lines) and anharmonic phonon dispersion curves of SnTe at 50 K (red lines) and 100 K along special points in the BZ. The anharmonic phonon dispersion ($\Omega_{\mathbf{q}\mu}$) is obtained from Eq.(3.31) and includes the contribution from the *bubble* self-energy.

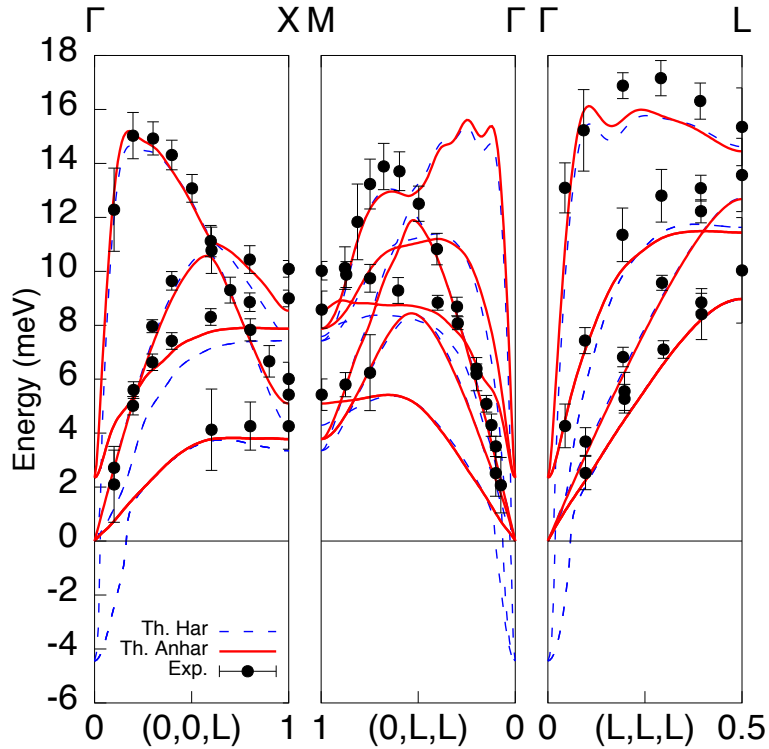


Figure 5.8: Harmonic (dashed lines) and anharmonic (solid lines) phonon dispersion relations of SnTe at 100 K (red lines) compared with IXS experiments [84] at 75 K (black dots). The anharmonic phonon dispersion ($\Omega_{\mathbf{q}\mu}$) is obtained from Eq.(3.31) and includes the contribution from the *bubble* self-energy.

Even, if this system was studied theoretically before, using methods such as the TDEP and self-consistent ab-initio lattice dynamics (SCAILD), the calculations focused on higher temperatures [84]. Our calculated anharmonic dispersion curves present the main features of the experimental data for all investigated high symmetry directions along the BZ. Overall, we find a good agreement with experimental data. It is worth to mention that in order to describe correctly the experimental results the difference between harmonic and anharmonic dynamical matrices are interpolated to a $14 \times 14 \times 14$ supercell for SnTe.

We also calculated the spectral-function for SnTe, considering the $4 \times 4 \times 4$ supercell. Differently from PbTe, we do not find the presence of a satellite peak at zone center as can be seen in Fig.(5.9). This was also observed experimentally by Li et al. [20] via INS measurement.

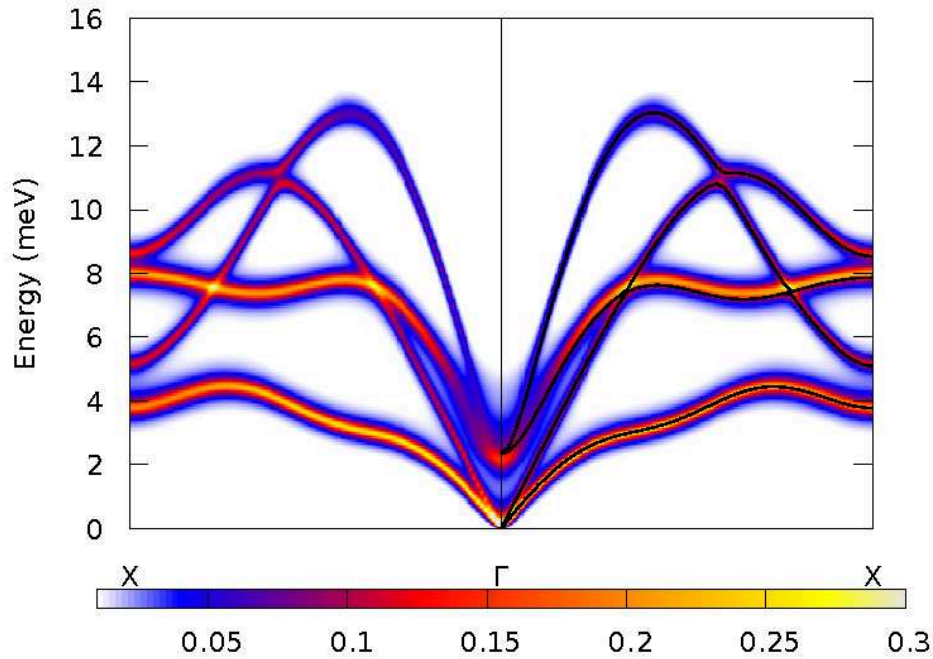


Figure 5.9: SnTe Spectral function at 100 K calculated along the X- Γ -X path (color map). Solid lines denote the anharmonic phonon dispersion curves. We do not find any additional structure on SnTe spectral function. The color code is determined by the value of $\sigma(\mathbf{q}, \omega)$ in Eq.(3.32).

5.2.1 Structural phase transition in SnTe

In order to study the second order structural phase transition in SnTe we evaluate the energy squared of the TO modes at Γ as a function of temperature T . Our data with the inclusion of anharmonicity are consistent with a ferroelectric transition at ≈ 23 K. However, this value should be taken with care as the theoretical calculations are limited by the error in the knowledge of the exchange correlation functional that leads to a big variation in the equilibrium volume. On the other hand, experimentally, the transition temperature of SnTe is strongly dependent on sample doping, varying from 0 K to around 120 K for different carriers concentrations. Fig.(A.5) compares our results for the energy squared of the TO mode with recent IXS [84] experiments.

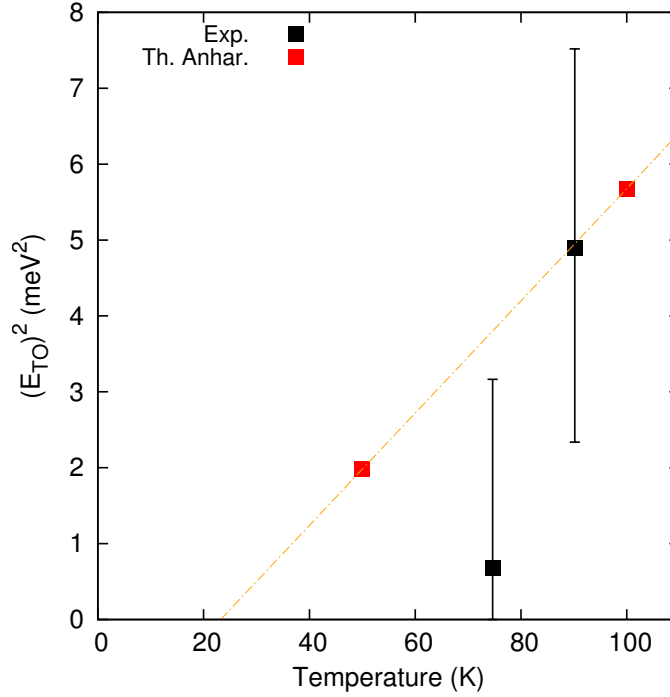


Figure 5.10: Energy square of the TO phonons on the zone-center plotted against temperature. The red squares denote the results obtained by using Eq.(3.31), and black squares results from O'Neill et al.[84]. The linear extrapolation indicates that the the modes softens to zero energy towards $T_c \approx 23$ K for our calculations.

For future applications, a solution to increase the precision of studies concerning structural instabilities, may be the utilization of hybrid functionals, such as the HSE06, that account better for exchange and correlation. Even if we are interested on this matter, this is beyond the scope of this thesis.

5.3 Summary

We successfully applied a novel technique based on the stochastic self-consistent harmonic approximation capable of investigating phase transitions via the calculation of the Hessian of the free energy. We have studied the temperature dependent anharmonic phonon spectra of PbTe and SnTe. We found a strong dependence of vibrational properties on the exchange-correlation functional used in the calculation and on the corresponding equilibrium volume. By using the PBE functional with the theoretical equilibrium volume, we find very good agreement with experimental INS spectra and INS spectra. Then, obtaining a correct description in how the anharmonic phonon dispersions depend on temperature.

By exploring these systems as a theoretical playground, the SSCHA showed to be not only capable of describing single particle spectra, but also manybody features like phonon satellites are correctly explained. Finally, we describe the occurrence ferroelectric transition in SnTe from the high-T rock-salt structure to the low-T rhombohedral one. The value of the ferroelectric critical temperature is found to be strongly dependent in the volume used in the calculations, consequently, on the exchange-correlation functional.

Chapter 6

Conclusion and Perspectives

The goal of this thesis was to apply to thermoelectric systems, such as lead telluride and tin telluride, a novel technique based on the self-consistent harmonic approximation, called stochastic self-consistent harmonic approximation (SSCHA) ; capable to investigate phase transitions and take into account anharmonic effects by the calculation of the free energy Hessian.

We chose PbTe and SnTe due to their simple structure, and also due to the presence of strong anharmonicity. The latter manifests itself in different ways for these compounds, such as the softening of phonon modes with decreasing temperature, the presence of satellite peaks on the PbTe inelastic neutron scattering (INS) spectra, and the phase transition at low temperature observed in SnTe.

This manuscript started by introducing briefly some phenomenology concerning PbTe and SnTe, focusing on the structure, electronic properties, and vibrational properties of these materials. Next, we introduced the harmonic approximation and the density-functional perturbation theory (DFPT) in which one can start to investigate numerically the phonon dispersion curves of materials. On chapter 3 , we discussed the addition of anharmonic term to the ionic potential and some methods to calculate them. In particular, we focused on the SSCHA, trying to write an introduction to its theory and capabilities.

An important part of the work was devoted to test and validate the SSCHA approach and its new implementations by using our systems of interest as playground. We dedicated chapter 4 to discuss tests and first applications pf the SSCHA. The magnitude of anharmonic effects was extensively studied for this systems, making use of an empirical potential and via ab-initio calculations. Next, we compared anharmonic phonon dispersion curves including different contributions to the ionic anharmonic free

energy, finding that terms beyond third-order can be neglected for PbTe and SnTe. Within the same analysis we also estimate the effects of thermal expansion on the phonon frequencies for the PbTe system. Afterwards, we compared results using off-diagonal and diagonal anharmonic phonon self-energies, showing that for both systems, the differences are minimal. In addition, the nature of the stochastic third-order force constants were investigated by comparing our results with third-order force constants calculated via finite differences method on top of the SSCHA phonon spectra. In this case the third order-force constants were used to calculate the contribution of the bubble diagram to the phonon self-energies. Our analysis found that for converged calculations no significant differences are noticed. These results are not important just for our studies but can also be viewed as a protocol to initiate the investigation of anharmonic properties in other materials.

After the testing phase, we carried out full ab-initio calculation in order to compare our findings to experimental data, chapter 5. We studied the temperature dependent anharmonic phonon spectra of PbTe and SnTe at different temperatures. We found a strong dependence of vibrational properties on the exchange-correlation functional used in the calculation and on the corresponding equilibrium volume. By using the PBE functional with the theoretical equilibrium volume, we find very good agreement with experimental INS spectra as well inelastic x-ray scattering (IXS) experiments.

The corrected behavior of the transverse optical (TO) modes with temperature was found for both materials, and the spectra exhibit a good agreement with past measurements in literature. By investigating the spectral function of PbTe and SnTe, we showed that the SSCHA is not only capable of describing single particle spectra, but also manybody features like phonon satellites are correctly reproduced. In addition, we describe the occurrence of a ferroelectric transition in SnTe from the high-T rock-salt structure to the low-T rhombohedral one. The value of the ferroelectric critical temperature is found to be strongly dependent on the volume used in the calculations, and consequently, on the exchange-correlation functional.

We believe that this thesis demonstrated the power of the SSCHA, that can be used in a large variety of systems in future works. For example, it is suitable to study shape memory alloys such as NiTi [88, 89], used in a broad spectrum of technologies, from medical applications to the aerospace industry. This compound in particular exhibits a phase transition, from

a β -phase to R -phase. Its understanding depends on the knowledge of the phonon dispersion. The stability of the β -phase, however, is not described correctly via the harmonic theory, showing instabilities along different points of the BZ. In Fig.(6.1) we show a preliminary analysis on this matter by using the SSCHA. Another possible application is the study of surfaces and thin-films. Following the study of ferroelectric transitions on SnTe, the SSCHA can explore SnTe thin films in which the T_c is enhanced to values close to 270 K [90].

Concerning the developments of the technique, in order to maximize the SSCHA capabilities the computational limitations must be reduced. Since the SSCHA depends on the calculations of interatomic forces and total energies, we believe that an optimization of the implementation, and also the use of alternative way to calculate these objects shall be explored. For instance, the use of empirical potentials, or machine learning techniques can expand the potential of the method, allowing the investigation of larger supercells and a big variety of more complex systems within its framework.

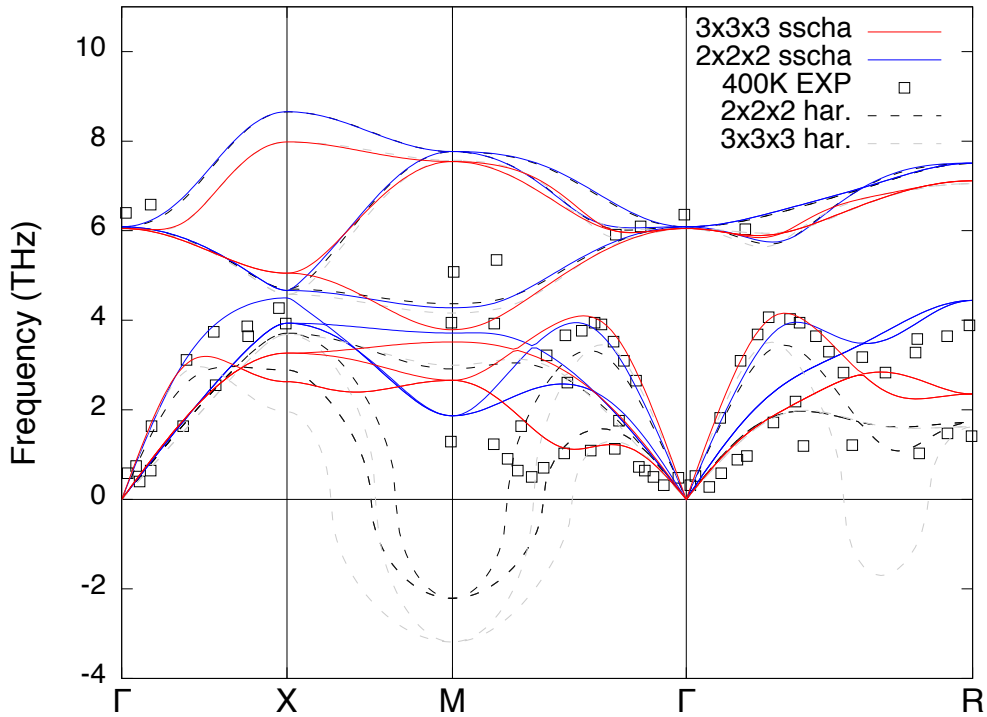


Figure 6.1: Preliminary results on the NiTi system. Tee plot compares experimental data at 400 K (points) with the harmonic phonon dispersion using the $2 \times 2 \times 2$ (black) and $3 \times 3 \times 3$ (black) supercells, and unconverged SSCHA calculations; $2 \times 2 \times 2$ (blue) and $3 \times 3 \times 3$ (red) supercells.

Appendix A

Density functional theory overview

In this appendix we present an short overview of the Density Functional Theory (DFT) focusing on the main theorems and on the Kohn-Sham approach.[36, 37] A deeper discussion including the discussion on approximations for the exchange-correlations terms, plane-waves basis set, and pseudopotentials, can be found in many textbooks, as well in review papers. All calculations presented on this thesis were performed using the DFT as implemented on the QUANTUM ESPRESSO package.

A.1 Hohenberg-Kohn theorems

Via the Born-Oppenheimer approximation it is possible to decouple the electronic from the vibrational degrees of freedom. Hence, one can tackle the electronic problem independently from the vibrational one. The density functional theory (DFT), developed by Hohenberg and Kohn, aims at simplifying the resolution of the electronic problem by reducing the many-body problems with $3N_e$ variables to a simple problem with one parameter, the electronic density. The DFT is based on two theorems rewritten by Martin as:

Theorem. *For any system of interacting particles in an external potential $V_{ext}(\mathbf{r})$, the potential $V_{ext}(\mathbf{r})$ is determined uniquely, except for a constant, by the ground state particle density $n(\mathbf{r}, \mathbf{R})$.*

Theorem. *A universal functional for the energy $E_e[n]$ in terms of the density $n(\mathbf{r}, \mathbf{R})$ can be defined, valid for any external potential $V_{ext}(\mathbf{r})$.*

For any particular $V_{ext}(\mathbf{r})$, the exact ground state energy of the system is the global minimum of this functional, and the density that minimizes the functional is the exact ground state density $n(\mathbf{r}, \mathbf{R})$.

Corollary. *The functional $E_e[n]$ alone is sufficient to determine the exact ground state energy and density.*

In resume, there is an universal functional $F[n(\mathbf{r}, \mathbf{R})]$ of the electron charge density such that the functional

$$E_e[n] = F[n] + \int n(\mathbf{r}, \mathbf{R})V_{ext}(\mathbf{r})d\mathbf{r} \quad (\text{A.1})$$

is minimized by the electron charge density of the ground state corresponding to the external potential $V_{ext}(\mathbf{r})$, under the constraint that the number of electrons is given by the integral of $n(\mathbf{r}, \mathbf{R})$.

A.2 The Kohn-Sham equations

According to the Hohenberg-Kohn theorems, if one can determine the electronic density that minimizes the functional of Eq.(A.1) then the ground state energy of the system is also determined. A practical way to calculate this object is the approach developed by Kohn and Sham. In this approach, the electronic density is written in terms of N_e single particle wavefunctions as

$$n(\mathbf{r}, \mathbf{R}) = \sum_i^{N_e} |\phi(\mathbf{r}, \mathbf{R})|^2. \quad (\text{A.2})$$

This single particle wavefunctions are auxiliary objects with no physical meaning called Kohn-Sham orbitals. On the other hand, the electronic density found by using this object corresponds to the density of the real system. On the spirit of the Kohn-Sham approach the functional $F[n]$ is expressed as

$$F[n] = T_0[n] + \frac{1}{2} \int \frac{n(\mathbf{r}, \mathbf{R})n(\mathbf{r}', \mathbf{R})d\mathbf{r}d\mathbf{r}'}{|\mathbf{r} - \mathbf{r}'|} + E_{xc}[n], \quad (\text{A.3})$$

where $T_0[n]$ is the kinetic-energy functional, the second term is the classical electrostatic self-interaction of the electron charge-density distribution, and the last term is the so called exchange-correlation term. The latter is part of the energy functional we do not know how to evaluate in principle.

Variation of the energy functional with respect to the density $n(\mathbf{r}, \mathbf{R})$,

keeping the number of electrons fixed, leads formally to the same equation as would hold for a system of noninteracting electrons subject to an effective potential $V_{SCF}(\mathbf{r})$, called the self-consistent field (SCF) potential, of the form

$$V_{SCF}(\mathbf{r}) = V_{ext}(\mathbf{r}) + V_{Hartree}(\mathbf{r}) + V_{xc}(\mathbf{r}) \quad (\text{A.4})$$

with

$$V_{Hartree}(\mathbf{r}) = \int \frac{n(\mathbf{r}', \mathbf{R}) d\mathbf{r}'}{|\mathbf{r} - \mathbf{r}'|} \quad (\text{A.5})$$

and

$$V_{xc}(\mathbf{r}) = \frac{\delta E_{xc}[n]}{\delta n(\mathbf{r}, \mathbf{R})}. \quad (\text{A.6})$$

By knowing $V_{SCF}(\mathbf{r})$ and the electronic density in terms of the Kohn-Sham orbitals, Eq.(A.2), one can evaluate the noninteracting electronic problem by solving the one-electron Schroedinger equation

$$\hat{H}_{SCF}(\mathbf{r})\phi_i(\mathbf{r}, \mathbf{R}) = \varepsilon_i\phi_i(\mathbf{r}, \mathbf{R}), \quad (\text{A.7})$$

where

$$\hat{H}_{SCF}(\mathbf{r}) = -\frac{\nabla^2}{2} + V_{SCF}(\mathbf{r}). \quad (\text{A.8})$$

Eq.(A.7) has the form of a nonlinear Schroedinger equation in which the potential depends on its own eigenfunctions through the electronic density, and are denominated Kohn-Sham equations. If the exchange-correlation term is known, then this equation can be solved self-consistently using different methods. The exact V_{xc} potential is not known. Hence, some approximation have to be made in order to treat $V_{xc}(\mathbf{r})$. The most well-known approximations for this contribution are the local density approximation (LDA) and the generalized gradient approximation (GGA). We chose the latter to carry out the DFT calculations described on this thesis.

A.3 Local density approximation (LDA)

Considering that in the limit of the homogeneous electron gas exchange-correlation effects are local in character, Kohn and Sham proposed that the exchange-correlation energy could be approximated simply as an integral over all space with the exchange- correlation energy density at each point assumed to be the same as in a homogeneous electron gas:

$$E_{xc}^{LDA}[n](\mathbf{R}) = \int d\mathbf{r} n(\mathbf{r}, \mathbf{R}) \epsilon_{xc}^{hom}(n(\mathbf{r}, \mathbf{R})). \quad (\text{A.9})$$

Where it is possible to find different parametrizations of ϵ_{xc}^{hom} in literature [91, 92].

A.4 Generalized gradient approximation (GGA)

Due to its local character, the LDA is expected to work better for solids close to a homogeneous electron gas than for more inhomogeneous systems. Kohn and Sham proposed that the LDA could be improved including corrections coming from the gradient of the density. In a similar form as the LDA equation the GGA exchange-correlation can be cast on the following form:

$$E_{xc}^{GGA}[n](\mathbf{R}) = \int d\mathbf{r} f(n(\mathbf{r}, \mathbf{R}), \nabla n(\mathbf{r}, \mathbf{R})). \quad (\text{A.10})$$

There are many parametrizations for the function f in literature [81, 93, 94]. However, there is not a definite value for f making it difficult to encounter the best functional. Hence, the gradient correction to the LDA is not a general improvement and can give worse results for some systems and some properties. As a consequence, the choice of the exchange-correlation which may lead to reliable results is system dependent.

Résumé en français

Introduction

Les matériaux thermoélectriques attirent de plus en plus d'attention en raison de leur propriété de pouvoir convertir la chaleur en énergie électrique et vice-versa [5, 6, 7]. En cas d'utilisation avec des sources d'énergie propres, comme le l'énergie solaire par exemple, de tels matériaux peuvent être une solution alternative au problème d'augmentation de la demande en énergie et d'autres problèmes mondiaux tels que le réchauffement climatique [1, 2, 3]. Le développement et la classification des dispositifs thermoélectriques est lié à une quantité adimensionnelle appelée facteur de mérite qui est donnée par :

$$ZT = \frac{S^2 \sigma T}{k}, \quad (\text{A.11})$$

Où S est le coefficient de Seebeck, T la température, et σ et k sont les conductivités électroniques et thermiques, respectivement. Plus le facteur de mérite est élevé, mieux est le dispositif ferroélectrique.

Dans ces systèmes, les effets anharmoniques jouent un rôle important car ils diminuent la conductivité thermique via la diffusion phonon-phonon et par conséquent, augmentent le facteur ZT . De plus, certains composés thermoélectriques subissent des transitions de phase du second ordre entraînées par des modes phoniques dites « doux ». Proche de la cette transition de phase, les fréquences des phonons deviennent très douces et le potentiel ressenti par les ions fortement anharmoniques. Par conséquent, un traitement non perturbatif de l'anharmonicité est crucial pour comprendre la dynamique du réseau cristallin et l'efficacité des matériaux thermoélectrique. D'un point de vue théorique, plusieurs approximations ont été développées ces dernières années afin de résoudre ce problème, et il devient enfin possible de décrire les effets anharmoniques au-delà le régime perturbatif [76, 77, 16, 18].

Parmi tous les thermoélectriques, le PbTe et le SnTe se distinguent par

leurs propriétés intéressantes [10, 12, 13, 14, 15, 19, 20]. Les deux systèmes ont des facteurs de mérite élevés faisant d’eux des thermoélectriques efficaces. De plus, à température ambiante, ils ont des structures simples de type NaCl. La simplicité de leur structure et l’importance des effets anharmoniques pour décrire les propriétés dynamiques de leurs réseaux cristallins les rendent des systèmes idéals pour valider les approches théoriques non perturbatives du problème anharmonique.

En plus de ses propriétés thermoélectriques, le SnTe exhibe une transition ferroélectrique intrigante à basse température. Cette transition vers une structure rhomboédrique se produit lorsque les modes optiques-transverses (TO) au centre de la zone de Brillouin (BZ) se ramollissent pendant le refroidissement. Les mesures expérimentales, passées et récentes, indiquent que différentes températures de transition, allant de 0 K jusqu’à 120 K existent. Une telle variation de T_c est due à la variation du dopage intrinsèque [28]. D’autre part, le PbTe ne subit pas une transition de phase à basse température, bien qu’il ait un caractère ferroélectrique naissant. De plus, des expériences INS récentes ont rapporté que le PbTe possède un pic de phonon satellite proche du centre de la BZ, ce qui représente une empreinte claire de la forte anharmonicité dans ce matériaux [19].

D’un point de vue théorique, les deux systèmes ont été étudiés dans le passé en utilisant des calculs ab-initio, ainsi que des méthodes basées sur la dynamique moléculaire [76, 77, 20]. La plupart de ces calculs utilisent une approche non-perturbative puisque les calculs basés sur la théorie des perturbations conduisent à des instabilités structurelles totalement absentes dans les mesures expérimentales [77, 87]. Certaines de ces méthodes donnent un bon accord avec l’expérience, spécialement pour le PbTe. Cependant, les résultats peuvent être affectés par une plusieurs facteurs, tels que le volume utilisé durant les calculs [47].

Dans ce résumé, nous présentons les spectres de phonons anharmoniques de PbTe et SnTe en fonction de la température en utilisant l’approximation harmonique stochastique et auto-cohérente (SSCHA) [16, 17, 18]. On déterminera ainsi l’ampleur des effets anharmoniques sur les spectres vibrationnels et sur la transition ferroélectrique.

Ce résumé est organisé dans l’ordre suivant : Tout d’abord, dans la section A.4, nous introduisons le cadre théorique et la méthodologie appliquée. Nous présentons ensuite l’approximation harmonique stochastique auto-cohérente (SSCHA) [16, 17, 18] et, dans ce cadre, l’évaluation de l’Hessien de l’énergie libre [18]. Dans la section A.4, nous discuterons les paramètres utilisés dans nos calculs ab-initio. Les principaux résultats concernant les

dispersions de phonons harmoniques et anharmoniques et la comparaison entre nos calculs et les données expérimentales sont décrits dans la section [A.4](#).

Théorie

Nous étudions la dynamique; des réseaux cristallins du PbTe et du SnTe dans l'approximation de Born-Oppenheimer (BO). Ainsi, nous considérons l'Hamiltonien quantique pour les atomes définis par l'énergie potentielle de BO $V(\mathbf{R})$. La variable \mathbf{R} dans $V(\mathbf{R})$ est une notation compacte (sans composante) de la quantité $R^{\alpha s}(\mathbf{l})$, une coordonnée collective qui spécifie complètement la configuration atomique. L'indice α indique la direction cartésienne, s désigne l'atome dans la cellule unitaire et \mathbf{l} indique un vecteur tridimensionnel du réseau direct (cristallin). Dans la suite, nous utiliserons également un l'index composite $a = (\alpha, s, \mathbf{l})$ qui regroupe l'index cartésien, l'index atomique et le vecteur du réseau direct. De plus, en général, nous utiliserons souvent dans cet article les caractères en gras pour indiquer d'autres quantités en notation compacte.

Afin traiter les effets quantiques et l'anharmonicité dans une approche non-perturbative, nous utilisons l'approximation harmonique stochastique et auto-cohérente (SSCHA) [16, 17, 18]. Pour une température donnée T , la méthode permet de trouver une estimation approximative pour $F(\mathcal{R}^{\alpha s}(\mathbf{l}))$, l'énergie libre du cristal en fonction de la position atomique moyenne $\mathcal{R}^{\alpha s}(\mathbf{l})$ (le *centroids*). Pour un centroid donné \mathcal{R} , l'énergie libre SSCHA est obtenue à travers un Hamiltonien quadratique auxiliaire, appelé l'Hamiltonien de la SSCHA $\mathcal{H}_{\mathcal{R}}$. Dans une transition de phase du second ordre, à haute température, l'énergie libre est minimale pour une configuration de haute symétrie \mathcal{R}_{hs} mais, lors durant le refroidissement, \mathcal{R}_{hs} devient un point-selle à la température de transition T_c . Par conséquent, l'Hessien de l'énergie libre évaluée à \mathcal{R}_{hs} , $\partial^2 F / \partial \mathcal{R} \partial \mathcal{R} |_{\mathcal{R}_{\text{hs}}}$, est définie positive a température élevée, mais elle développe une ou plusieurs directions négatives à T_c . L'Hessien de l'énergie libre SSCHA dans un centroïde \mathcal{R} peut être calculé en utilisant la formule analytique (en notation compacte) [18].

$$\frac{\partial^2 F}{\partial \mathcal{R} \partial \mathcal{R}} = \Phi + \overset{(3)}{\Phi} \Lambda(0) \left[\mathbf{1} - \overset{(4)}{\Phi} \Lambda(0) \right]^{-1} \overset{(3)}{\Phi}, \quad (\text{A.12})$$

avec

$$\overset{(n)}{\Phi}_{a_1 \dots a_n}(\mathcal{R}) = \left\langle \frac{\partial^n U}{\partial R^{a_1} \dots \partial R^{a_n}} \right\rangle_{\rho_{\mathcal{H}}} \quad (\text{A.13})$$

où les moyennes sont par rapport à la matrice densité de l'Hamiltonien SSCHA $\mathcal{H}_{\mathcal{R}}$, c'est-à-dire $\rho_{\mathcal{H}_{\mathcal{R}}} = e^{-\beta\mathcal{H}_{\mathcal{R}}}/\text{tr}[e^{-\beta\mathcal{H}_{\mathcal{R}}}]$, et $\beta = (k_b T)^{-1}$ où k_b est la constante de Boltzmann. Dans Eq. A.12 la valeur à $z = 0$ du tenseur de 4ème ordre $\Lambda(z)$ est utilisée. Pour un nombre complexe générique z , ce tenseur est défini par :

$$\Lambda^{abcd}(z) = -\frac{1}{2} \sum_{\mu\nu} F(z, \omega_\mu, \omega_\nu) \times \sqrt{\frac{\hbar}{2M_a\omega_\mu}} e_\mu^a \sqrt{\frac{\hbar}{2M_b\omega_\nu}} e_\nu^b \sqrt{\frac{\hbar}{2M_c\omega_\mu}} e_\mu^c \sqrt{\frac{\hbar}{2M_d\omega_\nu}} e_\nu^d, \quad (\text{A.14})$$

avec M_a la masse de l'atome a , ω_μ^2 et e_μ^a les valeurs et vecteurs propres de $D^S = \Phi_{ab}/\sqrt{M_a M_b}$, respectivement, et

$$F(z, \omega_\nu, \omega_\mu) = \frac{2}{\hbar} \left[\frac{(\omega_\mu + \omega_\nu)[1 + n_B(\omega_\mu) + n_B(\omega_\nu)]}{(\omega_\mu + \omega_\nu)^2 - z^2} - \frac{(\omega_\mu - \omega_\nu)[n_B(\omega_\mu) - n_B(\omega_\nu)]}{(\omega_\mu - \omega_\nu)^2 - z^2} \right] \quad (\text{A.15})$$

où $n_B(\omega) = 1/(e^{\beta\hbar\omega} - 1)$ est le numéro d'occupation bosonique. En évaluant l'hessienne de l'énergie libre à \mathcal{R}_{hs} Eq.A.12 et en étudiant son spectre en fonction de la température, on peut prédire l'occurrence d'une transition de phase du second ordre et estimer T_c . En particulier, puisque nous considérons un cristal, nous profitons de la périodicité du réseau et nous utiliseront la transformée de Fourier de l'hessienne de l'énergie libre par rapport aux indices de réseau. Par conséquent, puisqu'il y a 2 atomes dans la cellule unitaire de PbTe et SnTe, nous calculons en fait les valeurs propres $\lambda_\mu^2(\mathbf{q})$ de la matrice carrée de 6^{ème} order $\partial^2 F/\partial\mathcal{R}^{\alpha s}(-\mathbf{q})\partial\mathcal{R}^{\beta t}(\mathbf{q})$ pour différents points \mathbf{q} de la BZ.

Comme le montre la Réf.[18], dans le formalisme de la SSCHA, il est possible de formuler un *ansatz* afin de donner une expression approximative à la fonction de Green du phonon ($\mathbf{G}z$) pour la variable $\sqrt{M_a}(R^a - \mathcal{R}_{\text{hs}}^a)$

$$\mathbf{G}^{-1}(z) = z^2 \mathbf{1} - \mathbf{M}^{-\frac{1}{2}} \Phi \mathbf{M}^{-\frac{1}{2}} - \mathbf{\Pi}(z) = -\mathbf{D}^{(F)}, \quad (\text{A.16})$$

Où $\mathbf{\Pi}(z)$ est la self-énergie de la SSCHA, donnée par

$$\mathbf{\Pi}(z) = \mathbf{M}^{-\frac{1}{2}} \overset{(3)}{\Phi} \Lambda(z) \left[\mathbf{1} - \overset{(4)}{\Phi} \Lambda(z) \right]^{-1} \overset{(3)}{\Phi} \mathbf{M}^{-\frac{1}{2}}, \quad (\text{A.17})$$

où $M_{ab} = \delta_{ab}M_a$ est la matrice de masse. Pour les applications pris en considération dans cette thèse, le terme statique $bP_{ssf}hi\Lambda(0)$ est négligeable par rapport à la matrice d'identité. L'utilisation de cette approximation dans le cas dynamique réduit la self-énergie de la SSCHA à la self-énergie dite de « bulle », à savoir

$$\mathbf{\Pi}(z) \approx \mathbf{\Pi}^{(B)}(z) = \mathbf{M}^{-\frac{1}{2}} \mathbf{\Phi}^{(3)} \mathbf{\Lambda}(z) \mathbf{\Phi}^{(3)} \mathbf{M}^{-\frac{1}{2}}, \quad (\text{A.18})$$

On néglige alors le mélange entre différents modes de phonons et supposons que $\mathbf{\Pi}(z)$ est diagonal dans la base des vecteurs propres $e_{\mu}^{\alpha s}(\mathbf{q})$ of $\Phi_{\alpha s, \beta t}(\mathbf{q})/\sqrt{M_s M_t}$ où $\Phi_{\alpha s, \beta t}(\mathbf{q})$ est la transformée de Fourier de $\Phi_{\alpha s, \beta t}$. Nous définissons ensuite

$$\Pi_{\mu}(\mathbf{q}, \omega) = \sum_{\alpha s, \beta t} e_{\mu}^{\alpha s}(\mathbf{q}) \Pi_{\alpha s \beta t}(\mathbf{q}, \omega + i0^+) e_{\mu}^{\beta t}(\mathbf{q}) \quad (\text{A.19})$$

et $\omega_{\mu}^2(\mathbf{q})$ sont les valeurs propres de la transformée de Fourier de $\mathbf{D}^{(S)}$. Les fréquences des phonons au carré, $\Omega_{\mathbf{q}\mu}^2$, corrigées par la self-énergie de it bulle sont obtenus comme

$$\Omega_{\mathbf{q}\mu}^2 = \omega_{\mu}^2(\mathbf{q}) + \text{Re}\Pi_{\mu}(\mathbf{q}, \omega_{\mathbf{q}\mu}) \quad (\text{A.20})$$

En étudiant la réponse d'un réseau à la diffusion des neutrons, nous avons besoin de la fonction spectrale à un phonon. En utilisant Eq. (A.16) pour $\mathbf{G}(z)$ nous pouvons calculer la section efficace $\sigma(\omega) = -\omega \text{Tr} \text{Im} \mathbf{G}(\omega + i0^+)/\pi$, dont les sommets indiquent la présence d'excitations vibratoires collectives (phonons) ayant certaines énergies, car elles peuvent être sondées avec des expériences de diffusion inélastiques (ici le facteur de normalisation choisi est tel que $\int d\omega \sigma(\omega)$ est égal au nombre total de modes). Encore une fois, nous profitons de la périodicité du réseau en utilisant la transformée de Fourier des quantités intéressantes par rapport aux indices de réseau. En particulier, nous considérons la transformée de Fourier de la self énergie de la SSCHA, $\Pi_{\alpha s \beta t}(\mathbf{q}, z)$. En négligeant le mélange entre les différents modes, la section est alors donnée par

$$\sigma(\mathbf{q}, \omega) = \frac{1}{\pi} \sum_{\mu} \frac{-\omega \text{Im}\Pi_{\mu}(\mathbf{q}, \omega)}{(\omega^2 - \omega_{\mu}^2(\mathbf{q}) - \text{Re}\Pi_{\mu}(\mathbf{q}, \omega))^2 + (\text{Im}\Pi_{\mu}(\mathbf{q}, \omega))^2}. \quad (\text{A.21})$$

Méthodologie

Nous effectuons nos calculs dans le formalisme de la théorie de la fonctionnelle de densité (DFT) en utilisant le logiciel QUANTUM-ESPRESSO [80]. Dans les deux systèmes, l'interaction d'échange-corrélation est traitée dans l'approximation de gradient généralisée de Perdew-Burke-Ernzerhof (PBE) [81]. Pour décrire l'interaction entre les électrons et les ions, nous utilisons des pseudopotentiels à norme conservée [82] pour le PbTe, et PAW [83] pour le SnTe. Dans les deux systèmes, les états semi-core de valence inclus sont les $4d$ pour Te et Sn, et les $5d$ pour Pb. Les fonctions d'ondes électroniques sont décomposées en une somme d'ondes planes avec un seuil maximale d'énergie cinétique de 65 Ry et 28 Ry pour les pseudopotentiels relativistes scalaires de PbTe et SnTe respectivement. Les intégrations sur la zone de Brillouin (BZ) sont effectuées en utilisant une grille uniforme de $8 \times 8 \times 8\mathbf{k}$ -points pour PbTe et une grille plus dense de $12 \times 12 \times 12\mathbf{k}$ pour SnTe. Un soin particulier doit être pris en convergeant l'énergie de l'états fondamentale par rapport aux points \mathbf{k} pour le SnTe car la profondeur du puits de potentiel en tant que fonction des déplacements de phonons dépend fortement de l'échantillonnage de la BZ. Les calculs antérieurs [20] effectués avec des échantillonnages raréfiés s'avèrent être non-convergé. Les charges efficaces de Born calculées par la théorie de perturbation de la fonctionnelle de densité (DFPT) sont incluses pour les calculs de PbTe seulement. Pour le PbTe et le SnTe, nous considérons la structure sel (NaCl) à haute température et les paramètres de réseau optimisés en PBE qui sont de 6.55 Å et 6.42 Å respectivement.

Les fréquences harmoniques des phonons sont calculées dans le formalisme de la DFPT [53] e utilisant la version implémenté dans QUANTUM-ESPRESSO. Nous utilisons les grilles $2 \times 2 \times 2$, puis $4 \times 4 \times 4 \mathbf{q}$ pour les deux systèmes. L'interpolation de Fourier est utilisée pour obtenir la dispersion des phonons suivant des lignes de haute symétrie.

Pour calculer les fréquences des phonons renormalisées par les effets anharmoniques, nous utilisons le formalisme de la SSCHA [16, 17, 18]. L'Hamiltonien d'essai a est minimisé dans une super-cellule. Ce processus de minimisation nécessite la connaissance des énergies et des forces agissant sur une super-cellule pour un ensemble de configurations aléatoires générées par la matrice de densité d'essai. Ces quantités (énergies et forces) ont été calculés sur les super-cellules $2 \times 2 \times 2$ et $4 \times 4 \times 4$ en utilisant les mêmes paramètres que ceux utilisés pour les calculs harmoniques (DFPT). Le nombre de configurations aléatoires que nous utilisons est de l'ordre de

mille. La différence entre les matrices dynamiques harmoniques et anharmoniques est interpolée sur une grille de $14 \times 14 \times 14$ pour SnTe. Pour le PbTe aucune interpolation n'est nécessaire puisque la super-cellule $4 \times 4 \times 4$ est déjà adéquate pour décrire les résultats expérimentaux.

Résultats & Discussion

Dispersion des phonons harmonique

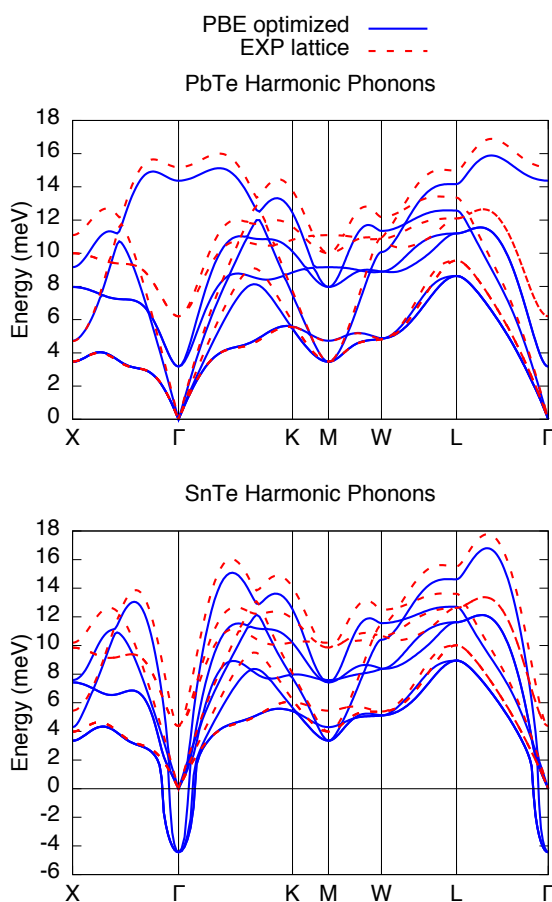


Figure A.1: Courbe de dispersion des phonons harmoniques pour PbTe et SnTe pour différents paramètres de mailles. Pour les paramètres de mailles expérimentaux (lignes rouges) chaque système ne présente aucune fréquence négative. Pour les paramètres de mailles optimisés par la méthode PBE (lignes bleues), le spectre phononique du SnTe montre des fréquences négatives au point Γ , indiquant ainsi une instabilité structurelle. Les modes TO au point gamma a une forte dépendance sur le volume..

Dans les matériaux ferroélectriques et thermoélectriques, les spectres de phonons dépendent fortement du volume utilisé dans les calculs [47],

de ce fait, nous étudions d'abord la dépendance des spectres de phonons harmoniques en fonction des paramètres du réseau. Dans la Fig.(A.1), on montre nos calculs des dispersions de phonons harmoniques au sein de la DFPT pour le PbTe et le SnTe en utilisant (i) les paramètres de maille PBE à température nulle (ii) les valeur expérimentales [26, 27] $a_{\text{exp}} = 6.46\text{\AA}$ et 6.32\AA respectivement. Dans les deux cas, les paramètres expérimentaux sont plus petit que les valeurs théoriques, comme si le système subit une pression finie. Comme prévu, les résultats dépendent fortement du volume. Dans le cas de PbTe, l'utilisation du paramètre de réseau expérimental durcit tous les phonons, mais le durcissement est particulièrement important pour le mode optique transverse (TO) au centre de la BZ qui se décale de $3,17\text{ meV}$ à $6,19\text{ meV}$. Cependant, dans les deux cas, les fréquences des phonons harmoniques sont positives et aucune instabilité structurelle n'est détectée dans PbTe, en accord avec les données expérimentales. Le PbTe est habituellement référencé comme ferroélectrique débutant en raison de la douceur du mode phonon TO. Il est important de souligner que dans le cas du PbTe, les expériences [42, 19] montre un levée de dégénérescence clair entre les modes de phonon LO/TO. Nous avons donc inclus cet effet dans notre calcul harmonique.

A la pression ambiante, le SnTe subit une transition de phase dans la plage de température de 30 à 100 K. A basse température, le cristal passe de la symétrie cubique ($Fm\bar{3}m$) à la symétrie rhomboédrique ($R\bar{3}m$). La distorsion est une transition de phase de déplacement impliquant une petite dimérisation dans la cellule unitaire [30]. Cette distorsion est compatible avec une instabilité d'un phonon au centre de la BZ. Les échantillons réels du SnTe sont non stœchiométriques et la température de transition ferroélectrique dépend fortement du nombre de trous présents dans le système. Elle est d'environ 100 K pour des concentrations de trou de l'ordre de $1 \times 10^{20}\text{ cm}^{-3}$ et diminue jusqu'à environ 30 K pour des concentrations de trous dix fois plus grandes. A ce niveau élevé de dopage, on ne s'attend pas à une levée de dégénérescence LO /TO, qui sera donc négligée dans la simulation

La dépendance du calcul harmonique sur le volume est plus forte dans le cas du SnTe. La transition ferroélectrique (phonon TO imaginaire au centre de la BZ) est présente lors de l'utilisation du volume théorique du PBE alors qu'elle disparaît si le volume expérimental est utilisé. Cela indique à nouveau le rôle important du volume utilisé dans le calcul des spectres de phonons dans ferroélectriques et thermoélectriques. Dans le reste de l'article, nous considérons le paramètre de réseau optimisé PBE à $T = 0\text{ K}$

dans tous les calculs. Pour le SnTe, comme nous nous intéressons aux températures inférieures à 100 K, nous négligeons les effets de la dilatation thermique.

Phonons anharmoniques

Tellurure de plomb (PbTe)

Dans la Fig. A.2 Nous comparons les courbes de dispersion de phonons du PbTe à 300 K obtenues par la SSCHA aux données expérimentales INS obtenues par Cochran et al. [42]. Nos courbes calculées sont en bon accord avec les résultats expérimentaux. Nous obtenons une valeur plus élevée que les expériences pour les modes TO au centre de la BZ ce qui est cohérent avec les observations expérimentales plus récentes d'un double pic dans cette région [19]. Les calculs antérieurs [87] ont trouvé un bon accord pour le mode TO d'énergie inférieure au point Γ , sans pour autant obtenir une bonne description des branches de phonons de haute énergie. Des mesures plus récentes de l'INS [19] ont suggéré la présence d'un phonon satellite fortement dépendant de la température près du point Γ et proviennent du mode TO. En outre, lorsque la température augmente, un croisement évité entre les branches de phonons LA et TO le long de la direction Γ X est rapporté à $T > 300$ K.

Afin de déterminer si l'approximation SSCHA peut décrire les phonons satellites et d'étudier l'occurrence du croisement évité, on calcule la self-énergie des phonons sur une grille plus dense de $40 \times 40 \times 40$. La Fig.(??) montre notre dispersion de phonons anharmoniques calculée comparée à la fonction spectrale du PbTe obtenue en utilisant la self-énergie de la SSCHA.

Nous montrons également, avec des points roses, l'énergie des phonons TO et de leurs satellites telle que mesurée dans les expériences INS détaillées dans la Réf.[19].

Le satellite et le croisement des bandes LA et TO à 300 K sont bien décrits par notre méthodologie. De plus, les énergies des pics TO à Γ obtenus par le SSCHA sont en accord avec les valeurs observées. La présence de ces caractéristiques a également été étudiée dans la littérature en utilisant différentes méthodes. En particulier, des méthodes non perturbatives telles que la technique du potentiel effectif dépendant de la température (TDEP) [64] avec laquelle des résultats similaires ont été obtenues.

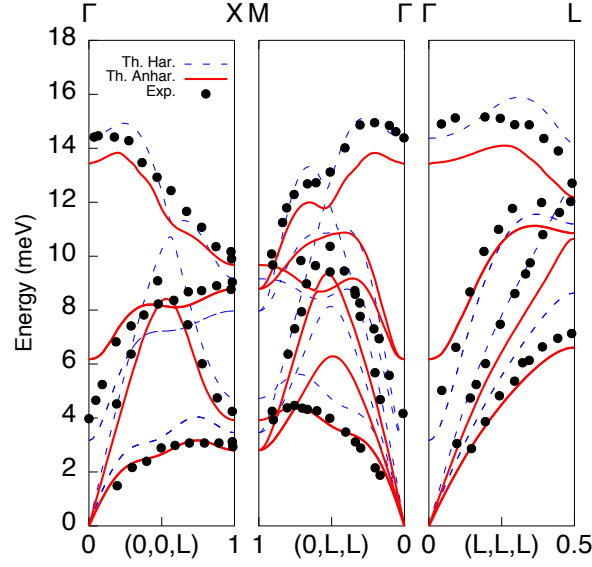


Figure A.2: Courbes de dispersion des phonons harmoniques (lignes pointillées) et anharmoniques (lignes pleines) pour PbTe à 300 K, comparées avec les expériences INS [42] à 300K. La courbe de dispersion des phonons anharmoniques ($\Omega_{\mathbf{q}\mu}$) est obtenue d'après l'équation (A.20) et comprend la contribution de l'énergie propre sous la forme *bulle*.

Tellurure d'étain (SnTe)

Les calculs pour le SnTe sont reportés sur la figure (A.4) où une comparaison entre les spectres de phonons obtenus via SSCHA à $T = 100 K$ et les expériences d'IXS récentes [84] à $T = 75 K$ est présentée. Même si ce système a été étudié théoriquement auparavant en utilisant des méthodes telles que le TDEP et la dynamique du réseau (SCAILD) auto-cohérent [84], les calculs ont porté sur des températures élevées. Nos courbes de dispersion anharmonique calculées présentent les principales caractéristiques des données expérimentales pour toutes les directions de haute symétrie étudiées le long de la BZ. Dans l'ensemble, nous trouvons un bon accord avec les données expérimentales.

Afin d'étudier la transition de phase structurale du second ordre dans le SnTe, nous évaluons le carré de l'énergie des modes TO à Γ en fonction de la température T . Nos données avec l'inclusion de l'anharmonicité sont cohérentes avec une transition ferroélectrique à $\approx 23 K$. Cependant, cette valeur doit être prise avec précaution car les calculs théoriques sont limités par l'erreur dans la connaissance de la fonction d'échange et corrélation qui conduit à une grande variation dans le volume d'équilibre. D'autre part,

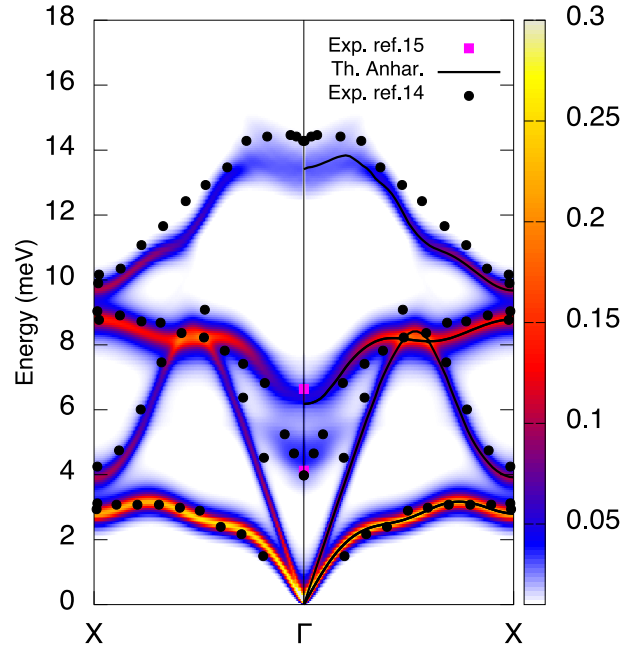


Figure A.3: Fonction spectrale de PbTe à 300K calculée le long de la trajectoire X- Γ -X (carte en couleur). Les lignes pleines représentent les courbes de dispersions des phonons anharmoniques, les points noirs les données expérimentales de réf.[42] et les carrés roses les valeurs expérimentales du pics pour le centre de zone d'après les expériences plus récentes de la réf.[19]. Le code de couleur est déterminé par la valeur de $\sigma(\mathbf{q}, \omega)$, équation (A.21).

expérimentalement, la température de transition de SnTe dépend fortement du dopage de l'échantillon, variant de 0 K à environ 120 K pour différentes concentrations de porteurs. La figure (A.5) compare nos résultats concernant le carré l'énergie du mode TO avec les expériences IXS [84] récentes.

Conclusions

Nous avons appliqué une nouvelle technique [18] basée sur utilisant l'approximation harmonique stochastique et auto-cohérente qui nous a permis d'étudier la transition de phase via le calcul de l'hessienne de l'énergie libre. Nous avons étudié les spectres de phonons anharmoniques dépendant de la température du PbTe et du SnTe. Nous avons trouvé une forte dépendance de propriétés vibrationnelles en fonction de la fonctionnel d'échange et corrélation utilisée dans le calcul ab-initio et sur le volume d'équilibre correspondant. En utilisant la fonctionnelle PBE avec le volume théorique d'équilibre, nous trouvons un très bon accord avec les expériences d'INS. Le formalisme de la SSCHA n'est pas seulement capable de décrire les spectres à une seule

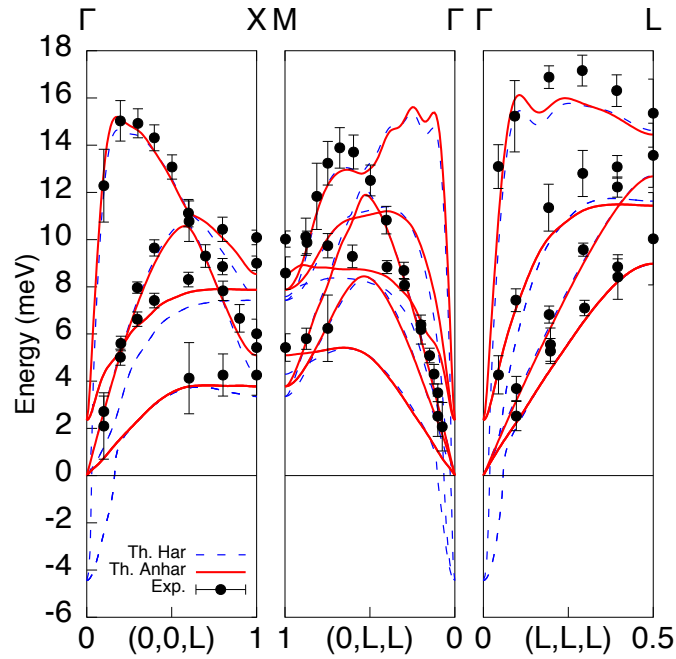


Figure A.4: Courbes de dispersion des phonons harmoniques (lignes pointillées) et anharmoniques (lignes pleines) pour SnTe à 100 K (lignes rouges), comparées avec les expériences IXS [84] à 75K (points noirs). La courbe de dispersion anharmonique ($\Omega_{\mathbf{q}\mu}$) est obtenue d'après l'équation (A.20) et comprend la contribution de l'énergie propre sous la forme *bulle*.

particule, mais aussi de nombreuses propriétés (comme les satellites des phonons TO) sont correctement expliquées. Enfin, nous décrivons la transition de phase ferroélectrique dans SnTe de la structure $Tm\bar{3}m$ à haute température vers la structure $R3m$ à basse température. La valeur de la température critique ferroélectrique dépendant fortement du volume utilisé dans les calculs, par conséquent, de la fonctionnelle d'échange et corrélation.

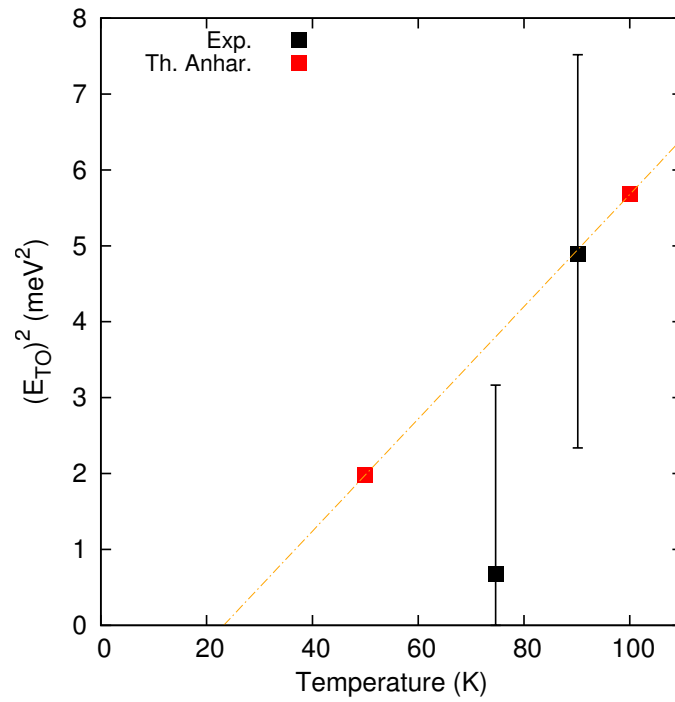


Figure A.5: Énergie au carré pour les phonons TO au centre de la zone en fonction de la température. Les carrés rouges présentent les résultats obtenus à l'aide de l'équation (A.20), et les carrés noirs présentent les résultats d'O'Neil et al.[84]. L'extrapolation linéaire montre que les modes s'annulent à une énergie nulle aux alentours de la $T_c \approx 23 \text{ K}$ d'après nos calculs.

Bibliography

- [1] M. Morini, M. Pinelli, P. R. Spina, and M. Venturini *Applied Energy*, vol. 112, p. 205, 2013.
- [2] S. Varnhagen, A. Same, J. Remillard, and J. W. Park *Journal of Power Sources*, vol. 196, no. 6, p. 3360, 2011.
- [3] S. FuiTie and C. WeiTan *Renewable and Sustainable Energy Reviews*, vol. 20, p. 82, 2013.
- [4] A. Royale and M. Simic *Procedia Computer Science*, vol. 60, p. 1443, 2015.
- [5] A. Montecucco, J. R. Buckle, and A. R. Knox *Applied Thermal Engineering*, vol. 35, p. 177, 2012.
- [6] R. J. Goldstein, W. E. Ibele, S. V. Patankar, T. W. Simon, T. H. Kuehn, P. J. Strykowski, K. K. Tamma, J. V. R. Heberlein, J. H. Davidson, J. Bischof, F. A. Kulacki, U. K. S. Garrick, V. Srinivasan, K. Ghosh, and R. Mittal *International Journal of Heat and Mass Transfer*, vol. 53, no. 21-22, p. 4397, 2010.
- [7] S. Twaha, J. Zhu, Y. Yan, and B. Li *Renewable and Sustainable Energy Reviews*, vol. 65, p. 698, 2016.
- [8] G. J. Snyder and E. S. Toberer *Nature Materials*, vol. 7, p. 105, 2008.
- [9] F.D.Rosi *Solid-State Electronics*, vol. 11, no. 9, p. 849, 1968.
- [10] C. Wood *Reports on Progress in Physics*, vol. 51, p. 459, 1988.
- [11] V. L. Kuznetsov, L. A. Kuznetsova, A. E. Kaliazin, and D. M. Rowe *Journal of Materials Science*, vol. 37, no. 14, p. 2893, 2002.
- [12] Y. Gelbstein, Z. Dashevsky, and M. P. Dariel *Physica B: Condensed Matter*, vol. 363, no. 1-4, p. 196, 2005.

-
- [13] G. S., W. Cochran, R. A. Cowley, and G. Dolling *Physical Review Letters*, vol. 17, p. 753, 1966.
- [14] E. R. Cowley, J. K. Darby, and G. S. Pawley *Journal of Physics C: Solid State Physics*, vol. 2, p. 1916, 1969.
- [15] W. Cochran, R. A. Cowley, G. Dolling, and M. Elcombe *Proceedings of the Royal Society A*, vol. 293, 1966.
- [16] I. Errea, M. Calandra, and F. Mauri *Physical Review Letters*, vol. 111, p. 177002, 2013.
- [17] I. Errea, M. Calandra, and F. Mauri *Physical Review B*, vol. 89, p. 064302, 2014.
- [18] R. Bianco, I. Errea, L. Paulatto, M. Calandra, and F. Mauri *Physical Review B*, vol. 96, p. 014111, 2017.
- [19] O. Delaire, J. Ma, K. Marty, A. F. May, M. A. McGuire, M.-H. Du, D. J. Singh, A. Podlesnyak, G. Ehlers, M. D. Lumsden, and B. C. Sales *Nature Materials*, vol. 8, p. 614, 2011.
- [20] C. Li, O. Hellman, A. M. J. Ma, H. Cao, X. Chen, A. Christianson, G. Ehlers, D. Singh, B. Sales, and O. Delaire *Physical Review Letters*, vol. 112, p. 175501, 2014.
- [21] L. Muldawer *Bulletin of the American Physical Society*, vol. 38, p. 443, 1975.
- [22] L. Muldawer *Journal of Nonmetals*, vol. 1, p. 117, 1973.
- [23] L. J. Brillson, E. Burstein, , and L. Muldawer *Physical Review B*, vol. 9, p. 1574, 1974.
- [24] Y. Tanaka, Z. Ren, T. Sato, K. Nakayama, S. Souma, T. Takahashi, K. Segawa, and Y. Ando *Nature Materials*, vol. 8, p. 800, 2012.
- [25] X.-L. Qi and S.-C. Zhang *Review of Modern Physics*, vol. 83, p. 1057, 2011.
- [26] K. Dalven *Infrared Physics*, vol. 9, p. 141, 1969.
- [27] R. F. Brebrick *Journal of Physics and Chemistry of Solids*, vol. 32, p. 551, 1971.

- [28] K. L. S. Kobayashi, Y. Kato, Y. Katayama, and K. F. Komatsubara *Physical Review Letters*, vol. 37, p. 772, 1976.
- [29] Landolt-Börnstein, *Non-Tetrahedrally Bonded Elements and Binary Compounds*, vol. 41. Springer.
- [30] A. N. Mariano and K. L. Chopra *Applied Physics Letters*, p. 282, 1967.
- [31] K. M. Rabe and J. D. Joannopoulos *Physical Review B*, vol. 32, no. 4, p. 2302, 1985.
- [32] M. E. Lines and A. M. Glass, *Principles and Applications of Ferroelectrics and Related Materials*. Oxford, 1977.
- [33] J. O. Dimmock, I. Melngailis, and A. J. Strauss *Physical Review Letters*, vol. 16, p. 1193, 1966.
- [34] L. Esaki and P. J. Stiles *Physical Review Letters*, vol. 16, p. 1108, 1966.
- [35] P. B. Littlewood, B. Mihaila, R. K. Schulze, D. J. Safarik, J. E. Gubernatis, A. Bostwick, E. Rotenberg, C. P. Opeil, T. Durakiewicz, J. L. Smith, and J. C. Lashley *Physical Review Letters*, vol. 105, p. 086404, 2010.
- [36] P. Hohenberg and W. Kohn *Physical Review*, vol. 136, p. B864, 1964.
- [37] W. Kohn and L. J. Sham *Physical Review*, vol. 140, p. A1133, 1965.
- [38] M. C. Payne, M. P. Teter, D. C. Allan, T. A. Arias, and J. D. Joannopoulos *Review of Modern Physics*, vol. 64, p. 1045, 1992.
- [39] S.-H. Wei and A. Zunger *Physical Review B*, vol. 55, p. 13605, 1997.
- [40] K. Hummer, A. Grüneis, , and G. Kresse *Physical Review B*, vol. 75, p. 195211, 2007.
- [41] J. Heyd and G. E. Scuseria *Journal of Chemical Physics*, vol. 118, no. 18, p. 8207, 2003.
- [42] D. Parker, X. Chen, and D. J. Singh *Physical Review Letters*, vol. 110, p. 146601, 2013.
- [43] L. Xu, H.-Q. Wang, and J.-C. Zheng *Journal of Electronic Materials*, vol. 40, p. 641, 2011.

-
- [44] G. A. Akhmedova and D. S. Abdinov *International Journal of Thermophysics*, vol. 45, p. 854, 2009.
- [45] Q. Zhang, B. Liao, Y. Lan, K. Lukas, W. Liu, K. Esfarjani, C. Opeil, D. Broido, G. Chen, and Z. Ren *Proceedings of the National Academy of Sciences USA*, vol. 110, p. 13261, 2013.
- [46] K. M. O. Jensen, E. S. Bozin, C. D. Malliakas, M. B. Stone, M. D. Lumsden, M. G. Kanatzidis, S. M. Shapiro, and S. J. L. Billinge *Physical Review B*, vol. 86, p. 085313, 2012.
- [47] A. S. J. An and D. J. Singh *Solid State Communications*, vol. 148, p. 417, 2008.
- [48] H. A. Alperin, S. J. Pickart, J. J. Rhyne, and V. J. Minkiewicz *Physical Review Letters*, vol. 40A, p. 295, 1972.
- [49] B. Fultz *Progress in Materials Science*, vol. 55, no. 4, p. 247, 2010.
- [50] R.F.Brebrick *Journal of Physics and Chemistry of Solids*, vol. 24, no. 1, p. 27, 1963.
- [51] J. Kohanoff, *Electronic Structure Calculations for Solids and Molecules: Theory and Computational Methods*. Cambridge, 2006.
- [52] R. M. Martin, *Electronic Structure: Basic Theory and Practical Methods*. Cambridge, 2008.
- [53] S. Baroni, S. de Gironcoli, A. D. Corso, and P. Giannozzi *Review of Modern Physics*, vol. 75, p. 515, 2001.
- [54] M. Born and R. Oppenheimer *Annalen der Physik*, vol. 20, p. 457, 1927.
- [55] N. W. Ashcroft, *Physique des solides*. EDP, 2002.
- [56] R. P. Feynman *Physical Review*, vol. 56, p. 340, 1939.
- [57] P. D. DeCicco and F. A. Johnson *Proceedings of the Royal Society A*, vol. 310, p. 111, 1969.
- [58] R. M. Pick, M. H. Cohen, and R. M. Martin *Physical Review B*, vol. 1, p. 910, 1970.

- [59] P. Giannozzi, S. de Gironcoli, P. Pavone, , and S. Baroni *Physical Review B*, vol. 43, p. 7231, 1991.
- [60] L. E. Ballentine, *Quantum Mechanics*. World Scientific, 1998.
- [61] R. M. Sternheimer *Physical Review*, vol. 96, p. 951, 1954.
- [62] L. Paulatto, I. Errea, M. Calandra, and F. Mauri *Physical Review B*, vol. 91, p. 054304, 2015.
- [63] M. Lazzeri and S. de Gironcoli *Physical Review Letters*, vol. 81, p. 2096, 1998.
- [64] A. H. Romero, E. K. U. Gross, M. J. Verstraete, and O. Hellman *Physical Review B*, vol. 91, p. 214310, 2015.
- [65] A. A. Maradudin and A. E. Fein *Physical Review*, vol. 128, p. 2589, 1962.
- [66] M. L. M. Calandra and F. Mauri *Physica C: Superconductivity*, vol. 456, p. 38, 2007.
- [67] B. Rousseau and A. Bergara *Physical Review B*, vol. 82, p. 104504, 2010.
- [68] M. Lazzeri, M. Calandra, and F. Mauri *Physical Review B*, vol. 68, p. 220509, 2003.
- [69] X. Gonze and J.-P. Vigneron *Physical Review B*, vol. 39, p. 13120, 1989.
- [70] L. Paulatto, F. Mauri, , and M. Lazzeri *Physical Review B*, vol. 87, p. 214303, 2013.
- [71] G. Deinzer, G. Birner, and D. Strauch *Physical Review B*, vol. 67, p. 144304, 2003.
- [72] M. Lazzeri and S. de Gironcoli *Physical Review B*, vol. 65, p. 245402, 2002.
- [73] W. Li, J. Carrete, N. A. Katcho, and N. Mingo *Computer Physics Communications*, vol. 185, no. 6, p. 1747, 2014.
- [74] N. Bonini, M. Lazzeri, N. Marzari, and F. Mauri *Physical Review Letters*, vol. 99, p. 176802, 2007.

-
- [75] I. I. M. M. Calandra and F. Mauri *Physical Review B*, vol. 80, p. 241108, 2009.
- [76] P. Souvatzis, O. Eriksson, M. I. Katsnelson, and S. P. Rudin *Physical Review Letters*, vol. 100, p. 095901, 2008.
- [77] O. Hellman, P. Steneteg, I. A. Abrikosov, and S. I. Simak *Physical Review B*, vol. 87, p. 095901, 2013.
- [78] D. Hooton , *The London, Edinburgh, and Dublin Philosophical Magazine and Journal of Science*, vol. 46, p. 422, 1955.
- [79] L. D. Landau and E. M. Lifshitz, *Course of Theoretical Physics, 3rd ed., Statistical Physics Vol. 5.* (Butterworth-Heinemann, 1980).
- [80] P. Giannozzi, S. Baroni, N. Bonini, M. Calandra, R. Car, C. Cavazzoni, D. Ceresoli, G. L. Chiarotti, M. Cococcioni, I. Dabo, A. D. Corso, S. Fabris, G. Fratesi, S. de Gironcoli, R. Gebauer, U. Gerstmann, C. Gougoussis, A. Kokalj, M. Lazzeri, L. Martin-Samos, N. Marzari, F. Mauri, R. Mazzarello, S. Paolini, A. Pasquarello, L. Paulatto, C. Sbraccia, S. Scandolo, G. Sclauzero, A. P. Seitsonen, A. Smogunov, P. Umari, and R. M. Wentzcovitch *Journal of Physics: Condensed Matter*, vol. 21, p. 395502, 2009.
- [81] K. B. J. P. Perdew and M. Ernzerhof *Physical Review Letters*, vol. 77, p. 3865, 1996.
- [82] N. Troullier and J. L. Martins *Physical Review B*, vol. 43, p. 1993, 1991.
- [83] P. E. Blochl *Physical Review B*, vol. 50, p. 17953, 1994.
- [84] C. D. O'Neill, D. A. Sokolov, A. Hermann, A. Bossak, C. Stock, , and A. D. Huxley *Physical Review B*, vol. 95, p. 144101, 2017.
- [85] Y. C. X. Ai and C. A. Marianetti *Physical Review B*, vol. 90, p. 014308, 2014.
- [86] Y. C. X. Ai and C. A. Marianetti *Physical Review Letters*, vol. 113, p. 105501, 2014.
- [87] T. Shiga, J. Shiomi, J. Ma, O. Delaire, T. Radzynski, A. Lusakowski, K. Esfarjani, , and G. Chen *Physical Review B*, vol. 85, p. 155203, 2012.

- [88] N. Hatcher, O. Y. Kontsevoi, , and A. J. Freeman *Physical Review B*, vol. 79, p. 020202, 2009.
- [89] N. Hatcher, O. Y. Kontsevoi, , and A. J. Freeman *Physical Review B*, vol. 80, p. 144203, 2009.
- [90] K. Chang, J. Liu, H. Lin, N. Wang, K. Zhao, A. Zhang, F. Jin, Y. Zhong, X. Hu, W. Duan, Q. Zhang, L. Fu, Q.-K. Xue, X. Chen, and S.-H. Ji *Science*, vol. 15, p. 144203, 2016.
- [91] S. H. Vosko, L. Wilk, , and M. Nusair *Canadian Journal of Chemistry*, vol. 58, p. 1200, 1980.
- [92] J. P. Perdew and A. Zunger *Physical Review B*, vol. 23, p. 5048, 1981.
- [93] C. Lee, W. Yang, and R. G. Parr *Physical Review B*, vol. 37, p. 785, 1988.
- [94] J. P. Perdew and Y. Wang *Physical Review B*, vol. 45, p. 13244, 1992.